Wesleyan University The Honors College

Transit, Secondary Eclipse, and Phase Curve Analysis to Characterize *Kepler* Exoplanets

by

Jesse Tarnas
Class of 2016

A thesis submitted to the
faculty of Wesleyan University
in partial fulfillment of the requirements for the
Degree of Bachelor of Arts
with Departmental Honors in Astronomy

Middletown, Connecticut April, 2016

But as soon as somebody demonstrates the art of flying, settlers from our species of man will not be lacking. Who would once have thought that the crossing of the wide ocean was calmer and safer than of the narrow Adriatic Sea, Baltic Sea, or English Channel? Given ships or sails adapted to the breezes of heaven, there will be those who will not shrink from even that vast expanse. Therefore, for the sake of those who, as it were, will presently be on hand to attempt this voyage, let us establish the astronomy, Galileo, you of Jupiter, and me of the moon.

–Johannes Kepler

Dissertatio Cum Nuncio Sidereo, 1610

Translated by Hellman (1965)

Acknowledgements

There are far too many people I ought to thank than can fit on this small page. First and foremost, many thanks to my mom, dad, and sister for all the great years that have led to now. I'd also like to thank all my aunties, uncles, grandparents, cousins, and hanai brothers and sisters who have helped make me the person I am today.

To my research advisor, Seth Redfield, who has mentored me for more than three years. Thank you for teaching me what it means to be a scientist. The 18 year old kid you met three years ago would not be where he is today without you.

To all my friends at Wesleyan –thank you for the good times and memories, you will always be treasures to me.

To all my friends from back on the Big Island –thanks for sticking with me even through the long distances and times between seeing each other. There's nothing like being home again with all of you.

To James Greenwood, another research advisor who taught me a completely new set of scientific skills. Thank you for each piece of knowledge.

To Marty Gilmore, who was my primary source of advice for applying to planetary science graduate school. Thank you for believing in me and helping me to succeed.

To Reinhold Blümel, who invited me into his research group two weeks into my first semester at Wesleyan. Thank you for giving me the background, confidence, and skills necessary to pursue research. The day that I met you was truly a fortunate one for me.

Contents

Chapter 1

Introduction

Cosmological models and observations tell us the universe is 69% dark energy and 26.8% dark matter (Planck Collaboration et al. 2014), which we can neither see nor interact with. The remaining 4.9% is baryonic matter, which composes billions of galaxies, each a collection of billions of stars. Our star, the Sun, represents 99.8% of the mass in our solar system (Woolfson 2000). Jupiter's mass composes over half of the remaining 0.2%, leaving less than 0.1% for the other seven planets.

The galaxies are relatively small when viewed at extensive scales, at which point they appear as a supercluster composed of thousands of gravitationally bound galaxies. Our galactic supercluster is called Laniakea (in Hawaiian: *lani*, heaven; *akea*, spacious, immeasurable) (Tully et al. 2014). Each galaxy is composed of billions of tiny specks called stars, which are orbited by astonishingly smaller objects called planets. These smallest of specks are some of the most interesting objects in the universe. In our solar system alone, they foster the country-sized extinct volcanoes of Mars, the cold oceans of Europa and Enceladus, the fiery atmosphere of Venus, the Earth sized hurricanes of Jupiter, the hydrocarbon lakes and rivers of Titan, the majestic rings of Saturn, and the fragile life of Earth. Planets are therefore worth searching for around other stars in order to expand our knowledge of planetary diversity and the prevalence of planetary

systems in general. However, their minuscule size and relatively cool temperatures make them difficult objects to study.

Planets are interesting for the same reason that they are difficult to study –they do not generate and radiate energy like stars, but absorb and metabolize it, eventually radiating the energy back at different wavelengths. Their lack of significant emission makes them difficult to directly image even with our largest telescopes. Exoplanet host stars must therefore be used in order to detect their surrounding planets. Two methods–radial velocity and transit analysis–have dominated exoplanet science for decades. At the end of the 20th century and first decade of the 21st century, radial velocity detections dominated the field as the most fruitful discovery technique, and still has discovered more long period planets than any other method (Akeson et al. 2013). However, with the launch of the *Kepler Space Telescope* in 2009 (Haas et al. 2010), the transit method has discovered thousands of exoplanets within the last six years (Akeson et al. 2013). Humanity now knows that most stars possess planetary systems and that Earth-sized planets are more common than larger planets (Fressin et al. 2013), unlocking seemingly infinite possibilities for planetary diversity and, probably, for extraterrestrial life.

1.1 Techniques for discovering exoplanets

1.1.1 Radial velocity technique

Johannes Kepler, the prominent German astronomer for whom the space telescope is named, was the first human to accurately describe the movements of the planets in the Solar System using empirical mathematical laws (Kepler 1609). The first of these laws states that the orbit of any planet is an ellipse with the Sun located at one of two foci. Kepler's description preceded the development of

Newtonian mechanics (Newton 1687) and advances in telescope technology beyond Galileo's (Galilei 1610), so this simplification was sufficient to match observations. However, in reality, Newton's Third Law of Motion tells us that for every action there is an equal and opposite reaction (Newton 1687). Both objects orbit one center, the system's center of mass, which is within the Sun's volume or near it because of its greater mass. Therefore, while the Sun exerts a gravitational force on a planet, driving its orbit, the planet exerts a gravitational force on the star, causing it to orbit in a smaller ellipse of equal eccentricity and period. This "wobble" can be measured via redshift and blueshift, which are caused by the Doppler effect (Doppler 1842). As a star moves toward an observer, its light is shifted toward the blue (shorter wavelengths and higher frequencies), and while it moves away light is shifted towards the red (longer wavelengths and lower frequencies). This is only possible when the star's orbit is inclined with respect to the observer ($0° < i \leq 90°$), as illustrated in Figure 1.1.

With the appropriate inclination, spectroscopy can be used to measure the shape and distance of an exoplanet's orbit, as well as a minimum planet mass $M_p \sin(i)$. This final measurement inherently contains a parameter degeneracy, as the values of M_p and i cannot be differentiated empirically. The following equation is used to relate the aforementioned parameters to radial velocity measurements (Lovis & Fischer 2010):

$$K_* = \left(\frac{G}{1-e^2}\right)^{1/2} M_p \sin(i) M_*^{-1/2} a^{-1/2},$$

where K_* is the radial velocity semi-amplitude, G is the gravitational constant, e is eccentricity, M_p and M_* are planetary and stellar mass, and a is semi-major axis. The equation illustrates the interconnectivity of M_p and i in the radial velocity

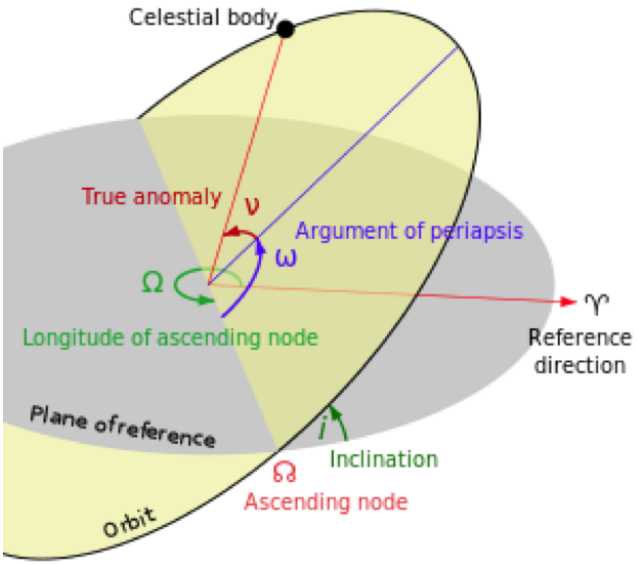

Figure 1.1: The star's spin axis is perpendicular to the orbital plane (yellow), which is tilted a certain number of degrees relative to the observer, called the inclination i. Inclination is 90° for an edge on orbit and 0° for a face on orbit. The celestial body, in this case an exoplanet, orbits elliptically on this orbital plane, following the star's spin. True anomaly (ν here) indicates the location of an object in its orbital ellipse relative the the foci of the system's center of mass. In the case of our Solar System, this foci would be within or very near to the volume of the Sun, but not at the exact center. The exact center of mass differs widely among star systems, therefore this classification of orbital location is convenient for astronomers. Argument of periapsis ω documents the position of the planet relative to its pericentre, which is the point in its orbit when its distance from the star is at minimum. From Lasunncty (2007).

technique, which generates an inherent degeneracy between these two parameters.

1.1.2 Transit technique

Transits occur when an exoplanet crosses in front of its host star relative to the observer's line of sight. The planet blocks a measurable amount of flux from the star in a periodic manner. If the host star radius is known, the depth of the transit can be related to planet radius by the following equation (Seager & Mallén-Ornelas 2003):

$$\Delta F = \frac{F_{notransit} - F_{transit}}{F_{notransit}} = \left(\frac{R_p}{R_*}\right)^2 .$$

Provided multiple transits are observed, the time between transits gives the planet's orbital period, as shown in Figure 1.2. The smaller dimming effect at a phase of $\phi = 0.5$, or shifted slightly from $\phi = 0.5$ based on eccentricity (e) and argument of periastron (ω), is called a secondary eclipse or occultation, which occurs when the planet passes behind the host star relative to the observer's line of sight.

1.1.3 Secondary Eclipse

Kepler measures the flux of an entire star-planet system. While the vast majority of the flux is contributed by the star, thermal emission from the planet also contributes. The degree of planet flux contribution depends on the planet's temperature and size, so this effect differs in magnitude between exoplanetary systems. The planetary equilibrium temperature, T_{eq}, is calculated as (López-Morales & Seager 2007)

$$T_{eq} = T_* \left(\frac{R_*}{a}\right)^{1/2} [f(1 - A_B)]^{1/4},$$

where T_* is the stellar temperature; R_* is the stellar radius, a is the semi-major axis, and A_B is the Bond albedo, which is defined by $A_B = (3/2)A_g$, where A_g is the geometric albedo. The eclipse depth, F_{ecl}, is given as (Esteves et al. 2015)

$$F_{ecl}[\lambda] = \left(\frac{R_p}{R_*}\right)^2 \frac{\int B_\lambda[T_{eq}]G[\lambda]d\lambda}{\int (G[\lambda]F_\lambda d\lambda)} + A_g \left(\frac{R_p}{a}\right)^2$$

where B_λ is the Planck function as a function of T_{eq}, $G[\lambda]$ is the *Kepler* transmission function, F_λ is the stellar flux computed using the NEXTGEN model spectra (Hauschildt et al. 1999), and A_g is the geometric albedo.

In addition to constraining thermal emission and reflection, secondary eclipse analysis allows for better constraint of eccentricity, as eccentric orbits can shift the center of the eclipse from $\phi = 0.5$ depending on the argument of periastron. This additional lightcurve analysis makes the transit technique significantly more robust.

1.1.4 Transit Spectroscopy

Exoplanet transits can produce different transit depths for the same planet when viewed at different wavelengths. Imagine Earth viewed as a transiting exoplanet by an observer in another star system. Through most wavelengths, only the rock and water of Earth would block out the Sun's light. However, if the transit is viewed through the wavelengths of blue visible light, the Earth's atmosphere would also block the Sun's light, because it is optically thick at those wavelengths due to Rayleigh scattering. The transit depth at these wavelengths

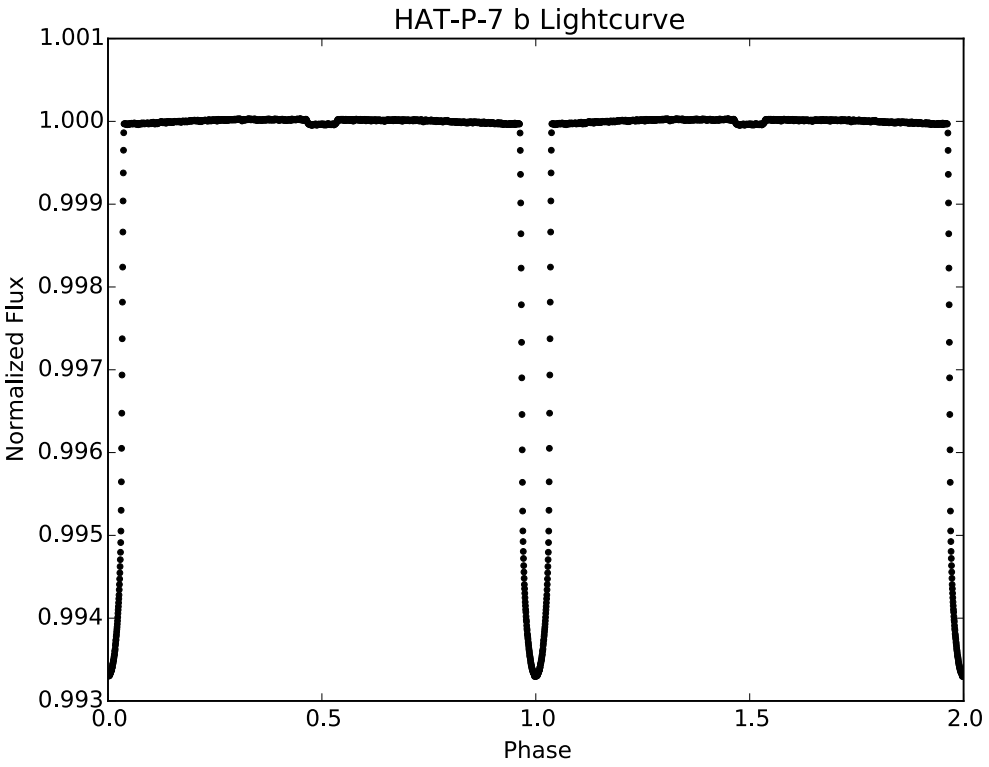

Figure 1.2: Reduced *Kepler* data for HAT-P-7 b. This target has a very pronounced secondary eclipse and transit. Phase curves are too subtle an effect to be seen at this scale. The transit occurs at phase $\phi = 0,\ 1,\ 2$ while the secondary eclipse occurs at phase $\phi = 0.5,\ 1.5$.

would be deeper than at other wavelengths, which would give information regarding the density, temperature, and composition of Earth's atmosphere. This same principle can also be applied to other types of atmospheres, such as exoplanetary gas giants, though the definition of where the atmosphere begins is somewhat different in this scenario. In the following equations used to model exoplanet atmospheres, k is the Boltzmann constant, T is the estimated temperature of the planet, μ is the mean molecular weight of the atmosphere, and g is the planet's gravity on a logarithmic scale. The mean molecular weight describes the mean mass of particles in an atmosphere. The atmospheric scale height, H, is a constant that describes the radial distance over which the atmosphere's density decreases, calculated as

$$H = \frac{kT}{\mu g}.$$

It is used to obtain the actual atmospheric height, Z, calculated as (Lecavelier Des Etangs et al. 2008)

$$Z(\lambda) = Hlog\left(\frac{P_o\sigma(\lambda)}{\tau_{eq}}\left(\frac{2\pi R_p}{kT\mu g}\right)^{1/2}\right)$$

where P_o is the pressure at the atmosphere's zero altitude point, $\sigma(\lambda)$ is the scattering cross section of the atmosphere, which changes with wavelength, τ_{eq} is the optical depth at the zero altitude point, and R_p is the planet's radius. With knowledge of the atmospheric height, the planet's radius with the atmosphere as a discrete contributing component is described as (Lecavelier Des Etangs et al. 2008)

$$R_{p+z}(\lambda) = R_p + Z(\lambda)$$

where $Z(\lambda)$ changes as $\sigma(\lambda)$ changes when observing through different wavelengths. As such, the effective planetary radius differs with wavelength, which produces a detectable change in transit depth, $\Delta F(\lambda)$, defined as:

$$\Delta F(\lambda) = \left(\frac{R_{p+z}(\lambda)}{R_*} \right)^2$$

where $R_{p+z}(\lambda)$ is the planetary radius including the atmosphere. $\frac{d\Delta F}{d\lambda}$ describes the behavior of flux change with respect to wavelength and can be used to obtain an estimate of an exoplanet atmosphere's mean molecular weight and temperature by comparison with spectroscopic data from observations. Because it is caused by Rayleigh scattering, this effect is useful primarily in visible to near-infrared wavelengths, as shown in Figure 1.3.

Multiwavelength spectroscopy is not possible with *Kepler*, so most exoplanet atmosphere studies are conducted with other space-based or ground-based telescopes.

1.1.5 Phase Curve Analysis

During the first stages of the *Kepler* mission, scientists actively analyzed lightcurves searching solely for transits. Discovering one was doubtlessly an impressive feat. In modern *Kepler* data analysis, transits are regarded as large and obvious features that clearly indicate the presence of an extrasolar planet. Phase curves are now regarded as the subtle signals fit only by models of the highest precision. They are created by a combination of reflected light and thermal emission from the planet, as well as the gravitational effects of ellipsoidal variations and Doppler boosting.

Reflected light is a function of the geometric albedo of the exoplanet's at-

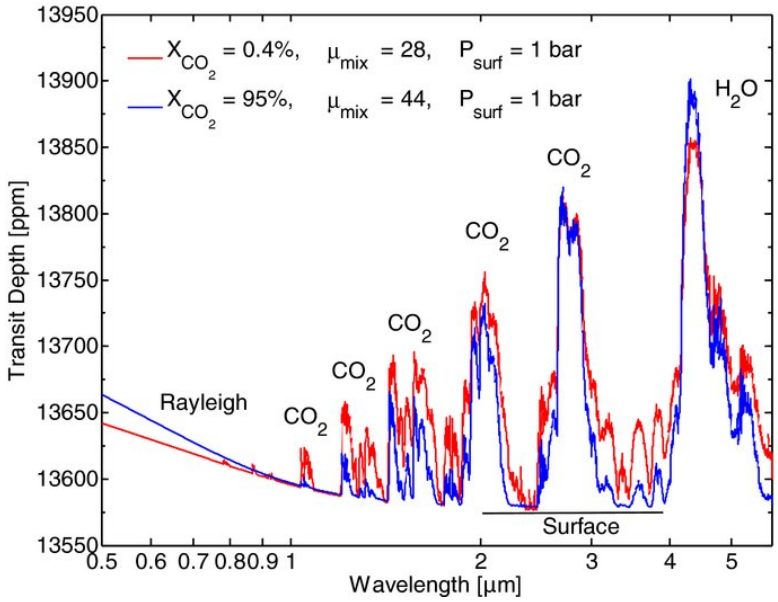

Figure 1.3: This model spectrum illustrates the change in transit depth with respect to wavelength. Using data from wavelengths higher than 1 μm, it is difficult to tell the difference between two model atmospheres with extremely different bulk CO_2 content (0.4% vs 95%). However, the slope of the Rayleigh scattering is distinct for both atmospheres. Using high-resolution spectroscopy to observe Rayleigh scattering in exoplanet atmospheres is therefore an effective means of estimating an atmosphere's temperature and mean molecular weight, which allows for characterization of atmospheric chemistry. From Benneke & Seager (2012).

mosphere, which is a valuable probe of atmospheric constituents. The thermal emission phase curve shape is nearly identical to the reflected light phase curve shape in most systems, but the amplitudes of the curves are used to determine which source is contributing the most to the overall phase shape. Additionally, the location of maximal thermal emission from the planet may not be the same as the substellar point, which describes the point on the planet receiving the most direct flux from the star. If this is the case, exoplanetary winds of extremely high velocities, which transport this heat from the hot zone to cooler parts of the planet, can be measured (Cowan & Agol 2011). The gravitational phase effects, ellipsoidal variations and Doppler beaming, provide direct constraints of an exoplanet's mass. In radial velocity analysis, measurements of an exoplanet's mass are degenerate with the system's inclination, therefore this is a valuable constraint made possible by phase curves.

The task of phase curve models is to tease out the relative contribution of each effect, a process that characterizes the exoplanet. Phase curves allow us to determine exoplanet atmosphere characteristics using single-band photometry. Furthermore, they allow scientists to circumvent the mass-inclination parameter degeneracy that is present in radial velocity analysis. An integrated model that characterizes the transit, secondary eclipse, and phase curves of an exoplanetary system is therefore the most powerful tool for *Kepler* data analysis. This thesis centers around the creation of this model.

1.2 *Kepler*

Launched in 2009, the *Kepler* space telescope remains the most important and iconic instrument in the history of exoplanet science. Its purpose is to detect and

characterize transiting exoplanet systems within its 115° field of view, with particular interest in exoplanets orbiting in their star's habitable zone. The mission has been a tremendous success thus far, detecting over 1000 confirmed planets and over 3000 exoplanet candidates (Akeson et al. 2013), some Earth-sized and within their star's habitable zone. Failure of two of four reaction wheels on the spacecraft stratified the mission into two distinct phases: *K1* and *K2* (Howell et al. 2014). *K1* denotes the time from launch to second wheel failure in May 2013. The spacecraft observed a single patch of sky for this entire period. Figures 1.4 and 1.5 show the spatial distribution of stars with orbiting exoplanets discovered by *Kepler*. Figure 1.6 shows the distribution of stars with known exoplanets in the galaxy, including those not discovered by *Kepler*.

The *K2* mission uses pressure from solar radiation to balance the telescope in lieu of two reaction wheels. Because *Kepler* is in an Earth trailing orbit, it must continuously adjust itself to maintain proper orientation relative to the Sun, meaning its field of view changes approximately every 83 days, 75 of which are dedicated to science. Its fields of observation are solely on the ecliptic plane. Though *K2* data has lesser photometric precision, its unexplored fields of view offer new opportunities for exoplanet discoveries.

During *K1*, the telescope took both long cadence (30 minute) and short cadence (30 second) exposures using a 42 CCD photometer with a full bandpass of 348-970 nm and half-maximum bandpass of 435-845 nm (Van Cleve et al. 2009). *K2* uses the remaining 40 CCD modules to observe 105° of sky, collecting data at 30 minute and 1 minute cadences (Howell et al. 2014). *K1* and *K2* data precision are compared in Figure 1.7. While its data is less precise and does not cover a single area for more than 75 scientifically dedicated days, *K2* has the potential to continue the strong momentum of space based exoplanet science.

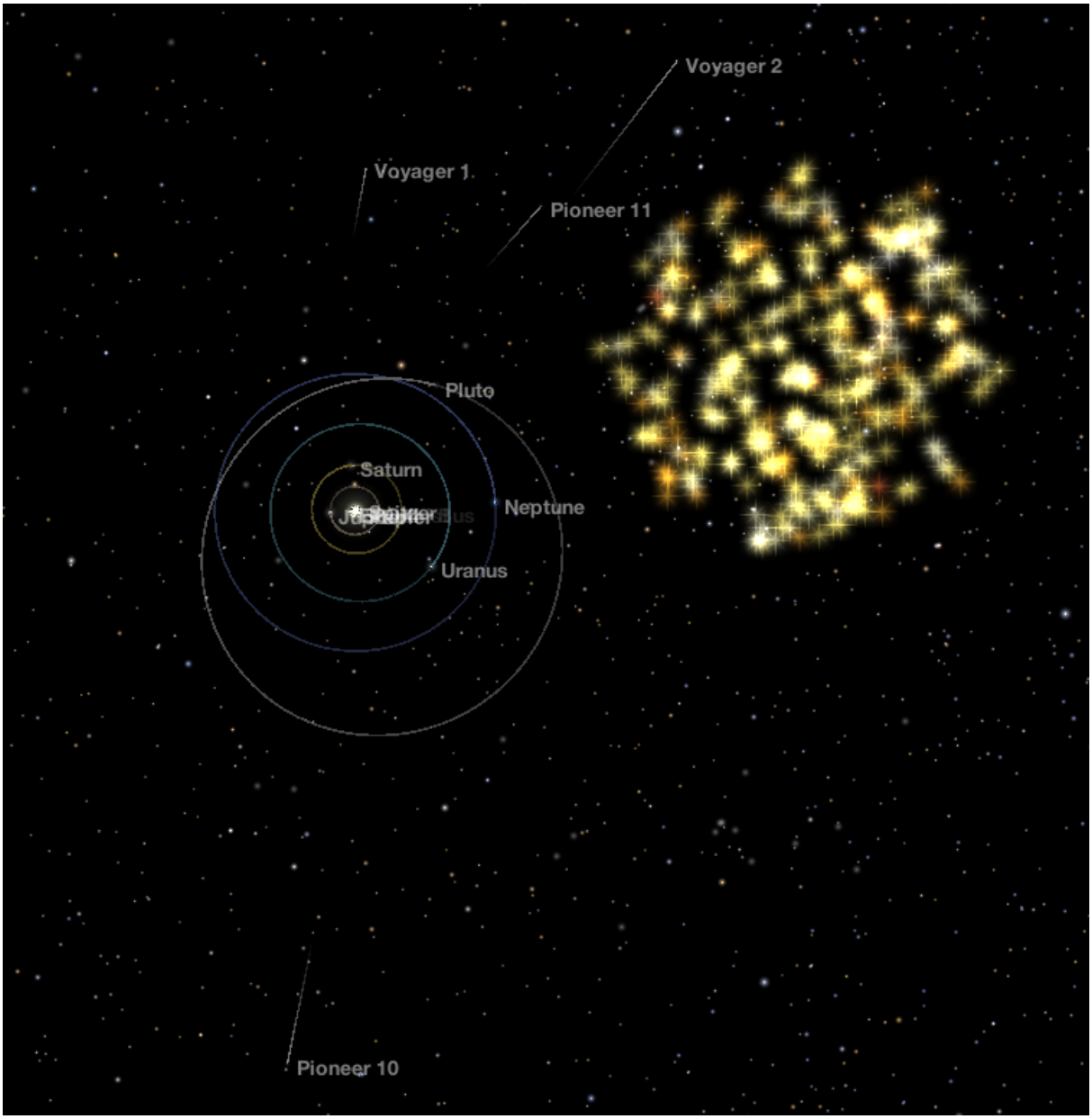

Figure 1.4: The illuminated stars host exoplanets, all of which were discovered by *Kepler*. The imprint of *Kepler*'s 42 CCD photometer is left upon the sky, as it represents our primary source of exoplanet discoveries. For perspective, this image is zoomed out from the Solar System approximately 1 light day. The South poles of the Sun and planets are pointing out of the page, thus the planets would be rotating clockwise from this perspective. From NASA's Eyes on Exoplanets, Biferno A. (2015).

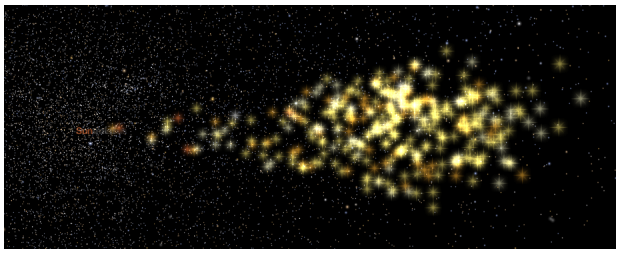

Figure 1.5: Zoomed out approximately 900 light years from the Solar System. The Sun's North-South axis points 90° away from the observer from this perspective. At this angle, the conical shape of the 3D distribution of exoplanets discovered by *Kepler* becomes apparent. This is because the same solid angle of sky contains a greater volume of space farther away from the observer, which means the CCD detects a wider physical distribution of stars that are farther away. As such, the field of view extends as a cone with the Sun at the cone's very tip. From NASA's Eyes on Exoplanets, Biferno A. (2015).

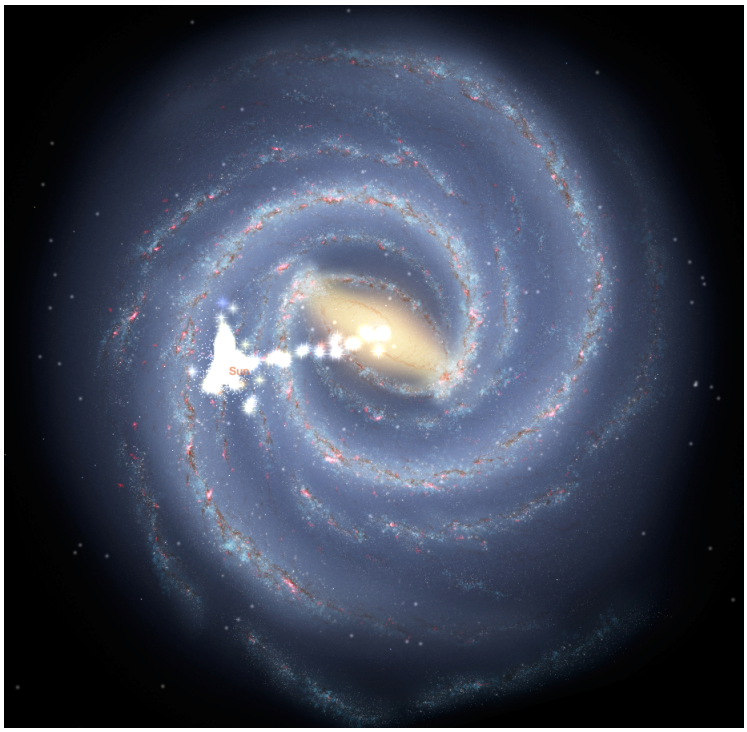

Figure 1.6: Zoomed out approximately 100,000 light years from the Solar System. This shows the distribution of stars with discovered exoplanets in our galaxy. The "peninsula" of illuminated stars extending toward the top of the figure are the *Kepler* discoveries. The other "peninsula" extends towards the galactic center. There are billions of stars within our galaxy, but all discovered exoplanets are confined to within 1000 light years of the Sun. The surface has just been scratched for galactic exoplanet discovery. From NASA's Eyes on Exoplanets, Biferno A. (2015).

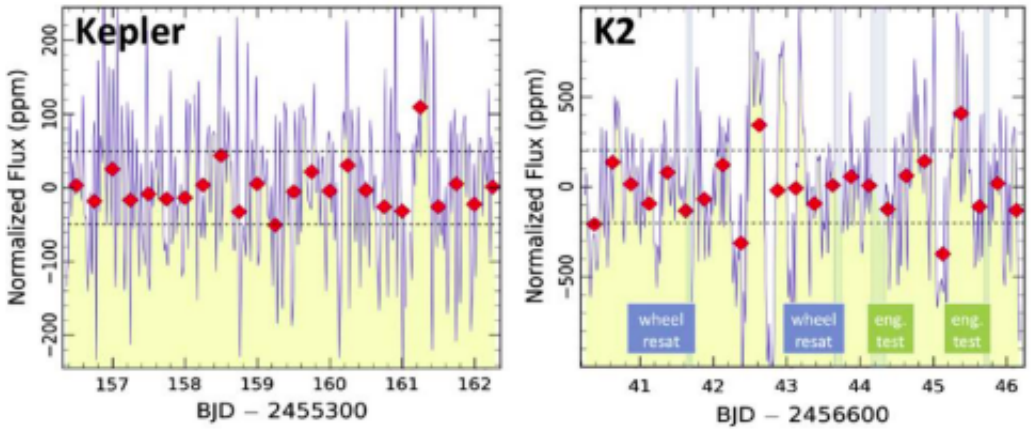

Figure 1.7: *K2* data precision compared to *Kepler* data precision. Both lightcurves are from a 12th magnitude target. *K2* demonstrated a precision of 82 ppm during its 2013 December test. From Howell et al. (2014).

1.3 The value of exoplanet science

Characterizing the diversity of existing planets allows us to place our world in the context of other worlds. Humanity is distinct from all other species of creature because the globalization of civilization allows us to analyze ourselves with awareness of the surrounding world beyond our immediate sensory instruments. A civilization's maps define their breadth of awareness regarding their surroundings. Only now that we have precisely characterized the Earth can we seek a truer understanding of our actual relationship with it. It becomes apparent that we are no longer isolated nations refining their maps, but an entire species that has been granted the planetary conditions for genetic development against significant odds. Self-awareness seems to have developed on the fascinating debris of stars. Though this debris is difficult to study, our species has finally developed the wisdom and technology necessary to evolve our planetary map craft to a galactic scale.

Amidst this map making, we, like our exploring ancestors, may encounter

other beings we were previously unaware of. At first we may only be able to see biochemical signatures in their atmospheres, but exoplanet science has the potential to radically change our understanding of the prevalence of life in the galaxy. While we will certainly explore the four currently favored life hosting bodies in the solar system–Europa, the Martian subsurface, Titan, and Enceladus–the diversity of potential targets for exoplanetary life is not quantifiable. As we continue to characterize smaller, more Earth-like worlds with increased precision, our knowledge of life could be revolutionized. We can only wait and see what the future holds.

Chapter 2

Modeling

The purpose of our model is to theoretically predict the lightcurve of an exoplanetary system based on that system's specific characteristics. We model the transit, which is the dominant feature in the lightcurve, as well as the secondary eclipse and phase curves, which are much more subtle effects. Precisely modeling each of these features allows us to obtain valuable information regarding planetary radii, masses, orbits, temperatures, and albedos.

2.1 Basic Equations

Modeling is simply the theoretical calculation of a particular effect based on a series of well characterized equations that describe the behavior of that system. In our particular case, we have a series of equations that describe the three dimensional elliptical motion of the exoplanet around its host star. These are coupled to a series of equations that use exoplanet characteristics such as radius, mass, temperature, and albedo to calculate the amount of flux from the star blocked by the planet during transit, the amount of flux from the planet blocked by the star during secondary eclipse, and the amount of flux contributed by the thermal, reflective, ellipsoidal variations, and Doppler beaming phase effects. With this extensive series of coupled equations, our model can predict the flux received over time from an exoplanetary system with specific characteristics. While all models

are imperfect in some form, many are accurate enough to provide extremely valuable information. In our case, the combined transit, secondary eclipse, and phase curve model is accurate enough to model even the most subtle flux effects found in *Kepler* lightcurves.

2.1.1 Orbit

Modeling transit, secondary eclipse, and phase curve effects requires mathematical constraint of exoplanetary orbital parameters. With proper description of the planet's orbit, it is possible to assess its other characteristics. First, the mean anomaly, $M(t)$, is calculated, which describes the location of an exoplanet in its orbit as

$$M(t) = M_0 + \frac{2\pi t}{P}$$

where $M(t)$ is in radians, t is time and P is the period. When $t = P$, the mean anomaly is equal to the initial mean anomaly, M_0, which describes the planet's location on its projected orbital circle at the nominal beginning of each new orbit. If all planets orbited in circles, this relationship would be sufficient to describe an object's location on its orbital path. However, eccentric orbits require us to describe the true anomaly, $f(t)$, as

$$f(t) = 2 \arctan\left(\sqrt{\frac{1+e}{1-e}} \tan\left(\frac{E(t)}{2}\right)\right),$$

where $E(t)$ is the eccentric anomaly. True anomaly describes the deviation of an exoplanet's actual orbital ellipse from its projected orbital circle defined by the mean anomaly. The geometric relationship between mean and true anomaly is

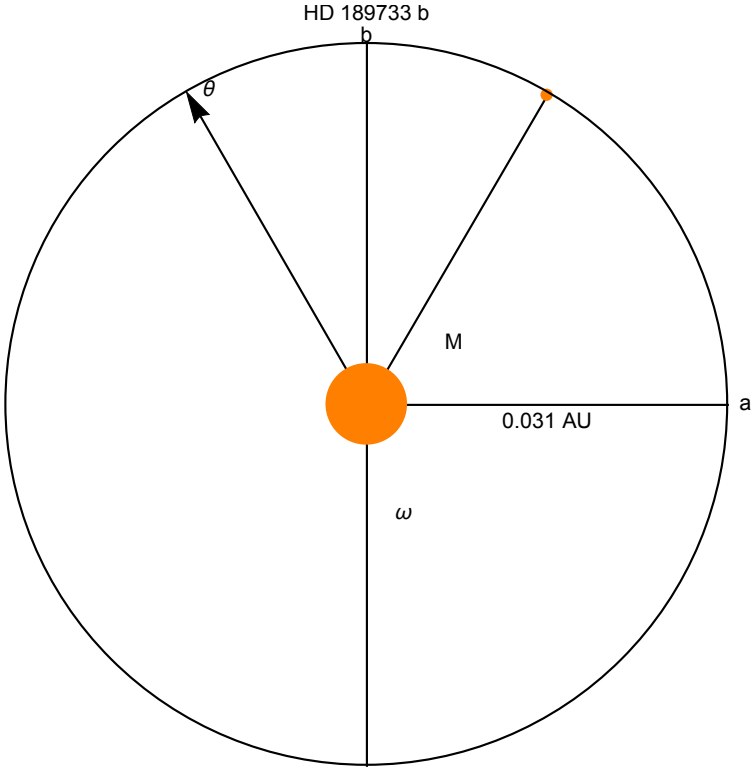

Figure 2.1: Illustrates the orbit of HD189733 b, with and star size scaled accurately. M is the mean anomaly, a is the semimajor axis, b is the semiminor axis, ω is the longitude of periastron, and θ is the angle where the phase is zero.

illustrated in Figures 2.1 and 2.2 for the example case of HD 189733 b, in which eccentricity (e), semimajor axis (a), and period (P) are 0, 0.031 AU, and 2.219 days respectively. Many hot-Jupiters have circular orbits, as tidal forces induce circular orbits and hot-Jupiters are often tidally locked to their host stars.

The eccentric anomaly, $E(t)$, is defined by the transcendental equation

$$E(t) = M(t) + e \sin E(t),$$

which must be solved numerically. The model uses a numerical solution described

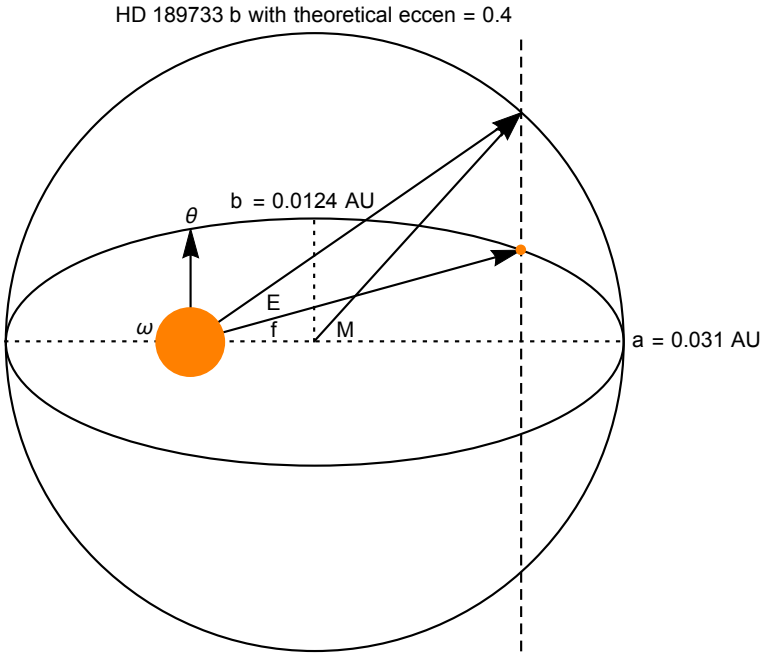

Figure 2.2: The 2 dimensional projection of a face-on ($i = 0°$) orbit for HD189733 b is shown with a heavily exagerrated eccentricity of $e = 0.4$ to illustrate its impact on the orbit's shape. M is the mean anomaly, f is the true anomaly, E is the eccentric anomaly, ω is the longitude of periastron, e is the eccentricity, a is the semimajor axis, and b is the semiminor axis. The circle that intersects the ellipse at the ends of its long axis is the one projected in the equation for mean anomaly. The dashed line connects the planet's position on its orbital ellipse to its position on the mean anomaly circle.

in Murray & Dermott (1999) as

$$E_{i+1} = M + e \sin E_i$$

where i marks the iteration number of the program. This equation iterates until a specified tolerance precision value of $|E_{i+1} - E_i|$ is achieved. The model uses the 10^{-8} tolerance value suggested by Murray & Dermott (1999). After calculating the eccentric anomaly, the true anomaly can be solved for. Furthermore, the distance between planet and star can be calculated as

$$d(t) = a(1 - e \cos E(t))$$

which accounts for the changing distance due to eccentricity. See Murray & Dermott (1999) for derivations of the aforementioned equations and a thorough discussion of orbital dynamics. The final calculation is the phase angle

$$\theta(t) = \arccos(\sin(\omega + f(t)) \sin i)$$

where ω is the argument of periastron, the angle that separates the planet's orbital location from its pericenter. The phase angle describes the angle between the vector of observer's line-of-sight and the vector from star to planet (Mislis et al. 2012; Placek et al. 2014). Now, we have a complete description of the orbital ellipse or circle of a modeled exoplanet, which allows us to accurately model the transit, secondary eclipse, and phase curves from a planet-star system based on specified input parameters.

2.1.2 Transit

With proper orbital modeling, we can now model the depth and duration of the transit based on the planet-star radius ratio, period, semimajor axis, inclination, argument of periastron, and eccentricity. First contact is the time at which the edge of the planet touches the first edge of the star from the observer's point of view. Second contact denotes the time at which the trailing edge of the planet crosses the first edge of the star. Third contact is the time at which the leading edge of the planet contacts the second edge of the star. Fourth contact is when the trailing edge of the planet contacts the second edge of the star. Our model uses PyTransit (Parviainen 2015) to model the transit and the Crossfield (2012) transit light curve code to model the secondary eclipse, both of which use the Mandel & Agol (2002) formalism. Where R_p is the planetary radius, R_* is the stellar radius, and d is the distance between the two objects, the depth of the transit, $\delta_{transit}$, is described by Mandel & Agol (2002) as

$$\delta_{transit} = \begin{cases} 0, & \text{where } 1 + k > z \\ \frac{1}{\pi}[k^2\kappa_0 + \kappa_1 - \sqrt{\frac{4z^2-(1+z^2-k^2)^2}{4}} & \text{where } |1-k| < z \leq 1+k \\ k^2, & \text{where } z \leq 1-k \\ 1 & \text{where } z \leq -1 \end{cases} \tag{2.1}$$

$$\kappa_1 = \arccos\left[\frac{1-k^2+z^2}{2z}\right]$$

$$\kappa_0 = \arccos\left[\frac{k^2+z^2-1}{2kz}\right]$$

$$k = \frac{R_p}{R_*}, z = \frac{d}{R_*}.$$

Clearly the depth of the transit, $\delta_{transit}$, is highly dependent on the planet-star radius ratio and the distance between the two objects. The nonuniform brightness of the stellar photosphere is also a factor and is described by limb darkening. The backdrop of the star at second and third contact is slightly dimmer than it is in the middle of transit, as the observer's line of sight vector does not penetrate as deeply into the star's photosphere, as it is diagonal at second and third contact rather than orthogonal to the star's surface, as it is during the transit center. Because this line of sight vector does not go as deep into the star at second and third contact as it does during midtransit, the material observed is cooler at these locations, which means the observer does not receive as much flux. Limb darkening also changes as a function of wavelength (Knutson et al. 2007). Limb darkening coefficients are plugged into a series of quadratic equations in the Mandel & Agol (2002) formalism, producing the different transit models shown in Figure 2.3.

Now that the transit depth as a function of input parameters is known, the duration of the transit must be calculated. First we must calculate the impact parameter (Winn 2010)

$$b_{transit} = \frac{a\cos(i)}{R_*}\Big(\frac{1-e^2}{1+e\sin(\omega)}\Big),$$

which describes the location of the transit across the star's disk and is illustrated in Figure 2.4.

With knowledge of the impact parameter, we can calculate the full duration of the transit, as well as fractional durations of ingress, egress, and full transit (second-third Contact) through the equation (Winn 2010)

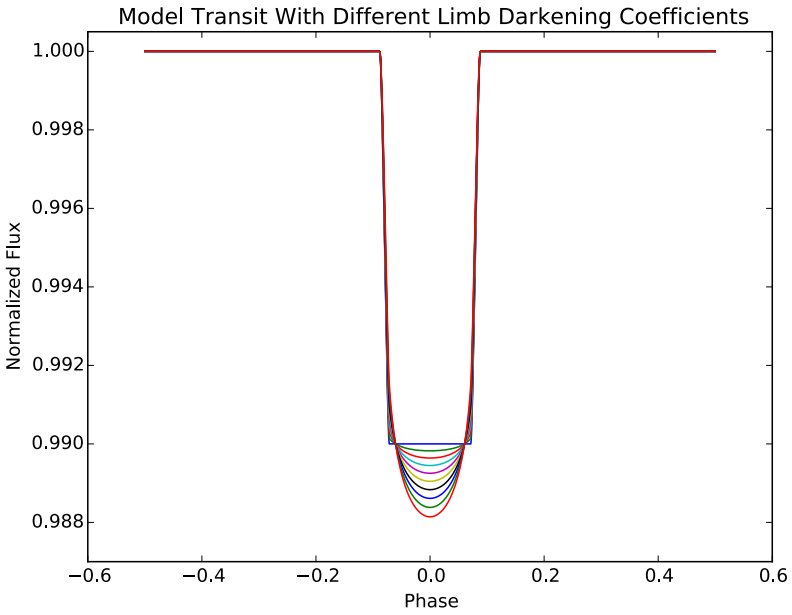

Figure 2.3: Limb darkening effects significantly change the shape of the transit curve bottom. This transit was modeled with various quadratic limb darkening coefficients from 0.25-0.45, with 0.26, 0.25 for the model with the flattest bottom and 0.45, 0.44 for the model with highest curvature at the transit bottom. Determining the correct limb darkening coefficient for each target is important to achieving a viable fit.

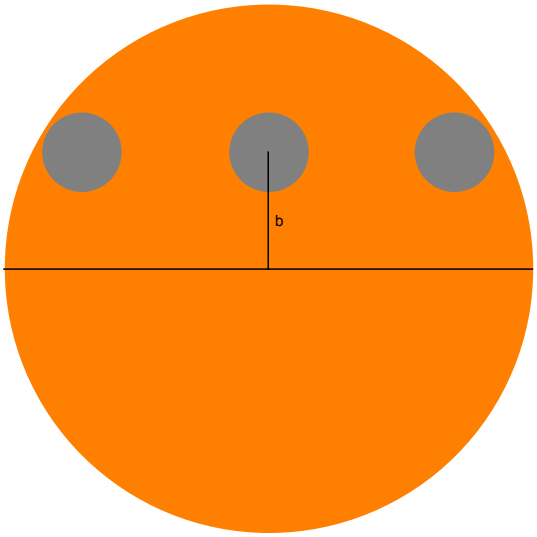

Figure 2.4: Illustrates the impact parameter for a 1.1 Jupiter mass planet (grey) transiting a 0.8 solar radii K star (orange). The impact parameter measures the offset of the line followed by the planet during transit from the line through the center of the star that is the same length as the stellar diameter. This parameter is crucial for determining transit timing, as well as the shape of ingress and egress in the lightcurve.

$$t_x - t_y = \frac{P}{2\pi\sqrt{1-e^2}} \int_{t_y}^{t_x} \left[\frac{r(f)}{a}\right]^2 df$$

where $r(f)$ is the planet-star distance as a function of true anomaly and df is the true anomaly infinitesimal. Where T_{tot} is the duration of transit from first to fourth contact and T_{full} is the duration of transit from second to third contact, this integral can be simplified for circular orbits as (Winn 2010)

$$T_{tot} = \frac{P}{\pi} \arcsin\left(\frac{R_*}{a}\frac{\sqrt{(1+k)^2-b^2}}{\sin i}\right)$$

$$T_{full} = \frac{P}{\pi} \arcsin\left(\frac{R_*}{a}\frac{\sqrt{(1-k)^2-b^2}}{\sin i}\right).$$

Now that the duration and depth of the transit are known, we can model transits to data to determine absolute exoplanet dimensions and orbital parameters.

Some of these dimensional ratios, such as (Winn 2010)

$$\frac{R_*}{a} = \frac{\pi}{2\delta^{1/4}} \frac{\sqrt{T_{total}^2 - T_{full}^2}}{P} \left(\frac{1 + e\sin(\omega)}{\sqrt{1-e^2}} \right),$$

are important for determining the magnitude of tidal interactions between star and planet. The ratio of the planet radius to semimajor axis ($\frac{R_p}{a}$) determines the total fraction of stellar luminosity received by the planets, thus this ratio is also of interest (Winn 2010). Finally, by assuming a stellar mean density, the planetary density can be calculated as (Winn 2010)

$$\rho_* + k^3 \rho_p = \frac{3\pi}{GP^2} \left(\frac{a}{R_*} \right)^3,$$

which can grant insight into an exoplanet's possible composition, as rock and gas have very different densities, which is why Earth is much more dense than Jupiter or Saturn. The planetary density measured in gas giants is an average between rock and gas densities, but for terrestrial planets the density will likely be distinctly rocky. Determining these different planetary characteristics through analysis of transits has allowed astronomers to make statistical assessments regarding abundances in radius, mass, eccentricity, and other constrained parameters. Because of *Kepler*, modeling transits has granted insight into the attributes of thousands of exoplanets.

2.1.3 Secondary Eclipse

Planet dimensions and characteristics can be better constrained through an analysis of both secondary eclipse and transit rather than analysis of solely the latter. The secondary eclipse depth is a direct function of the exoplanet's thermal

and reflected flux, which can be used to measure the planet's albedo and dayside temperature. The contribution of these individual fluxes to the secondary eclipse depth is described by Esteves et al. (2013) as

$$\delta_{eclipse} = \left(\frac{R_p}{R_*}\right)^2 \frac{\int B_\lambda(T_{B,day}) T_K d\lambda}{\int T_K f_{\lambda,*} d\lambda} + A_g \left(\frac{R_p}{a}\right)^2.$$

This provides a powerful constraint on the total combined flux of reflected light and thermal emission. The timing of the secondary eclipse center relative to the transit center, which we will set as phase = 0, is dependent on the system's eccentricity and argument of periastron. The time of mid secondary eclipse can be calculated as

$$t = \frac{P}{2}\Big[1 + 4e\cos(\omega)\Big],$$

which provides an important constraint on eccentricity and argument of periastron. The secondary eclipse duration also constrains these orbital parameters. The equation is the same as that of transit duration, but the impact parameter is

$$b_{occ} = \frac{a\cos(i)}{R_*}\Big(\frac{1-e^2}{1-e\sin(\omega)}\Big),$$

providing yet another measurement of orbital parameters. Figures 2.4, 2.5, and 2.6 illustrate eclipse timing change with respect to eccentricity and argument of periastron, as well as the change in secondary eclipse and transit duration.

2.1.4 Phase Curves

Phase curve flux contributions provide the final details to the model. The total phase effect flux is a combination of flux from reflection, thermal emission,

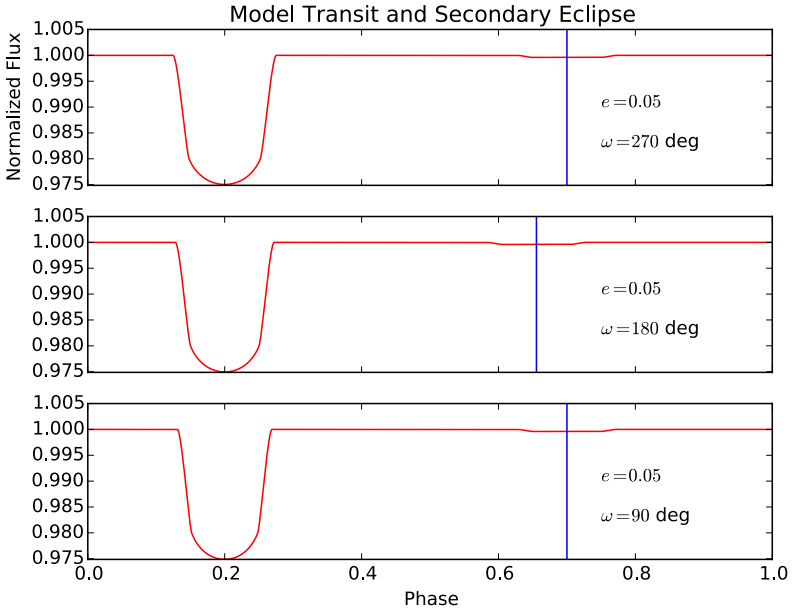

Figure 2.5: Illustrates the change in secondary eclipse timing, duration, and transit duration with respect to eccentricity and argument of periastron (ω). The verticle line goes through the secondary eclipse center. Eccentricity determines the ellipticity of the orbital ellipse, while the argument of periastron determines the orientation of that ellipse relative to the observer. With low eccentricities, the timing of the secondary eclipse shifts by a small amount, though still very measurable. This figure shows the shifting of secondary occultation center with respect to argument of periastron given an eccentricity of 0.05. Note that the duration of the transit also changes with different orientations of eccentric systems, though the effect is not notable here.

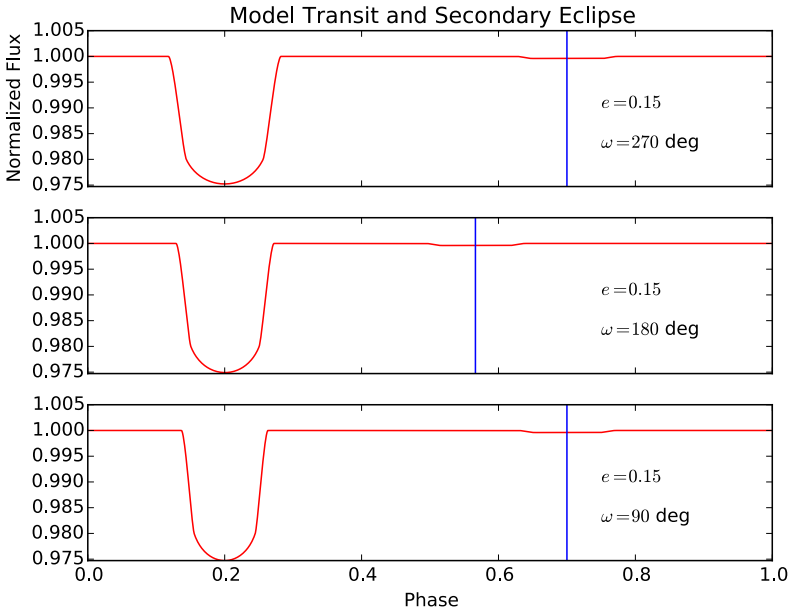

Figure 2.6: Illustration of the shifting of secondary eclipse occultation center with respect to argument of periastron given an eccentricity of 0.15. The verticle line goes through the secondary eclipse center. Clearly the orientation of the ellipse matters more for secondary eclipse timing given a larger eccentricity, thus ω has a greater impact. Note that the duration of the transit also noticeably changes with different orientations of eccentric systems.

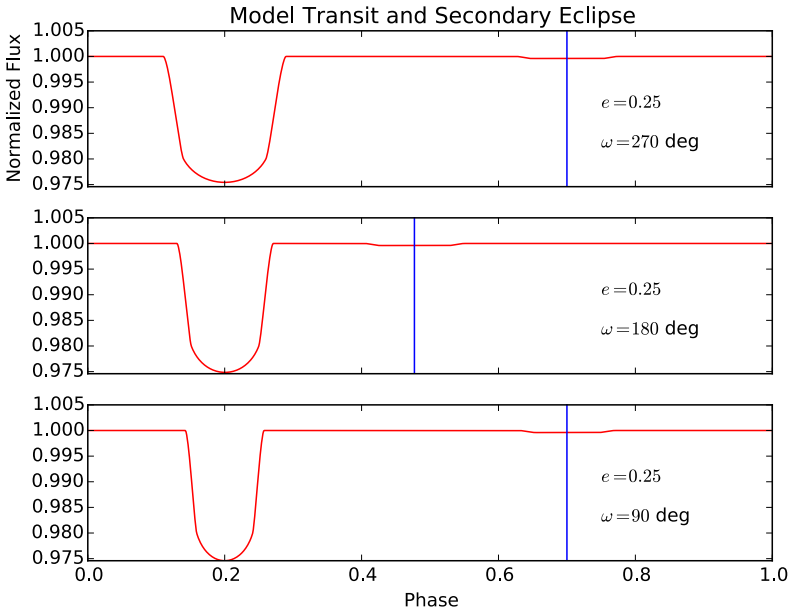

Figure 2.7: This figure illustrates the shifting of secondary eclipse occultation center with respect to argument of periastron given an eccentricity of 0.25. The verticle line goes through the secondary eclipse center. Note that the duration of the transit and eclipse also noticeably change with different orientations of this eccentric system.

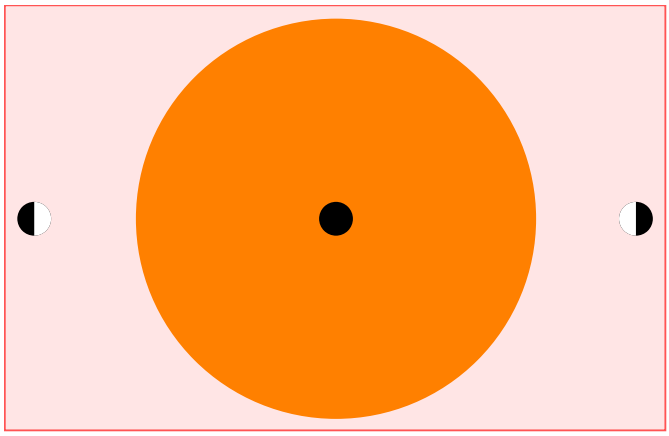

Figure 2.8: Illustrates the changing phases of an exoplanet that produce the reflected flux phase curve. The white parts of the planet are reflecting, while the black regions are not. During transit, the planet is in new phase.

ellipsoidal variations, and Doppler beaming. Characterizing an exoplanet's phase curves provides information regarding atmospheric temperature, albedo, orbital properties, and nondegenerate mass and inclination measurements.

Reflected Flux

The reflected flux from an exoplanet comes from starlight striking the planet's atmosphere and bouncing towards the line of sight of the observer. The change in reflected flux with phase is the same as the shifting phases of Earth's moon. During transit, the planet is in new phase, as the entire portion of the planet reflecting starlight is facing away from us. The planet enters full phase during secondary occultation, but will approach the full phase before first contact of the secondary eclipse. Figure 2.8 illustrates how reflection from an exoplanet changes with time.

The total amount of reflected flux at a specific time during the orbital phase is calculated as (Mislis et al. 2012; Placek et al. 2014)

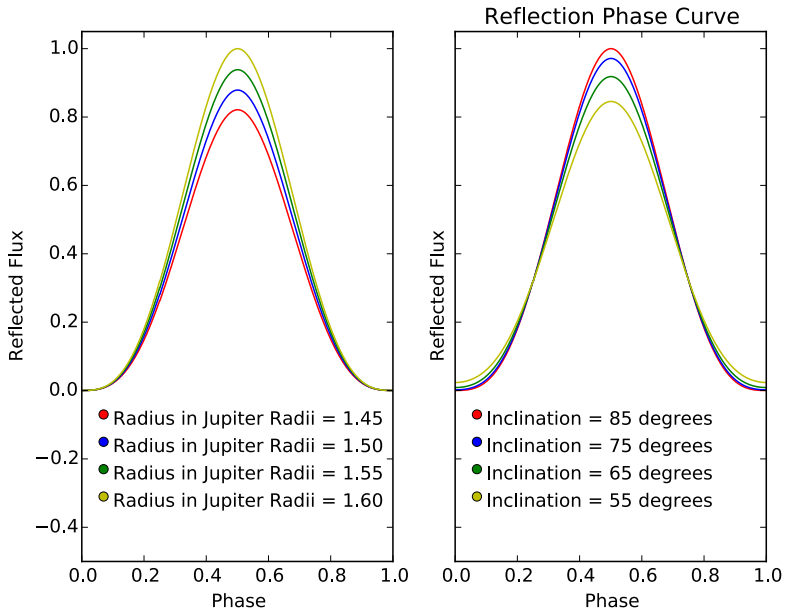

Figure 2.9: Reflected flux phase curve over a single phase. On the left plot, the colors correspond to models run with different planetary radii. On the right, the colors correspond to models run with different inclinations. The peak of the reflected flux is blocked out during secondary eclipse, thus that part of the curve is not observed.

$$\frac{F_{reflected}(t)}{F_*} = \frac{A_g}{2}\frac{R_p^2}{[d(t)]^2}[1 + cos\theta(t)],$$

where A_g is the geometric albedo defined as the ratio of reflected flux from the exoplanet's atmosphere at full phase and the reflected flux from a Lambertian disk of equal cross-sectional area (Burrows and Orton 2011). Lambertian disks are perfectly flat and diffusing surfaces, therefore the closer A_g is to 1, the more perfectly reflective the planet's atmosphere. The reflected flux equation is also partly used in calculation of the secondary eclipse depth.

Examples of reflected flux phase curves are shown in Figures 2.9 and 2.10. These figures also show how the shape of the reflective flux phase effect changes through the shifting of a single orbital parameter (R_p, e, i, A_g).

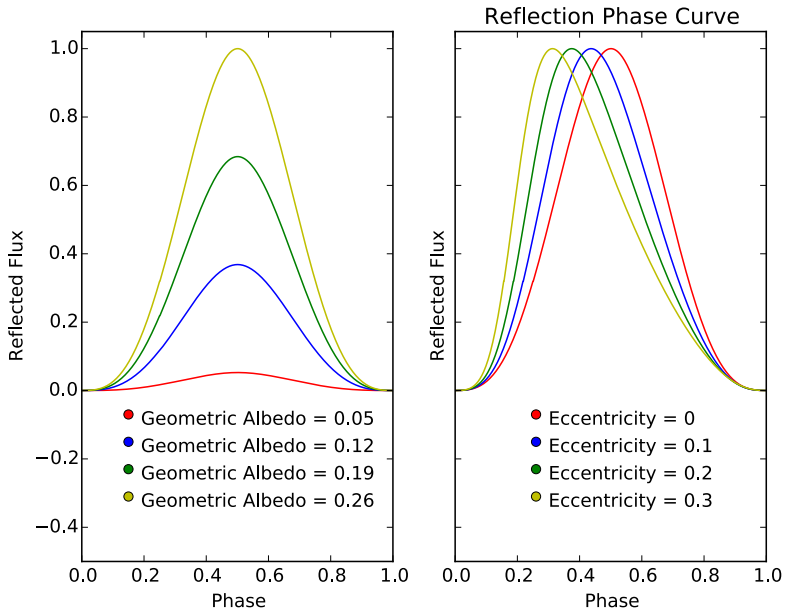

Figure 2.10: Shows the reflected flux phase curve over a single phase. On the left plot, the colors correspond to models run with different geometric albedo. On the right, the colors correspond to models run with different eccentricity.

Thermal Emission Flux

Most objects for which phase curve analysis is viable are tidally locked to their host stars, as making a planet hotter and moving it closer to its star amplifies the magnitude of the system's phase effects. As such, many have permanent day and nightsides, which have different temperatures. Winds can provide a mechanism for smoothing this temperature gradient, but the planet will still have a zone of maximum temperature, which will emit more thermal flux than cooler sections. The variation in phase of the thermal emission curve comes from this hot zone coming in and out of view throughout the course of the orbit. The emission is thought to be at maximum during the full phase, at which time light from the planet is blocked during the secondary eclipse. The maximum temperature seen by the observer is thus thought to come immediately before ingress and after

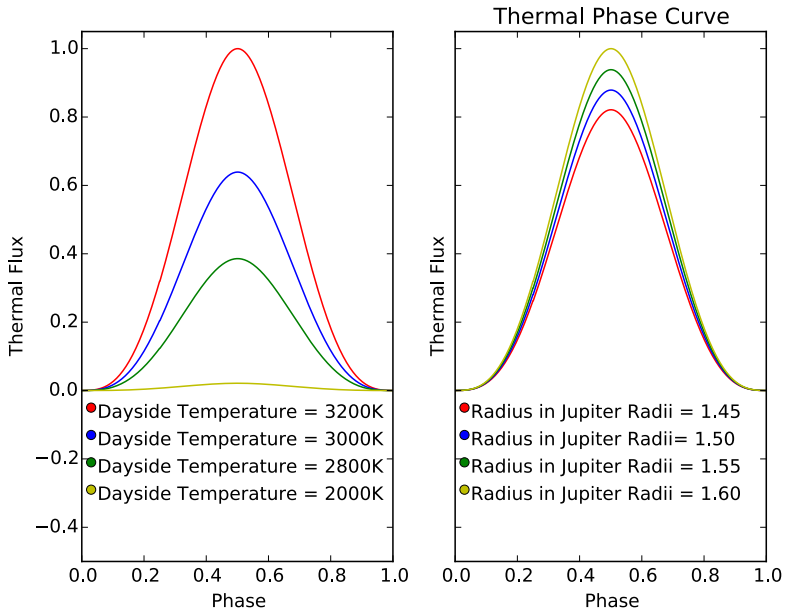

Figure 2.11: Thermal flux phase curve over a single phase. On the left, the different colors correspond to different dayside temperatures for the same planet. On the right, the different colors correspond to different radii for the same planet.

egress of the secondary eclipse.

Thermal flux contribution is calculated as (Placek et al. 2014)

$$\frac{F_{thermal,day}(t)}{F_*} = \frac{1}{2}\left[1 + \cos\theta(t)\right]\left(\frac{R_p}{R_*}\right)^2 \frac{\int B(T_{day})G(\lambda)d\lambda}{\int B(T_{eff})G(\lambda)d\lambda},$$

where $B(T_{day})$ is the Planck function for the planet, $B(T_{eff})$ is the Planck function for the star, and $G(\lambda)$ is the *Kepler* response function at wavelength λ (Van Cleve 2009). This equation also contributes to the final calculation of eclipse depth, which is the sum of both this thermal flux and the aforementioned reflected flux. Figures 2.11 and 2.12 show the flux contribution from the thermal phase effect, as well as its change with respect to a single parameter (e, i, R_p, and dayside temperature).

The individual contributions between thermal and reflected flux from the ex-

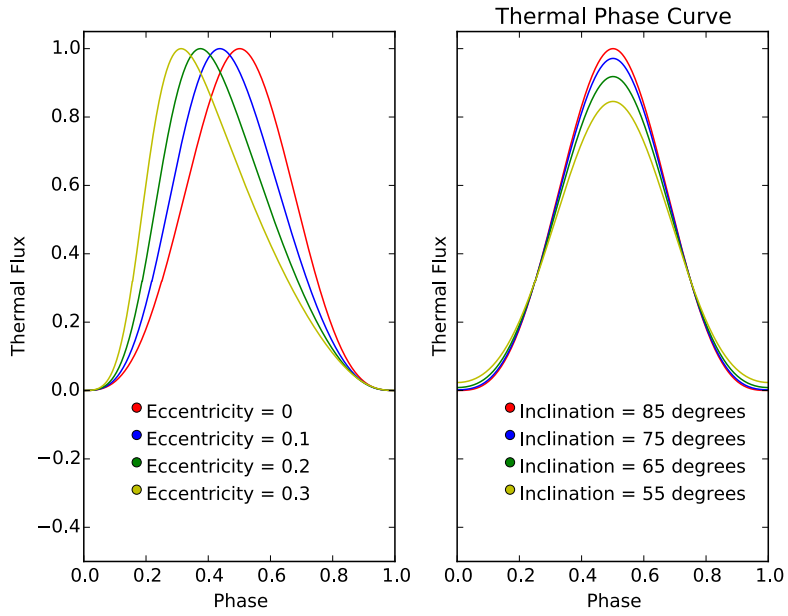

Figure 2.12: Thermal flux phase curve over a single phase. On the left, the different colors correspond to different eccentricities for the same planet. On the right, the different colors correspond to different inclinations for the same planet.

oplanet are difficult to measure, making the geometric albedo and dayside temperature degenerate parameters. This is a considerable problem for single-band photometric phase curve analysis that remains to be resolved.

Looking at Figures 2.9-2.12, it is easy to see why planetary temperature and geometric albedo are degenerate parameters, as the thermal and reflected flux phase curves are nearly identical in structure. This can often lead one value being depressed and the other inflated upon output from the model. Developing a means to break this degeneracy would greatly improve the robustness of single band photometric phase effect analysis. Exoplanetary winds may be a mechanism for shifting the hot zone in some specific cases, thus breaking this degeneracy.

Ellipsoidal Variations Flux

Ellipsoidal variations are a gravitational effect caused by the exoplanet's gravitational pull warping the star from its generally spherical shape to that of an ellipsoid. The bulge induced by this gravitational warping follows the orbit of the planet, meaning the solid angle of the star seen by the observer changes as this bulge rotates during the phase. The flux contribution from ellipsoidal variations and its change in phase is calculated as (Placek et al. 2014)

$$\frac{F_{ellipsoidal}(t)}{F_*} = \beta \frac{M_p}{M_*} \left[\frac{R_*}{d(t)}\right]^3 \left(\cos^2[\omega + f(t)] \cos^2(i) \right)$$

where β is the gravity darkening exponent calculated as (Mislis et al. 2012)

$$\beta = \frac{log_{10}(GM_*/(R_*)^2)}{log_{10}(T_{eff})}$$

which changes with stellar mass and radius, planet mass, and parameters to characterize the 3D orbit of the exoplanet. This is one of the phase effects that helps constrain the mass parameter. Figure 2.13 shows the shape of this phase curve, as well as its change with respect to planet mass, eccentricity, and inclination.

These sinusoidal variations have a significantly shorter period than those of the Doppler beaming effect discussed below, therefore these two phase effects are not degenerate. Minor asymmetries in phase curves on either side of a secondary eclipse often come from asymmetry in the ellipsoidal variation flux sinusoids that increases with greater eccentricity. This can further help to constrain this critical parameter.

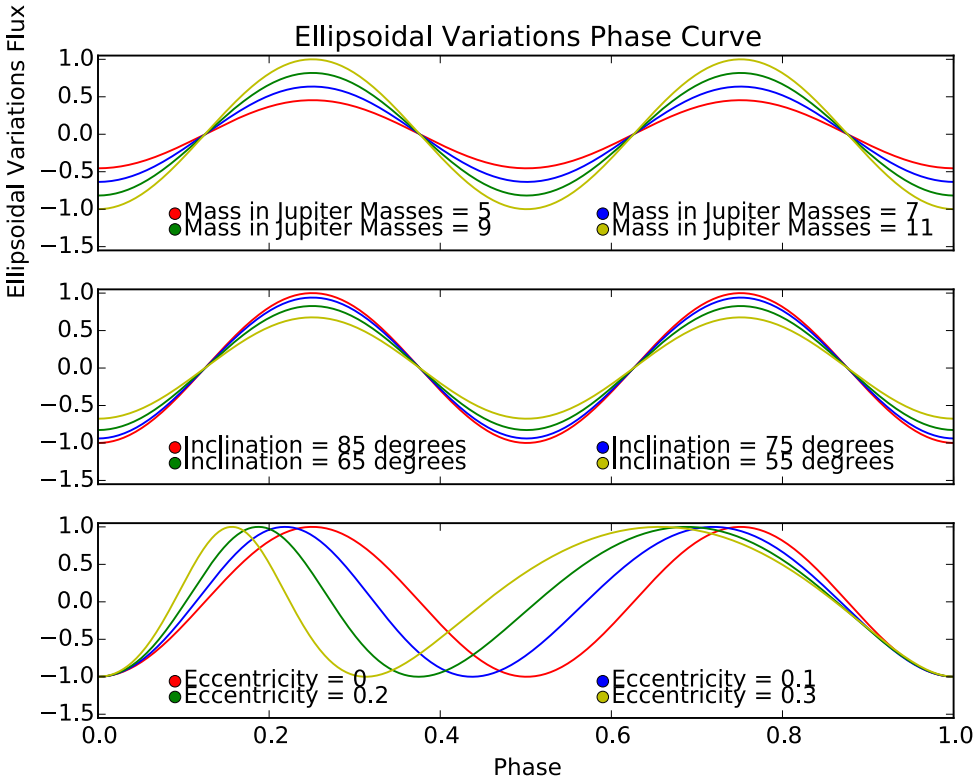

Figure 2.13: Ellipsoidal variations flux phase curve over a single phase. On top, the different colors correspond to different masses for the same planet. In the middle, the different colors correspond to different inclinations for the same planet. On the bottom, the different colors correspond to different eccentricities for the same planet.

Doppler Beaming Flux

Doppler beaming is a relativistic effect caused by redshifting and blueshifting of stellar flux due to movement of particles in the star towards the planet. The flux contribution from doppler beaming is calculated as (Loeb & Gaudi 2003)

$$\frac{F_{beam}(t)}{F_*} = \frac{4v_r}{c}$$

where c is the speed of light in a vacuum and v_r is the radial velocity of star, defined as

$$v_r = V_z + K(\cos[\omega + f(t)] + e\cos(\omega))$$

where V_z is the speed at which the star is traveling relative to the sun and K is the radial velocity semiamplitude, defined as (Lovis & Fischer 2010)

$$K = \frac{28.4329}{\sqrt{1-e^2}} \frac{M_p \sin i}{M_{Jup}} \left(\frac{M_* + M_p}{M_{Sun}}\right)^{-1/2} \left(\frac{a}{1AU}\right)^{-1/2}$$

where a is the semimajor axis, or (Lovis & Fischer 2010)

$$K = \frac{28.4329}{\sqrt{1-e^2}} \frac{M_p \sin i}{M_{Jup}} \left(\frac{M_* + M_p}{M_{Sun}}\right)^{-2/3} \left(\frac{P}{1yr}\right)^{-1/3}$$

where P is the period.

The shape of the Doppler beaming phase curve is illustrated in Figure 2.14, as well as its change in shape with respect to planet mass, eccentricity, and inclination.

The sinusoid of this phase effect is distinct from that of ellipsoidal variations due to its longer period. Doppler beaming is an important phase effect for con-

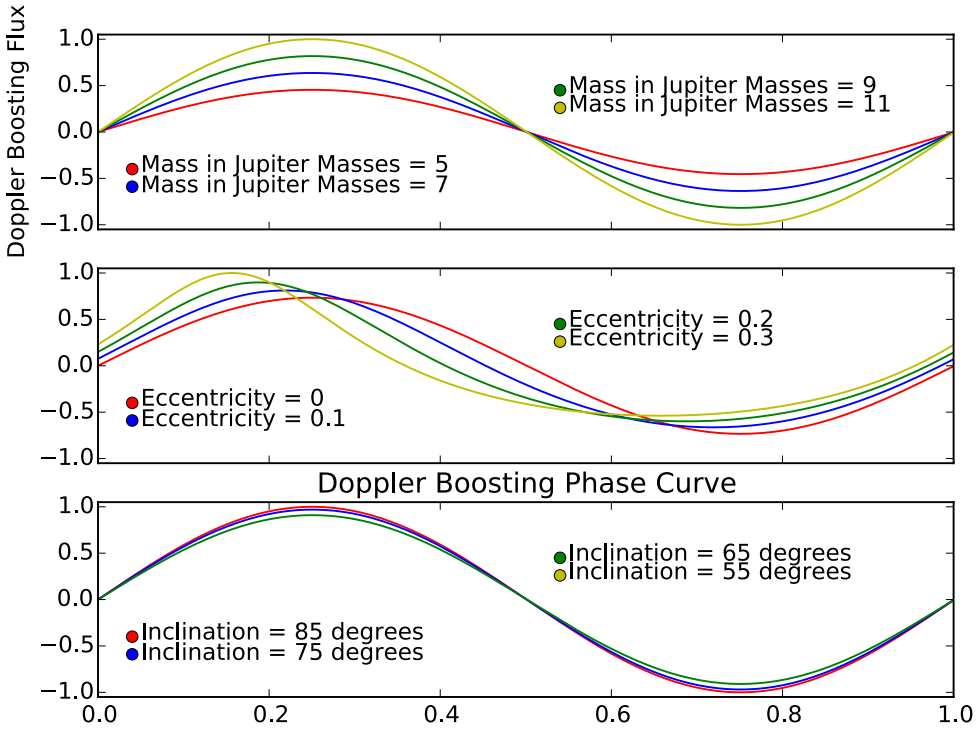

Figure 2.14: Doppler boosting flux phase curve over a single phase. On top, the different colors correspond to different masses for the same planet. In the middle, the different colors correspond to different eccentricities for the same planet. On the bottom, the different colors correspond to different inclinations for the same planet.

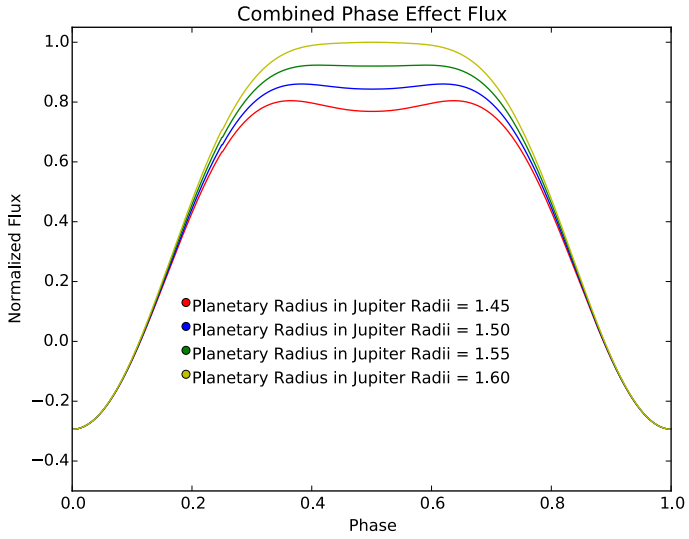

Figure 2.15: Illustrates the combined phase curve flux from all four effects, with different colors corresponding to different radius values. The planetary radius affects the magnitude of the phase curves as well as the curvature of the phase curve peak.

straining the exoplanet's mass, inclination, and eccentricity. Constraint of Doppler beaming flux contributions complements constraint of ellipsoidal variation contributions, both of which constrain the same planetary parameters.

Combined

Figures 2.15-2.18 show combinations of different phase curves, as well as their change with respect to specific parameters. Most parameters have a distinct effect on the overall shape of the phase curves. In some cases, high temperatures can wash out all the gravitational phase effects by becoming overwhelmingly high in amplitude. In Figure 2.17, it is apparent that at high temperatures the amplitude of the thermal phase effect becomes strong enough to overpower the remainder of the effects. The reflective phase curve exhibits this same behavior with respect to the albedo parameter, meaning that when combined, the phase effects of an extremely reflective exoplanet atmosphere may appear to be dominantly, even

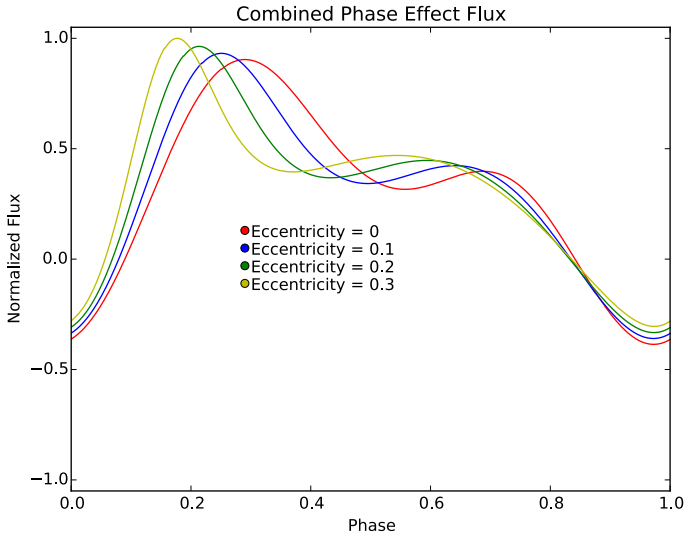

Figure 2.16: Illustrates the combined phase curve flux from all four effects, with different colors corresponding to different eccentricity values. It is apparent that eccentricity produces significant asymmetries in the flux from phase effects over a single phase.

solely, reflective. The eccentricity term serves to pull the peaks of each phase curve towards either the left or right of the phase, depending on the argument of periastron, as illustrated in Figure 2.15. The maxima of the thermal and reflective phase curves shift in the same direction with respect to phase, while the maxima and minima of the gravitational phase effects both shift in the same direction. The gravitational phase curves become compressed in the direction in which they are pulled by the eccentricity term and expanded on the opposite end of the phase from which they are pulled, as is apparent in Figure 2.15.

Inclination affects all four phase effects in a similar way –it simply reduces each of their amplitudes as it moves towards 0° from 90°, as is apparent in Figure 2.9, 2.12, 2.13, 2.14, and 2.16. The inclination is also heavily constrained by fitting the transit, so this specific parameter is generally well characterized by our model. The radius, too, is well characterized by the transit, though increasing it affects the phase curve shape in a similar way to increasing temperature or albedo. As

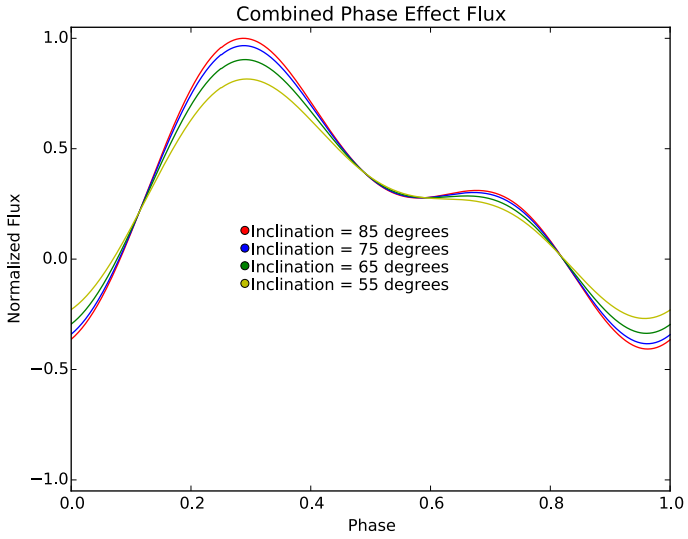

Figure 2.17: Illustrates the combined phase curve flux from all four effects, with different colors corresponding to different inclination values. It is apparent that changing the inclination significantly impacts the magnitude of flux from the phase effects.

is apparent in Figure 2.18, increasing the radius washes out the bimodal shape of the combined phase curve that is induced by the contribution of gravitational phase effects. This is similar to the overwhelming of gravitational effects by high temperatures discussed in the previous paragraph. This triple parameter degeneracy between albedo, temperature, and planetary radius would be a significant challenge for any fitting algorithm. However, with addition of transit modeling to our analysis, this is reduced to a double parameter degeneracy, which is far more manageable.

Many exoplanet systems exist that do not show each individual phase effect. For systems with small, hot planets orbiting close to their host star, such as Kepler-7 b, the only present phase effects appear to be reflective and thermal in nature, as the gravitational components are not of high enough amplitude to contribute noticeably to the overall shape of the phase curve. This may potentially make planetary mass harder to measure. For systems with similar temperatures

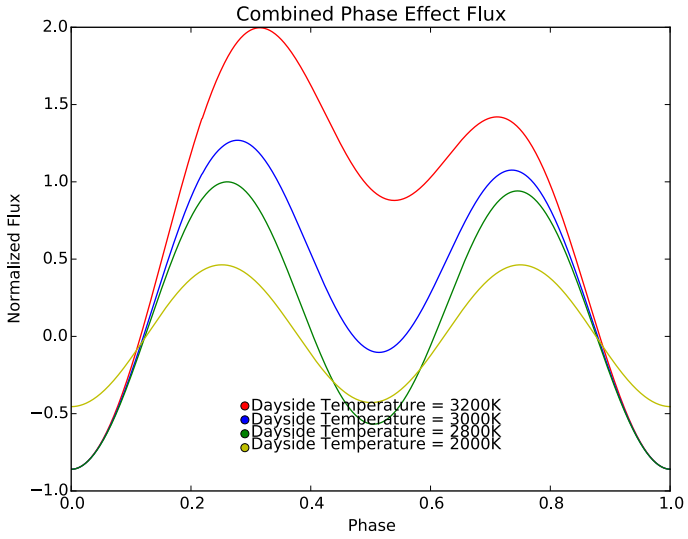

Figure 2.18: Illustrates the combined phase curve flux from all four effects, with different colors corresponding to different dayside temperature values. The dayside temperature clearly impacts the magnitude of flux from the combined phase curves, though this only changes the thermal flux phase curve.

but considerably higher mass, such as Kepler-5 b, the dominant phase effects are clearly gravitational in shape. Phase curves for both of these specific systems will be modeled in Chapter 4 of this thesis. For another informative description of modeling phase effects, see Serindag (2015).

Chapter 3

Fitting

Fitting algorithms are designed to assess the fit of a model to a dataset and adjust parameters to move towards a better fit with fewer residuals, a term used to describe the numerical difference between the model and data. We are attempting to fit the transit, secondary eclipse, and all four phase effects simultaneously by integrating them into a single model that can be assessed for agreement to data. The amplitude of the transit is far greater than that of the secondary eclipse or phase curves, so this part of model immediately provides a strong constraint on radius and inclination. After this, other planetary parameters shift throughout the course of the fitting process until they eventually settle at their best fit values. These best fit values thus provide measurements for temperature, albedo, mass, eccentricity, and argument of periastron.

A paramount fundamental problem facing fitting routines is that of parameter degeneracy, which describes parameters that produce nearly identical effects on the overall shape of the model when adjusted. For the phase curve model alone, planetary radius, temperature, and albedo are all degenerate parameters, since adjusting one has a similar effect on the phase curve amplitude as adjusting either of the other two, as shown in Figure 3.1. This often leads to one or more of these values being depressed while their fellow degenerate parameters are increased to unphysical levels. To combat this, we run multiple models that encompass all pos-

sible combinations of the four phase effects, as well as the possibility of none of the effects being present. This serves to lessen the dimensionality of parameter space while simultaneously eliminating degenerate parameters pairings in some models. Furthermore, addition of more constraints to the model can eliminate parameter degeneracies. In our case, the addition of transit analysis to our assessment gives us another probe for the radius value, thereby eliminating the aforementioned degeneracy, as is shown in Figure 3.1. Without this additional transit constraint, planetary albedo, temperature, and radius would be triple degenerate parameters. It is clear why temperature and albedo are degenerate parameters, as they can be used interchangeably to produce the same effect. The difference between a bright, cool planet and a dark, warm planet, is difficult to determine. Perhaps a convenient way of constraining this degeneracy would be to calculate a minimum expected temperature based on flux received from the star at the planet's orbital distance. The temperature could potentially be warmer than this, assuming the atmosphere traps heat, but would not go beyond this lower bound. We will implement this constraint in future models.

Another major issue encountered by fitting algorithms lies in guaranteeing the program will actual find the best fit values of a global minimum in residuals rather than values that correspond to a local minimum in residuals. If a fitting program goes to a local minimum in residual values, the gradient of residual space can trap the algorithm in this "well". To escape, the gradient of residual space must somehow be lessened through a process called parallel tempering (Earl & Deem 2005; Foreman-Mackey et al. 2013). If the fitting routine cannot escape, it will output incorrect parameter values that correspond to a local minimum in residuals rather than a global minimum. We will use two different implementations of the Markov Chain Monte Carlo fitting algorithm in an effort to resolve these issues.

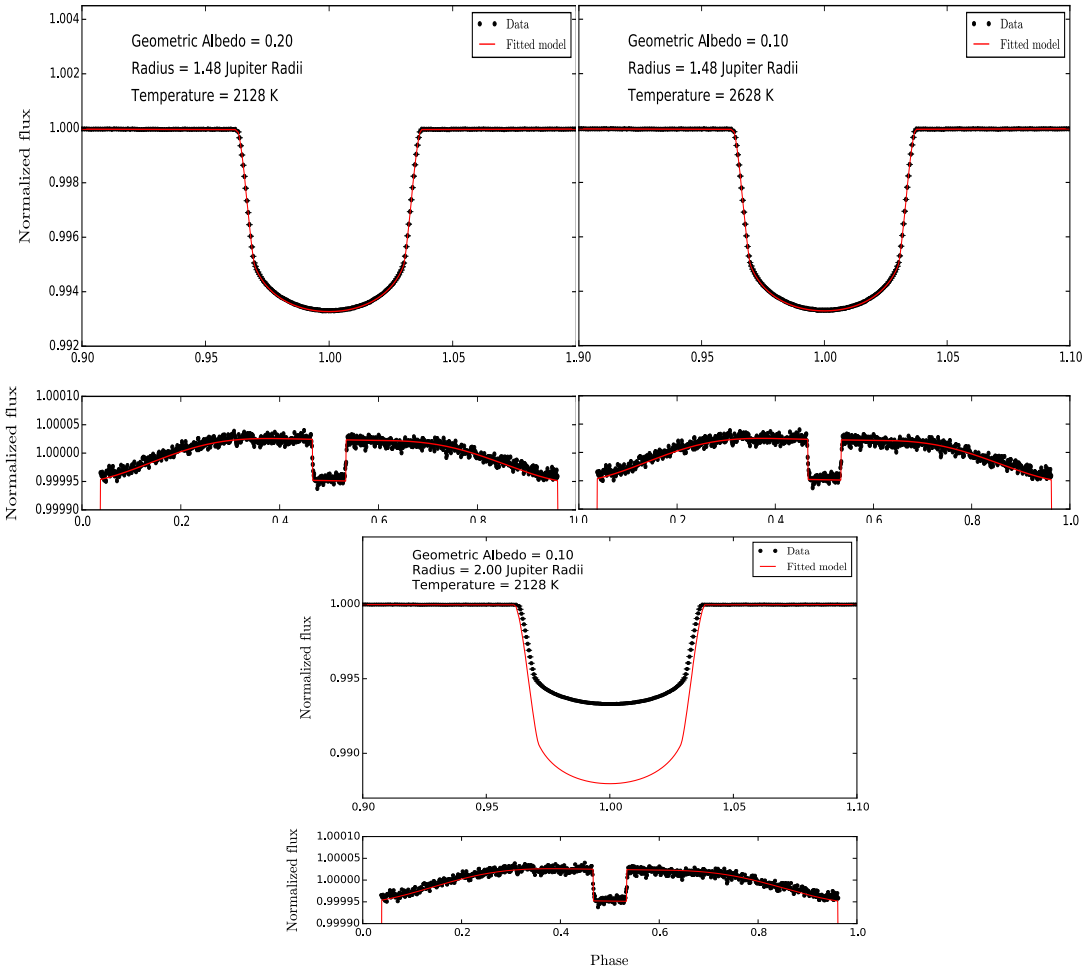

Figure 3.1: For HAT-P-7 b. Illustrates how the triple degeneracy between albedo, planetary temperature, and planetary radius is broken by including the transit in modeling and fitting process. Though the phase effects and secondary eclipse appear to be essentially indistinguishable between the three plots, each of which uses a different combination of these three parameters, the difference in the transit portion of the model induced by adjusting the radius is obvious. This allows us to reduce the triple degeneracy to a double degeneracy between albedo and temperature.

3.1 Markov Chain Monte Carlo

The Markov Chain Monte Carlo (MCMC) (Ivezić et al. 2014) is our favored fitting method for this model. It consists of applying the Monte Carlo process of moving walker chains based on posterior probability density distributions. Walkers are individual probes of parameter space that move upon every iteration of the fitting program. Most fitting algorithms that utilize posterior probability density distributions depend heavily on its thorough and detailed constraint. The MCMC is designed to sample and provide approximations to posterior probability density even in systems dependent on a large number of parameters (Foreman-Mackey et al. 2013).

3.1.1 Metropolis-Hastings algorithm

The Metropolis-Hastings (MH) implementation of the MCMC centers the walkers in a compact distribution around the currently existing chain of walkers (Ivezić et al. 2014; Foreman-Mackey et al. 2013). It has $N[N+1]/2$ tuning parameters, where N is the number of dimensions comprising parameter space. The algorithm is highly sensitive to the values of these numerous parameters, many of which cannot be properly estimated before implementing the fitting routine. For this reason, we will implement a more efficient and capable version of the MCMC that utilizes affine invariant sampling.

3.1.2 Affine invariant sampling

The affine invariant sampling MCMC (Goodman & Weare 2010; Foreman-Mackey et al. 2013) links together the position of two random walkers across

parameter space. Each step taken by one walker is selected from a proposal distribution connecting its position in parameter space to its partner's. This is particularly useful for probing anisotropic probability distributions with high numbers of dimensions. The classic problem faced by many probability density sampling routines is commonly visualized as a highly anisotropic probability density, defined as (Foreman-Mackey et al. 2013)

$$\pi(x) \propto \exp\left(- \frac{(x_1 - x_2)}{2\epsilon} - \frac{(x_1 + x_2)^2}{2} \right),$$

where ϵ is a proportionality constant (Goodman & Weare 2010). This definition of probability density is sensitive to parameter constraints of N^2 parameters, which makes this problem much worse with higher dimensions (Foreman-Mackey et al. 2013). The problem can be simplified by the affine transformation of $y_1 = \frac{x_1 - x_2}{\sqrt{\epsilon}}$, $y_2 = x_1 + x_2$ (Goodman & Weare 2010; Foreman-Mackey et al. 2013; Ivezić et al. 2014), which is conducive to affine invariant sampling, capable of performing well under all linear transformations, helping to reduce sensitivity to degeneracy between parameters. This sampling method also allows the walkers to take nonorthogonal steps, which quickens their convergence to the best fit value. Flaherty et al. (2015) favor an affine-invariant routine MCMC over the Metropolis-Hastings algorithm, as it reduces significant degeneracies between parameters that would otherwise prove problematic for their protoplanetary disk turbulence model. Hou et al. (2012) use an affine invariant sampler to fit radial velocity data for exoplanet detection and characterization. This sampling approach is hundreds of times faster than a comparable Metropolis-Hastings MCMC, which makes this affine invariant fitting method far more applicable to large datasets. Overall, the affine invariant sampler is superior to the Metropolis-Hastings algorithm in

terms of speed and accuracy in probing posterior probability distribution functions subject to strong parameter degeneracies.

Affine invariant sampling is weak when probability distributions take on a multi-modal form, which is indicative of a local maximum within the distribution. Large groupings of these walkers can congregate at these local maxima due to the nature of their collective movement and convergence, as walkers are linked, unlike in other sampling methods. If such a large grouping of walkers develops, the other walkers will likely trek towards this incorrect solution, causing the model to output false parameters. Alternatively, groups of walkers can build up at multiple local maxima, which confines their movement to a line connecting the two peaks Ivezić et al. (2014). The probability distributions used by our fitting algorithm are often characteristically multi-modal. For this reason, solely affine invariant sampling will not be sufficient for our fitting algorithm. Now, we must include a parallel-tempering algorithm to give the walkers more chance of overcoming gradients of parameter space that crowd them to local maxima.

3.1.3 Parallel tempering algorithm

The parallel tempering MCMC (Earl & Deem 2005; Foreman-Mackey et al. 2013) deals with the local maxima issue in affine invariance sampling by running multiple MCMCs at different "temperatures". Turning up the temperature flattens parameter space, which enables walkers to overcome probability gradients that would otherwise be insurmountable. Furthermore, it exchanges walkers between these different temperatures, which propagates this increased walker freedom to the lower temperature MCMCs. Parallel tempering takes care of the primary issue with affine invariant sampling, therefore our fitting algorithm is now

capable of dealing with the anisotropy, high dimensionality, and multi-modality of the probability distributions that it will analyze. We use the parallel-tempering MCMC from the `emcee` Python library (Foreman-Mackey et al. 2013). For additional informative discussion of the advantages of this fitting method for this specific probability density distribution type, see Serindag (2015).

Chapter 4

Results

In order to test the effectiveness of our model in generating accurate lightcurves, we run it on four different *Kepler* exoplanets –Kepler-5 b, Kepler-6 b, Kepler-7 b, and HAT-P-7 b. In order to do this, we first had to run the *Kepler* data through a reduction process. Then, our MCMC generates models and fits them to the data, adjusting parameter values until they, ideally, reach the actual values of the exoplanetary system.

Testing our modeling and fitting process on four real *Kepler* exoplanets illuminates their strengths and weaknesses. The most prominent weakness made apparent by these tests is in the secondary eclipse modeling. We obtained our secondary eclipse model from the code made public by Crossfield (2012). This particular secondary eclipse model does not include the ingress and egress of the secondary eclipse, just its bottom. This leads to multiple data points measuring secondary eclipse ingress and egress being poorly fit, which throws off the fitting routine. If this modeling error is resolved, our fitting routine will likely be able to accurately characterize the entire lightcurve to a χ^2 of < 2. Alternatively, if our fitting process is unable to output realistic temperature and albedo parameters upon resolution of the secondary eclipse ingress and egress issue, there is likely a deeper issue in our calculation of the thermal and reflective phase curves as well as the secondary eclipse depth.

Because the Crossfield (2012) model does not address secondary eclipse ingress and egress, we will need to construct our own in the future. The χ^2 values for our fitting all exceed 17, which means they are not statistically significant fits, though they may appear to be by eye. This could also mean that our model is underestimating errors or is not a complete description of the system, which is likely due to this slight shortcoming in the secondary eclipse model. We will display and discuss the output parameters from our real exoplanet tests from the best fit, lowest χ^2 models, though the χ^2 is still not low enough to make these results statistically significant. We also present "triangle" plots from the runs, which illustrate the movement of our MCMC walkers through different dimensions of parameter space. Finally, we show the lightcurve fits and their residuals.

4.1 Kepler Exoplanets

4.1.1 Data Reduction

The portion of our data reduction routine that reduces secondary eclipse and phase curve sections of *Kepler* data is the same one constructed and employed by Serindag (2015), but without the occultation clipped out before processing. A new code was written to reduce the transit sections of the data, which were seeing a deviation in transit depth from literature values out after undergoing the same reduction process as the secondary eclipse and phase curves. A new transit data reduction routine was constructed. It uses literature values for planetary parameters to clip the transit portion of the lightcurve, grabbing a comfortable margin of data points before ingress and after egress, though these data points were not removed from secondary eclipse-phase effect section of the lightcurve. A spline function was then fit between the collection of data points before and

after each transit. The same spline was calculated for the in-transit portion of the lightcurve, then the in-transit data points were divided by the spline. After this, the data were phase folded.

Provided all input data are short-cadence *Kepler* datasets, this produces transits, secondary eclipses, and phase curves datasets of comparable quality to those seen in literature (Kipping & Bakos 2011; Gostev 2011; Esteves et al. 2013; Esteves et al. 2015; Placek & Knuth 2015). However, the degree to which phase curve effect magnitude is weakened with exclusion of long-cadence *Kepler* data must be better characterized in the future. Long-cadence data is better for detecting weak phase-long signals, like phase curves, while short cadence data is superior for detection of strong and short-term signals, like transits or, less so, secondary eclipses. The optimal solution to this potential issue is to modify the data reduction program so that it uses only short-cadence data for all of the transit data reduction, but still processes the long cadence data in the phase-curve/secondary eclipse portion of the reduction.

4.1.2 Kepler-5 b

Table 4.1: Kepler-5 b: Fixed Parameters. R_* is the stellar radius, M_* is the stellar mass, T_* is the stellar temperature, a and b are the quadratic limb darkening coefficients, g is the gravity darkening coefficient, and P is the period.

Parameter	Value	Reference
R_* $[R_\odot]$	1.793	Koch et al. (2010)
M_* $[M_\odot]$	1.374	Koch et al. (2010)
T_* $[K]$	6297	Koch et al. (2010)
a,b	0.368,0.142	Müller et al. (2013)
g	0.2915	Koch et al. (2010)
$P[days]$	3.54846	Koch et al. (2010)

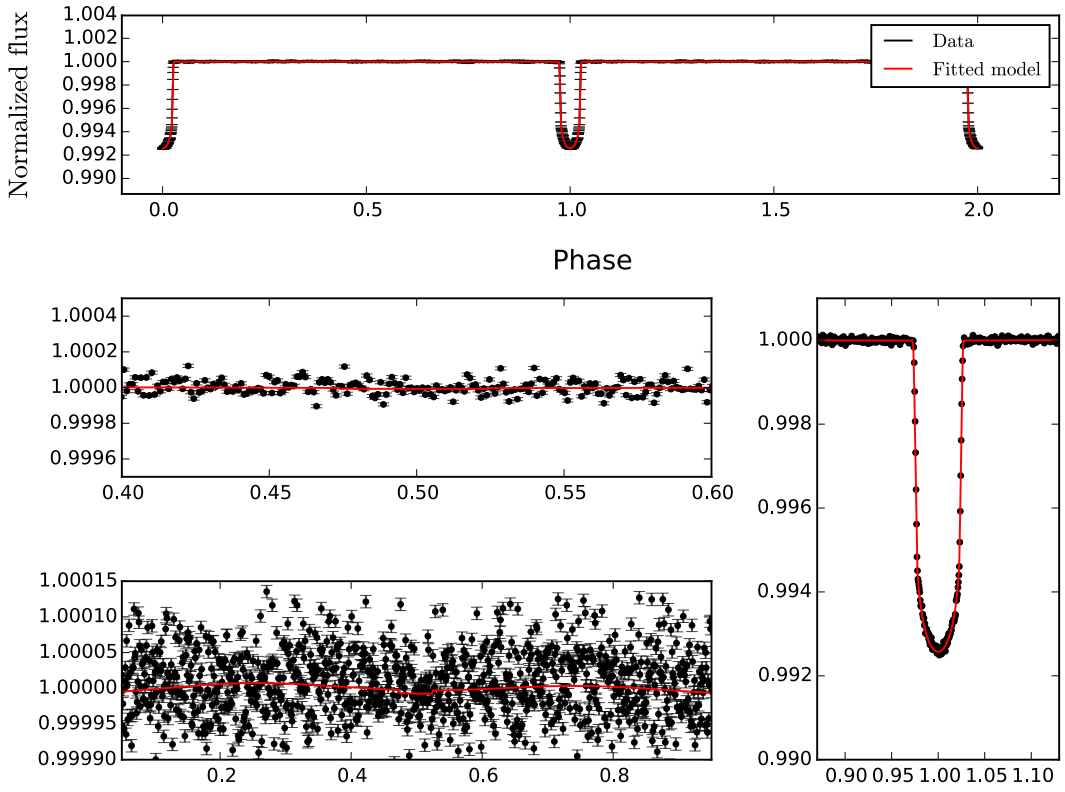

Figure 4.1: Illustrates the data (black) and ReThElDo model lightcurve (red) for Kepler-5 b. (above) Two phases of the planet's orbit. This illustrates how the transit and secondary eclipse events occur continuously. The small horizontal bars are error bars. (middle left) The secondary eclipse section of the phase. This is the section of the phase around $\phi = 0.5$. (bottom left) The entire phase at a scale in which the phase effects are visible. This scale is, of course, extremely small, as phase effects are the lowest magnitude of all flux variations. (bottom right) Transit fit. This is clearly the largest feature in every light curve, which allows for very precise constraint of planetary radius and inclination.

The 20 walker 500 step run for Kepler-5 b demonstrates many interesting successes and issues in our model. As shown in Figure 4.1, the overall fit to the data looks excellent. However, some of our ouput parameter values do not agree with those in the literature. As shown in Table 4.2, for the ReThElDo model, the fitting successfully constrains the eccentricity, mass, and planetary radius to values that agree with those in Esteves et al. (2013). The best fit value is the parameter associated with the model of lowest χ^2 and the median value is the one walkers spent the most time at during the fitting process. The error bars are a measure of the distribution of walker positions around the median value. The derived mass for our planet is closer to the minimum mass measured by radial velocity techniques than those in Esteves et al. (2015). The inclination does not agree with phase curve analysis literature values (Esteves et al. 2013; Esteves et al. 2015), but does agree with transit analysis literature values (Kipping & Bakos 2011). The geometric albedo and temperature are not in agreement with any literature values. Furthermore, the degeneracy between these parameters is demonstrated by our ThElDo model, which does not include reflection, producing a comparable χ^2 value to the ReThElDo model that contains all four phase effects, as shown in Table 4.2.

Table 4.2: Kepler-5 b: ReThElDo Model $\chi^2 = 33.12$. 20 walkers 500 steps

Parameter	Best Fit	Median	Accepted Value	Reference
e	0.002	$0.001^{+0.001}_{-0.001}$	0^a	Esteves et al. (2015)
i [deg]	86.79	$86.753^{+0.004}_{-0.003}$	86.3 ± 0.5	Kipping & Bakos (2011)
ω [rad]	2.31	$2.99^{+0.05}_{-0.07}$	...	Esteves et al. (2015)
M_p [M_J]	1.50	$1.08^{+0.19}_{-0.13}$	$0.92^{+0.93}_{-1.02}$	Esteves et al. (2015)
R_p [R_J]	1.408	$1.4065^{+0.00015}_{-0.00008}$	$1.431^{+0.041}_{-0.052}$	Esteves et al. (2015)
A_g	0.026	$0.016^{+0.004}_{-0.005}$	$0.121^{+0.034}_{-0.036}$	Esteves et al. (2015)
T_{day} [K]	1497	1590^{+70}_{-96}	2390^{+80}_{-100}	Esteves et al. (2015)

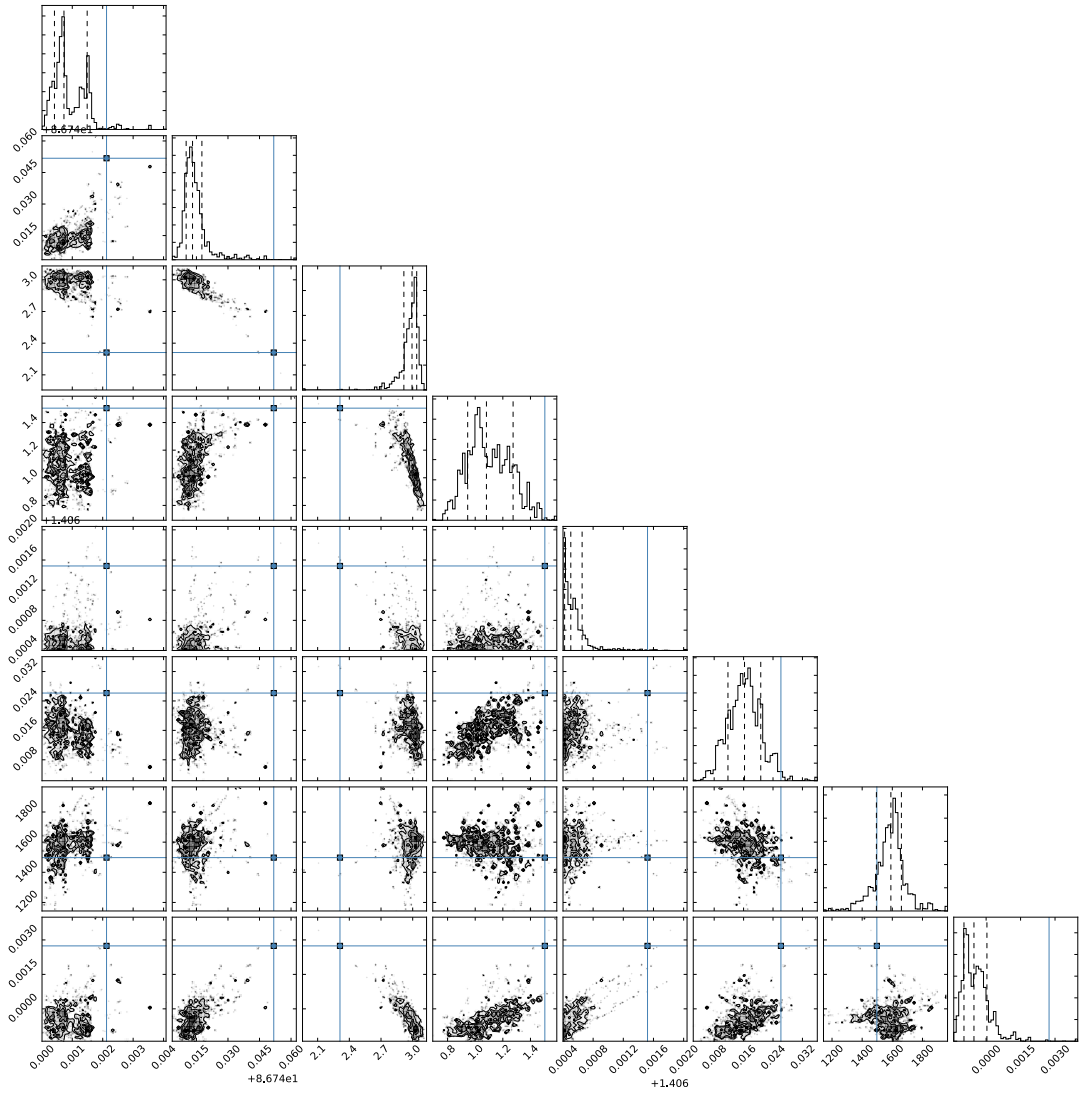

Figure 4.2: This "triangle" plot shows the movement of the walkers through parameter space during the course of the fitting procedure for the ReThElDo model applied to Kepler-5 b. For some parameters, the walkers settle around the best fit value in a Gaussian manner, while for others they run up against boundaries. The parameters displayed here are, from top to bottom, (1) e, (2) i, (3) ω, (4) M_p, (5) R_p, (6) A_g, (7) T_{day}, (8) Flux offset. The middle dotted line shows the median value and the surrounding dotted lines represent 1σ errors. Ideally, the correct value will correspond to this median value. The overall shape of the walker movement shows the probability distribution of each parameter. Some parameters have nearly Gaussian probability distributions, while the walkers of others encounter the boundaries for their parameters, gathering at these extreme values. The Gaussian distribution is typically favorable to the gathering of walkers at value boundaries.

As shown in Table 4.2, other than planetary mass and temperature, the ThElDo model produces essentially the same values for all parameters as the ReThElDo model. The mass value still falls within the ranges found in Esteves et al. (2013) and Esteves et al. (2015). However, the temperature is still less than the value calculated in these works, which is problematic, as it should in this case be higher to compensate for the lack of albedo. Albedo and temperature contribute to flux received from all planets, but must be of sufficient magnitude to be detected by the *Kepler* photometer if they are to be measured. A model that uses contributions from both parameters to fit data is more physically favorable than one that simply ignores one of the two relevant effects. Our model is clearly having trouble accurately fitting the thermal and reflective contributions to the phase curves, Esteves et al. (2013); Esteves et al. (2015) achieve a statistically significant fit with higher values for both temperature and albedo. This is likely due to the aforementioned secondary eclipse issues, as temperature and albedo flux constitute the secondary eclipse depth. Our model seems to fit the gravitational phase curves well because our mass values for both the ReThElDo and ThElDo models are within the relatively wide range of literature values (Esteves et al. 2013; Esteves et al. 2015) The phase curves shown in Figure 4.1 clearly resemble the multi-peaked gravitational phase curves more so than the centered single peak thermal and reflective curves.

Figures 4.2 and 4.3, which show walker movements for both the ReThElDo and ThElDo models, respectively, illustrate a suboptimal fitting process, which is probably the result of an issue in the secondary eclipse modeling, not the MCMC. Because the model is unable to fit the points of secondary eclipse ingress and egress, it will likely generate incorrect values for parameters that the secondary eclipse is heavily dependent upon, such as temperature and albedo, which define

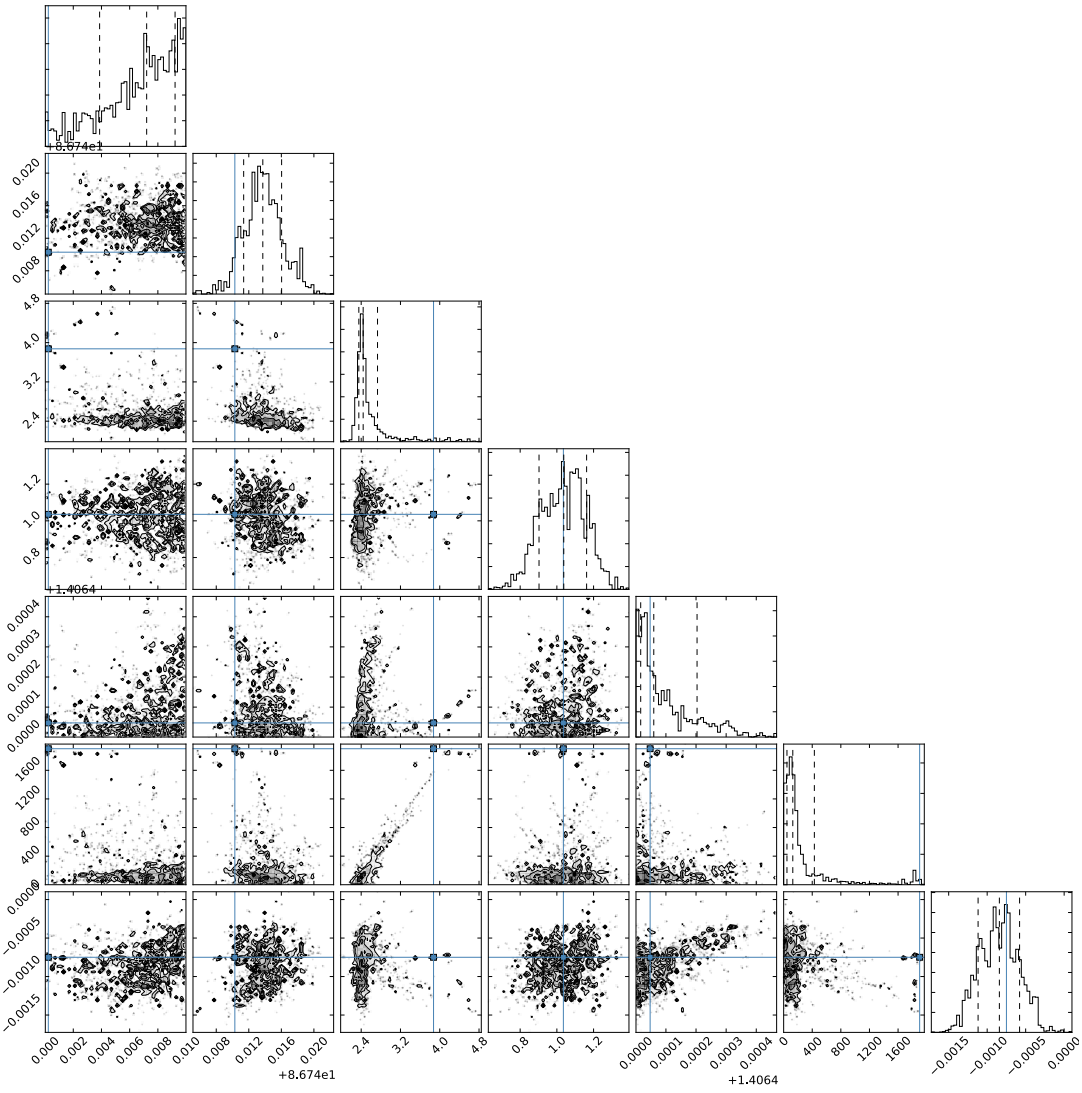

Figure 4.3: This "triangle" plot shows the movement of the walkers through parameter space during the course of the fitting procedure for the ThElDo model applied to Kepler-5 b. More walkers settle at parameter extremes during the run compared to the ReThElDo run shown in Figure 4.2. The parameters displayed here are, from top to bottom, (1) e, (2) i, (3) ω, (4) M_p, (5) R_p, (6) T_{day}, (7) Flux offset.

Table 4.3: Kepler-5 b: ThElDo Model $\chi^2 = 33.13$. 20 walkers 500 steps

Parameter	Best Fit	Median	Accepted Value	Reference
e	0.00	$0.007^{+0.002}_{-0.004}$	0^a	Esteves et al. (2015)
i [deg]	86.75	$86.753^{+0.003}_{-0.002}$	86.3 ± 0.5	Kipping & Bakos (2011)
ω [rad]	3.87	$2.44^{+0.05}_{-0.09}$	...	Esteves et al. (2015)
M_p [M_J]	1.04	$1.04^{+0.12}_{-0.14}$	$0.92^{+0.93}_{-1.02}$	Esteves et al. (2015)
R_p [R_J]	1.407	$1.4065^{+0.0001}_{-0.0001}$	$1.431^{+0.041}_{-0.052}$	Esteves et al. (2015)
T_{day} [K]	1901	128^{+301}_{-82}	2390^{+80}_{-100}	Esteves et al. (2015)

the magnitude of its depth. Alternatively, since Kepler-5 b has a very weak secondary eclipse signal, the model may simply struggle to fit phase curves of such low magnitudes. Finally, the underlying issue may be neither of these problems, in which case there must be an error in our thermal and reflective phase curve modeling and secondary eclipse depth calculation. Other parameters are well constrained by the transit, such as radius, inclination, and eccentricity, while others, such as mass, appear to be well constrained by the gravitational phase curves, which do not affect the depth of the secondary eclipse in our model.

In Figure 4.4, the residuals for our fit to the Kepler-5 b lightcurve show that it is most descrepant at transit ingress (near $\phi = 1$). However, this too may simply be an artifact of the secondary eclipse modeling issue, as the error values in the secondary eclipse phase section are orders of magnitude smaller than those in the transit section due more frequent data point binning during the transit, which makes the secondary eclipse data points much more influential in determining the final χ^2 value. If the model is initially unable to achieve a good secondary eclipse fit, it will then begin slightly adjusting the transit. This seems rather unlikely for this system, however, as the secondary eclipse is too weak a signal to even have distinct ingress and egress points. This is perhaps indicative of a greater underlying issue in our thermal and reflective phase curve and secondary eclipse

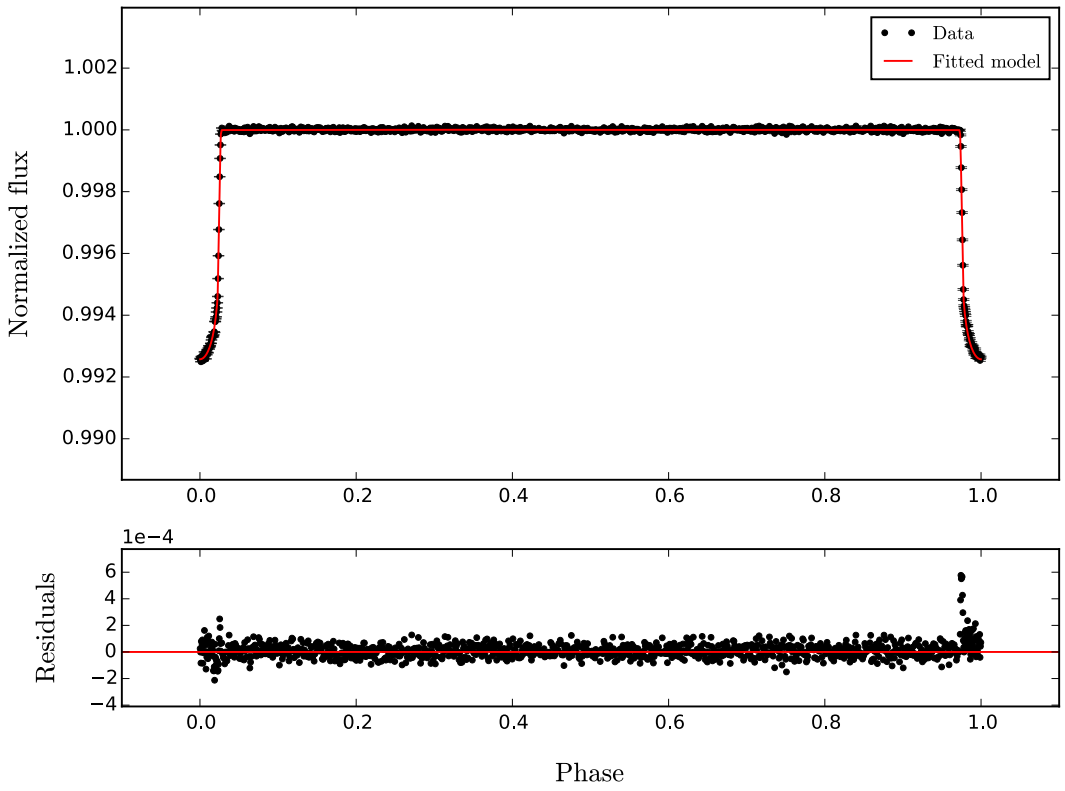

Figure 4.4: (top) Illustrates the full phase for Kepler-5 b. (bottom) Shows the residuals after subtracting the best fit model from the data. In this instance, the worst fit by the model is during ingress near $\phi = 1$ during ingress and egress of the primary transit.

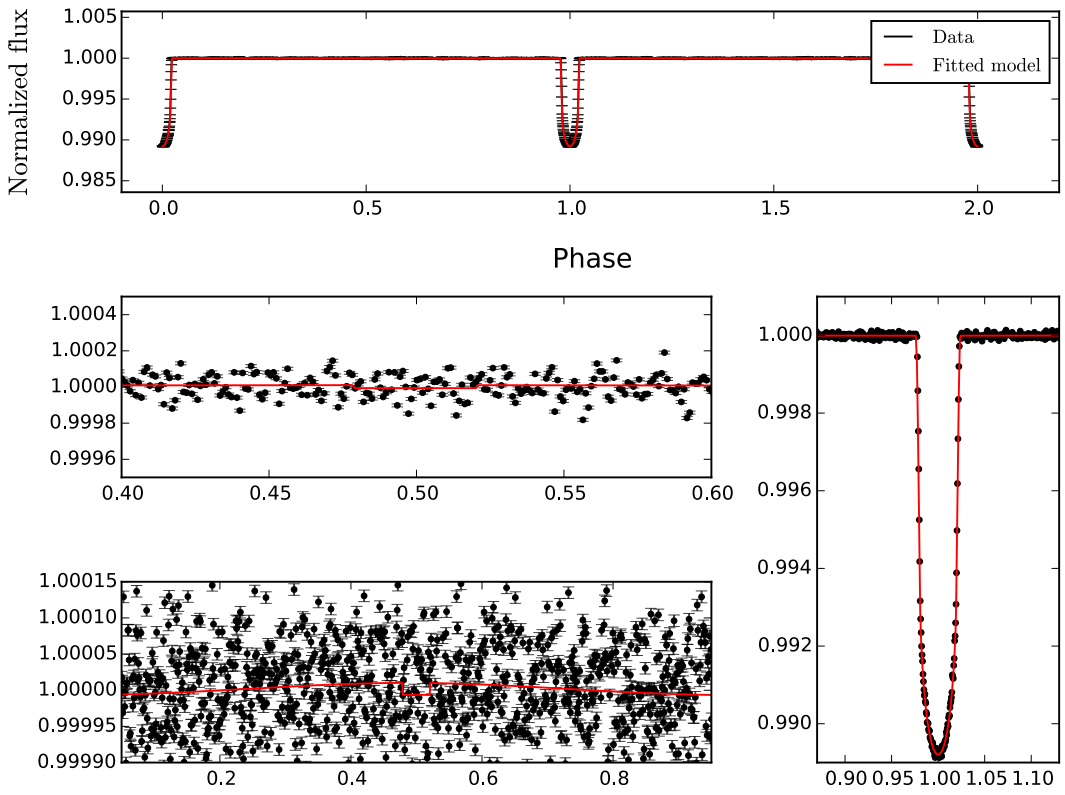

Figure 4.5: Illustrates the data and ReThElDo model lightcurve for Kepler-6 b. (above) Two phases of the planet's orbit. (middle left) The secondary eclipse section of the phase. (bottom left) The entire phase at a scale in which the phase effects are visible. (bottom right) Transit fit.

modeling. Once the secondary eclipse ingress and egress issue is resolved, we will know which of these issues is skewing our fitting procedure to produce unrealistic output parameters.

4.1.3 Kepler-6 b

Many of the results from the Kepler-6 b model fitting procedure agree with literature values. However, some do not. Our eccentricity is nonzero, therefore it cannot agree completely with the Esteves et al. (2015) model, which assumes a circular orbit. Our inclination disagrees with Esteves et al. (2013); Esteves et al.

Table 4.4: Kepler-6 b: Fixed Parameters.

Parameter	Value	Reference
R_* $[R_\odot]$	1.391	Dunham et al. (2010)
M_* $[M_\odot]$	1.209	Dunham et al. (2010)
T_* $[K]$	5647	Dunham et al. (2010)
a,b	0.480,0.138	Müller et al. (2013)
g	0.3979	Dunham et al. (2010)
$P[days]$	3.23472	Dunham et al. (2010)

Table 4.5: Kepler-6 b: ReThElDo Model $\chi^2 = 64.01$. 50 walkers 1000 steps

Parameter	Best Fit	Median	Accepted Value	Reference
e	0.010	$0.00999^{+0.00001}_{-0.00002}$	0^a	Esteves et al. (2015)
i [deg]	87.22	$87.221^{+0.001}_{-0.003}$	86.8 ± 0.3	Kipping & Bakos (2011)
ω [rad]	1.60	$1.61^{+.02}_{-.01}$	...	Esteves et al. (2015)
M_p [M_J]	0.43	$0.43^{+0.07}_{-0.08}$	$0.617^{+0.52}_{-0.051}$	Kipping & Bakos (2011)
R_p [R_J]	1.28	$1.2843^{+0.0001}_{-0.0001}$	$1.208^{+0.129}_{-0.049}$	Kipping & Bakos (2011)
A_g	0.091	$0.091^{+0.004}_{-0.004}$	$0.070^{+0.031}_{-0.034}$	Esteves et al. (2015)
T_{day} [K]	326	592^{+682}_{-387}	2060^{+90}_{-140}	Esteves et al. (2015)

(2015), but agrees with that of Kipping & Bakos (2011). Our radius value agrees with Esteves et al. (2013); Esteves et al. (2015); Kipping & Bakos (2011), but our mass value does not agree. Esteves et al. (2015) choose to fix the mass value, so perhaps they encountered a similar issue. Our geometric albedo value agrees with that of Esteves et al. (2015), but our dayside temperature is thousands of Kelvin below their calculated value. Our model fitting procedure is able to constrain parameter values heavily associated with the transit, as was discovered in our analysis of Kepler-5 b. However, the values most heavily associated with the secondary eclipse–dayside temperature and geometric albedo–are inaccurate due to the secondary eclipse modeling error. Once our model includes secondary eclipse ingress and egress, we may be able to constrain these parameter values to closer agreement with the literature. However, if our program still struggles to

find proper fits, there is a deeper underlying issue with our thermal and reflective phase effect calculations, or perhaps with our calculation of secondary eclipse depth.

The triangle plot illustrating the Kepler-6 b fitting process, shown in Figure 4.6, shows that some terms, such as inclination, mass, radius, and geometric albedo, are fit by Gaussian distributions of walkers surrounding the selected best fit value. In contrast, for the eccentricity, argument of periastron, and temperature parameters, the walkers are unable to settle around a parameter value and instead collect at the upper or lower boundaries of their possible values. Relative to the fitting procedure of Kepler-5 b, this fitting procedure has been very successful, which is likely a result of the greater number of walkers and steps. It is particularly interesting that the geometric albedo fitting is so strongly Gaussian while the temperature fit is poorly constrained, as both parameters are innately coupled in both the phase curve and secondary eclipse modeling process.

Our model does an acceptable job fitting certain parameters of Kepler-6 b heavily associated with transit characteristics. However, as is apparent in Figure 4.7, the transit fit is far from perfect. Upon removal of the secondary eclipse error, the fitting procedure will no longer be forced to attempt to compensate for the model's insufficiencies at modeling secondary eclipse ingress and egress. This may allow us to calculate all parameter values within the realm of reasonable possibilities, perhaps even improving on the fits of Esteves et al. (2015) by including eccentricity as a free parameter. Kipping & Bakos (2011) calculate one possible eccentric orbit of Kepler-6 b, so allowing flexibility in this parameter will make for a more robust model. If the secondary eclipse ingress and egress does not end up being the underlying issue, then we will explore ways in which our thermal and reflective phase curve and secondary eclipse depth calculations may be off. We

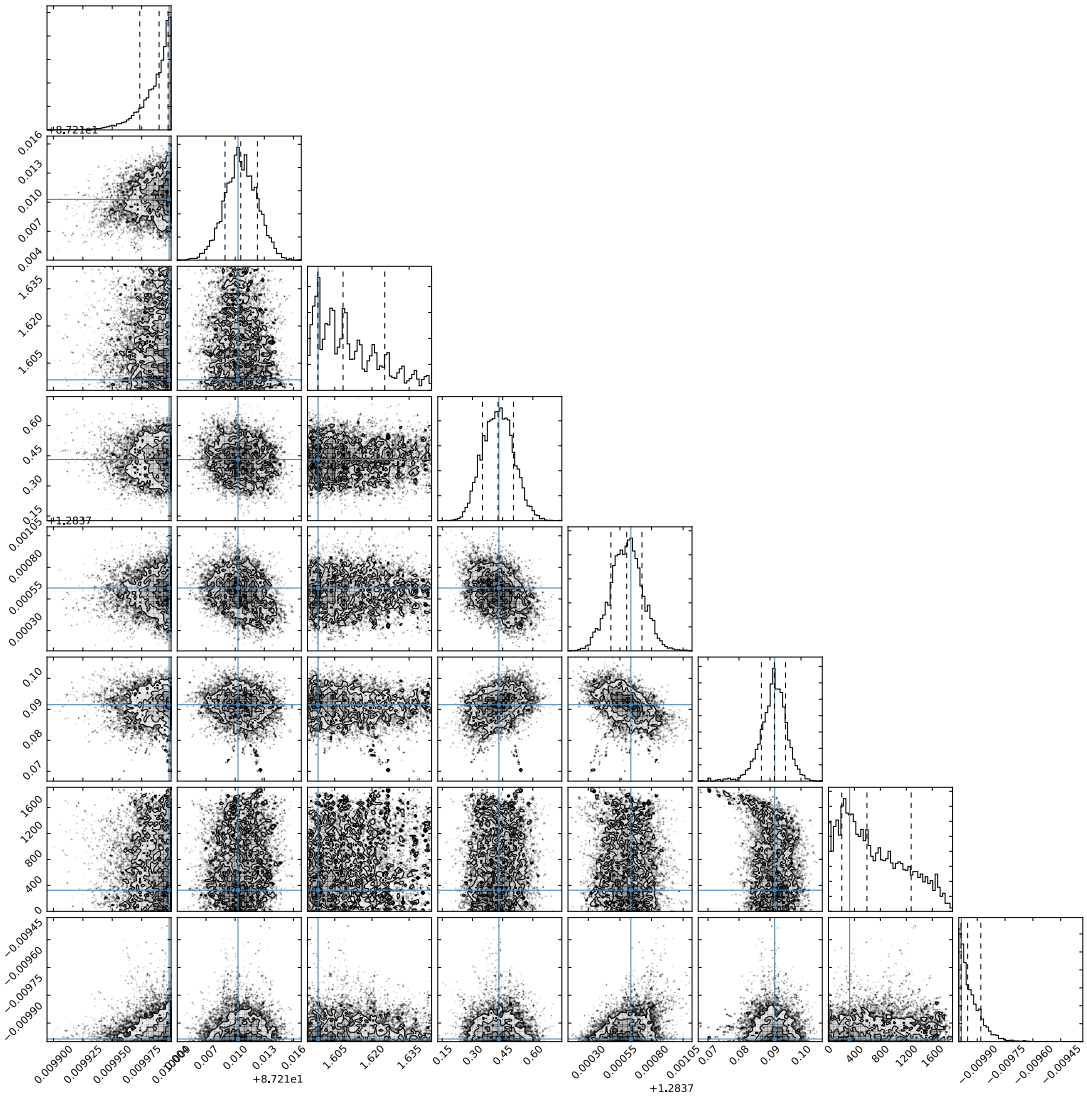

Figure 4.6: This triangle plot shows the movement of the walkers through parameter space during the course of the fitting procedure for the ReThElDo model applied to Kepler-6 b. For some parameters, the walkers settle around the best fit value in a Gaussian manner, while for others they run up against boundaries. The parameters displayed here are, from top to bottom, (1) e, (2) i, (3) ω, (4) M_p, (5) R_p, (6) A_g, (7) T_{day}, (8) Flux offset.

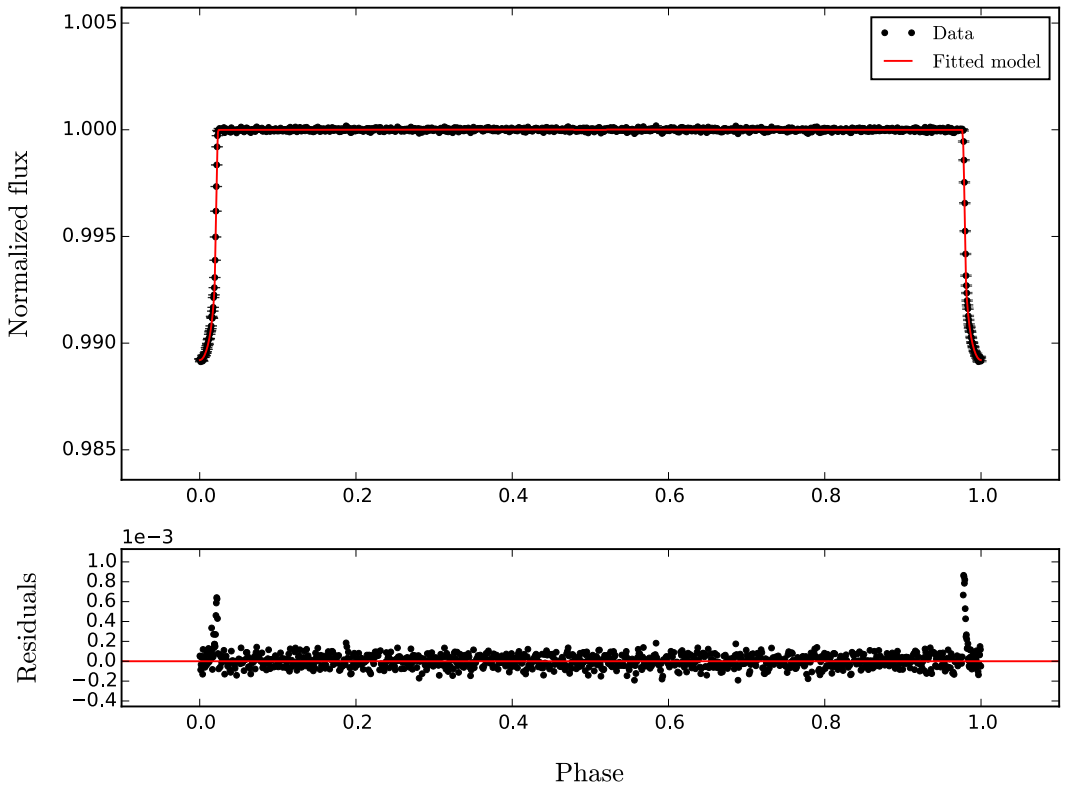

Figure 4.7: (top) Illustrates the full phase for Kepler-6 b. (bottom) Shows the residuals after subtracting the best fit model from the data. In this instance, the worst fit by the model is during both ingress and egress, which may indicate a poor eccentricity value.

shall now move to targets with higher magnitude secondary eclipses and phase variations to fully test our model's abilities.

4.1.4 Kepler-7 b

Table 4.6: Kepler-7 b: Fixed Parameters.

Parameter	Value	Reference
R_* $[R_\odot]$	1.843	Latham et al. (2010)
M_* $[M_\odot]$	1.347	Latham et al. (2010)
T_* $[K]$	5933	Latham et al. (2010)
a,b	0.374,0.185	Müller et al. (2013)
g	0.3442	Latham et al. (2010)
$P[days]$	4.88553	Latham et al. (2010)

Table 4.7: Kepler-7 b: ReThElDo Model $\chi^2 = 17.14$. 30 walkers 1000 steps

Parameter	Best Fit	Median	Accepted Value	Reference
e	0.010	$0.00996^{+0.00003}_{-0.00005}$	0^a	Esteves et al. (2015)
i [deg]	86.54	$86.541^{+0.002}_{-0.003}$	$86.5^{+2.0}_{-1.4}$	Kipping & Bakos (2011)
ω [rad]	5.05	$5.06^{+.01}_{-.01}$	...	Esteves et al. (2015)
M_p [M_J]	0.53	$0.60^{+0.14}_{-0.14}$	0.441^a	Esteves et al. (2015)
R_p [R_J]	1.44	$1.4418^{+0.0004}_{-0.0018}$	$1.45^{+0.18}_{-0.15}$	Kipping & Bakos (2011)
A_g	0.022	$0.032^{+0.026}_{-0.023}$	$0.248^{+0.073}_{-0.071}$	Esteves et al. (2015)
T_{day} [K]	2315	2297^{+33}_{-54}	2510^{+90}_{-110}	Esteves et al. (2015)

The run on Kepler-7 b further demonstrates the established strengths and weaknesses of our model. Unlike Kepler-5 b and Kepler-6 b, Kepler-7 b has a clear secondary eclipse. As shown in Table 4.4, our calculated mass is in agreement with literature values (Latham et al. 2010; Esteves et al. 2015; Demory et al. 2011), but our albedo and temperature parameters do not agree, as is usually the case. Interestingly, while our radius and inclination parameters are not in agreement with those of Esteves et al. (2015) and Demory et al. (2011), they do agree to

the values found by Kipping & Bakos (2011); Latham et al. (2010). This is likely because Esteves et al. (2015) and Demory et al. (2011) calculate a slightly smaller inclination value than this work, Kipping & Bakos (2011), and Latham et al. (2010) do. The movement of walkers through parameter space during the fitting process, shown in Figure 4.9, shows an interesting bimodality in fitting for radius, which may be hinting at the second possible radius-inclination combination found in Esteves et al. (2015) and Demory et al. (2011). Aside from the eccentricity running up against its upper limit and albedo against its lower limit, the remaining distributions on the triangle plots are mostly Gaussian, indicating that the fitting procedure was successful.

While Esteves et al. (2015) assume a circular orbit for Kepler-7 b, we calculate a nonzero eccentricity value. Other studies that have analyzed this system without assuming its orbit to be circular have found nonzero eccentricity values (Demory et al. 2011; Kipping & Bakos 2011). Our value of $e = 0.01$ is closer to that of Demory et al. (2011) than to the significantly larger value calculated by Kipping & Bakos (2011). We conclude that our model does a commendable job finding parameter values for eccentricity, inclination, radius, and mass. However, it still fails to produce dayside temperature and geometric albedo values that agree with boundaries from the literature. More disturbingly, perhaps, the values for dayside temperature and albedo are both depressed relative to the literature values. If the issue were simply degeneracy between these two parameters, one would be inflated while the other is depressed. Because both parameters are of insufficient magnitude, there is a greater underlying issue generating this problem. Some residuals can be seen during egress of the transit in Figure 4.10. This is likely because Kepler-7 b produces the deepest secondary eclipse aside from that of HAT-P-7 b, which means the ingress and egress data points that are not properly

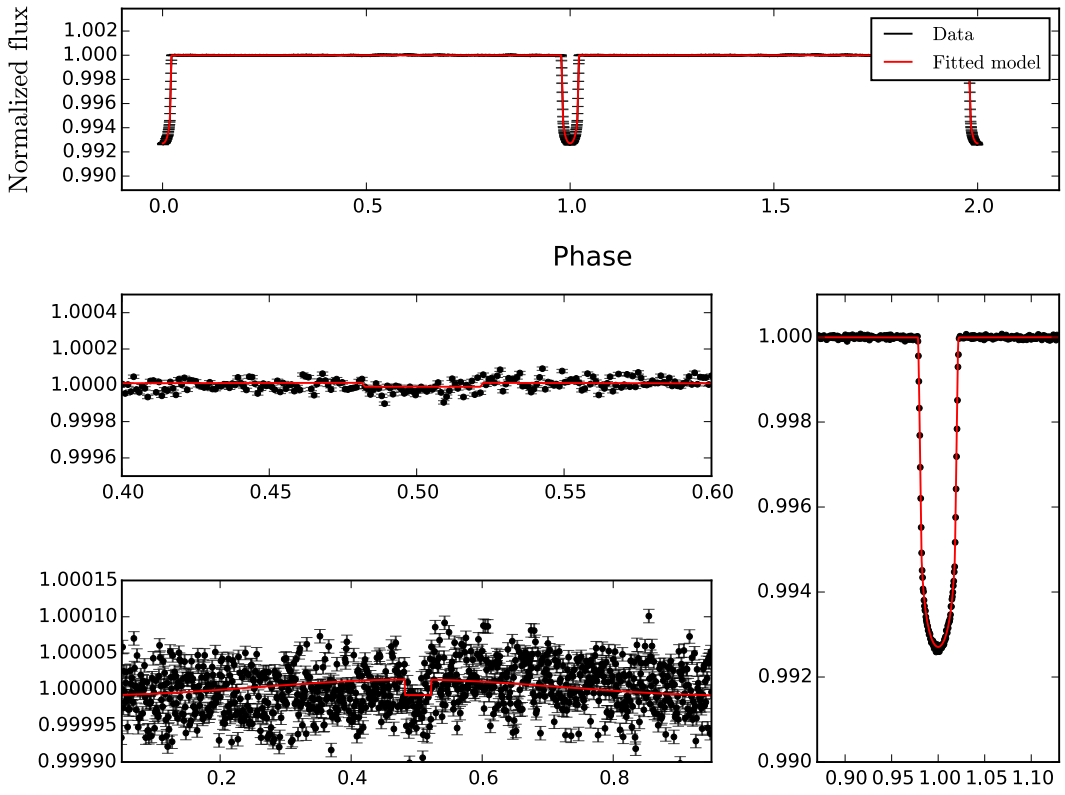

Figure 4.8: Illustrates the data and ReThElDo model lightcurve for Kepler-7 b. (above) Two phases of the planet's orbit. (middle left) The secondary eclipse section of the phase. (bottom left) The entire phase at a scale in which the phase effects are visible. (bottom right) Transit fit.

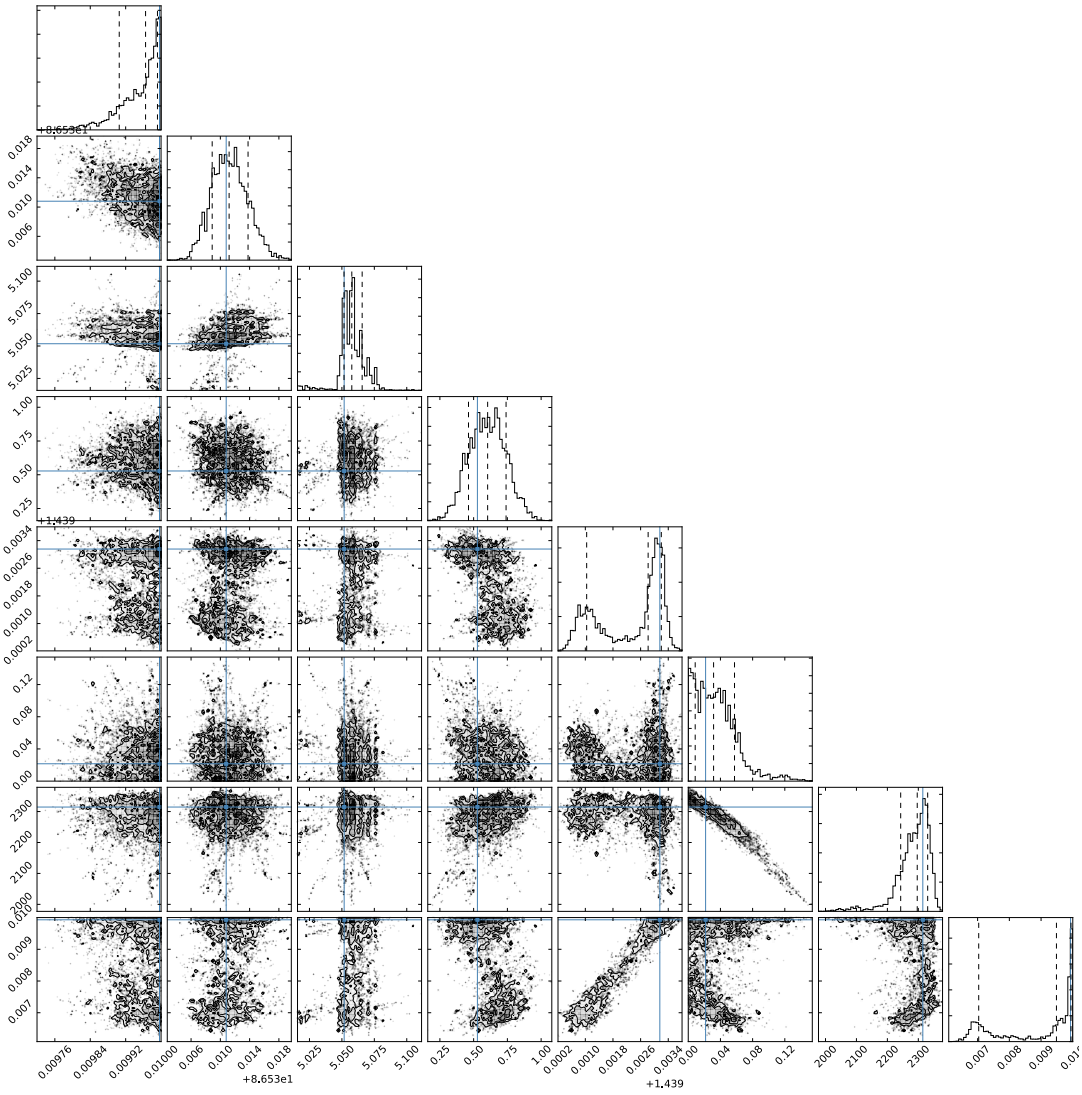

Figure 4.9: This triangle plot shows the movement of the walkers through parameter space during the course of the fitting procedure for the ReThElDo model applied to Kepler-7 b. For some parameters, the walkers settle around the best fit value in a Gaussian manner, while for others they run up against boundaries. The parameters displayed here are, from top to bottom, (1) e, (2) i, (3) ω, (4) M_p, (5) R_p, (6) A_g, (7) T_{day}, (8) Flux offset.

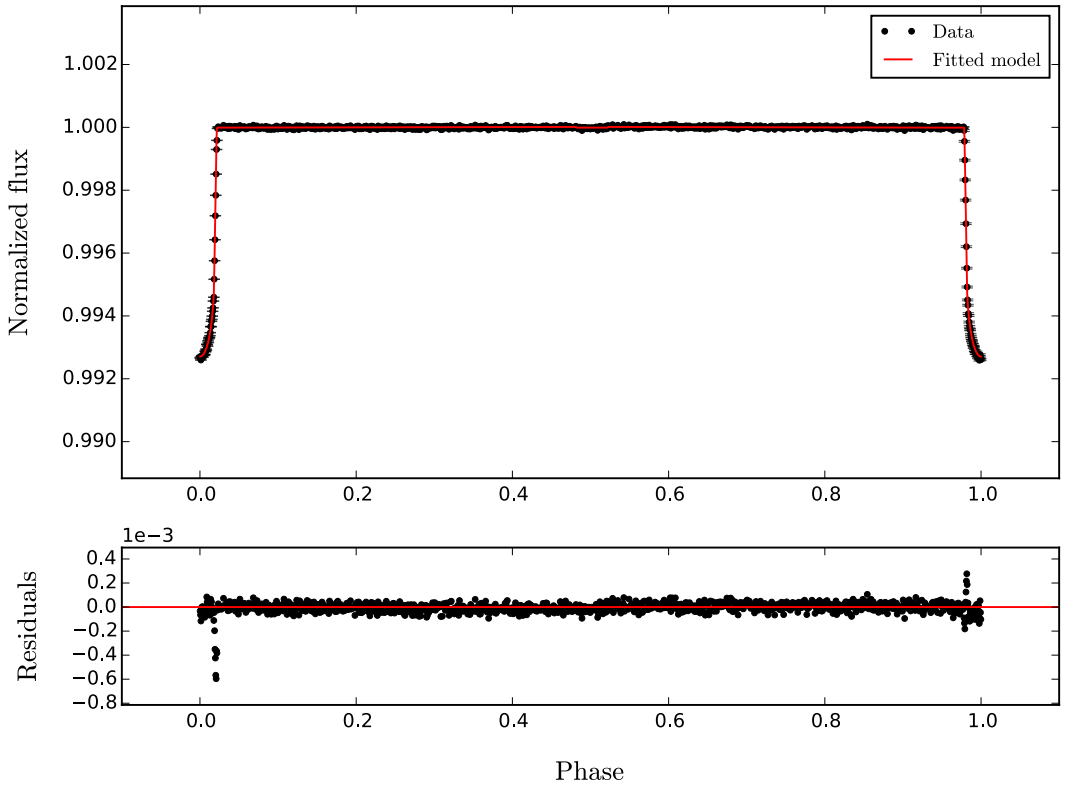

Figure 4.10: (top) Illustrates the full phase for Kepler-7 b. (bottom) Shows the residuals after subtracting the best fit model from the data. In this instance, the worst fit by the model is during egress after $\phi = 0$.

modeled are further offset from the model than in Kepler-5 b and Kepler-6 b, forcing the model to skew the transit fit more in order to compensate for the secondary eclipse modeling error.

As mentioned previously, the secondary eclipse depth is inherently tied to the magnitude of dayside temperature and geometric albedo. Because our secondary eclipse model does not fit ingress and egress of the eclipse, the values of these parameters will be skewed by the fitting algorithm attempting to find a better fit to these data points. Upon resolution of this issue, our code should be able to successfully fit the dayside temperature and geometric albedo parameters to literature values. If it cannot, there is a greater underlying issue in our thermal

and reflective phase curve and secondary eclipse depth calculations. Once the ultimate underlying issue is resolved, we will be able to properly fit these final two parameter values. Furthermore, we shall be able to do so without assuming a circular orbit, which is a common simplification (Esteves et al. 2013; Esteves et al. 2015; Shporer & Hu 2015). Other models that have included eccentricity as a free parameter have found better fits with nonzero eccentricity orbits (Placek et al. 2014). Furthermore, nonzero eccentricities help disentangle to degeneracy between the temperature and albedo parameters, as their peaks shift in different directions Placek et al. (2014). However, this only begins to work for $e > 0.3$ Placek et al. (2014). While our calculated nonzero eccentricity for this target is not sufficiently high to argue for it as a thermal and reflective degeneracy breaking mechanism, it is still a more physically correct than assuming an eccentricity of zero. We will continue to fit our models with eccentricity as a free parameter. One of its primary constraints is the timing of secondary eclipse and transit centers. With resolution of secondary eclipse modeling issue, our constraint of this free parameter will likely become even more accurate, which will allow us to calculate a more physically accurate orbit. The greater accuracy of this orbit will then propagate through the model, permitting more accurate calculations for our other parameters.

4.1.5 HAT-P-7 b

The runs on HAT-P-7 b are the most explicitly demonstrative of the secondary eclipse modeling issue. The intensely apparent multimodality of the triangle plot in Figure 4.12, with 20 walkers and 300 steps, becomes even more heavily exaggerated in Figure 4.13, which has 20 walkers and 2000 steps.The χ^2 value is improved

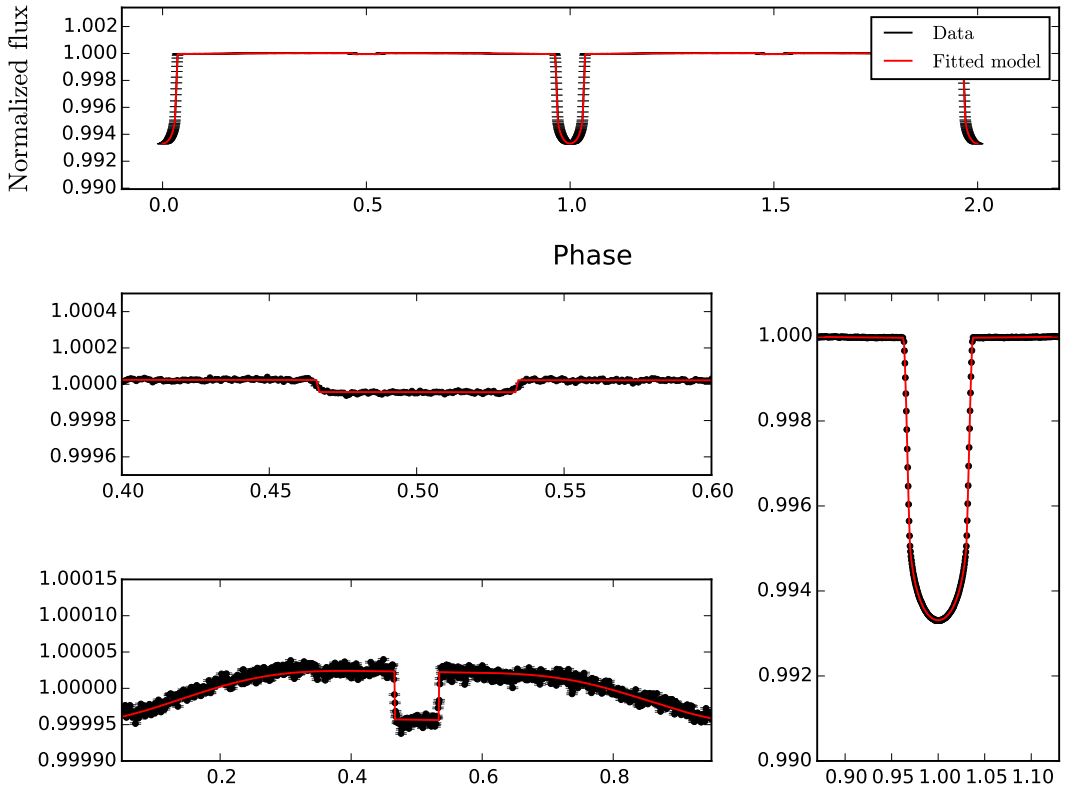

Figure 4.11: Illustrates the data and ReThElDo model lightcurve for HAT-P-7 b. (above) Two phases of the planet's orbit. (middle left) The secondary eclipse section of the phase, which shows a significant decrease in flux compared to other targets. (bottom left) The entire phase at a scale in which the phase effects are visible. (bottom right) Transit fit.

Table 4.8: HAT-P-7 b: Fixed Parameters. R_* is the stellar radius, M_* is the stellar mass, T_* is the stellar temperature, a and b are the quadratic limb darkening coefficients, g is the gravity darkening coefficient, and P is the period.

Parameter	Value	Reference
R_* $[R_\odot]$	1.98	Butler et al. (2006)
M_* $[M_\odot]$	1.52	Lund et al. (2014)
T_* $[K]$	6350	Pál et al. (2008)
a,b	0.344,0.1843	Müller et al. (2013)
g	0.2820	Pál et al. (2008)
$P[days]$	2.204735	Pál et al. (2008)

Table 4.9: HAT-P-7 b: ReThElDo Model $\chi^2 = 28.26$. 20 walkers 300 steps

Parameter	Best Fit	Median	Accepted Value	Reference
e	0.000	$0.0002^{+0.0002}_{-0.0001}$	0^a	Esteves et al. (2015)
i [deg]	82.99	$82.996^{+0.006}_{-0.002}$	$83.143^{+0.023}_{-0.020}$	Esteves et al. (2015)
ω [rad]	2.01	$2.01^{+.01}_{-.00}$	...	Esteves et al. (2015)
M_p [M_J]	1.57	$1.58^{+0.01}_{-0.01}$	1.63 ± 0.13	Esteves et al. (2015)
R_p [R_J]	1.483	$1.4831^{+0.0001}_{-0.0002}$	$1.419^{+0.178}_{-0.085}$	Esteves et al. (2015)
A_g	0.207	$0.2068^{+0.0006}_{-0.0007}$	$0.2044^{+0.0058}_{-0.0067}$	Esteves et al. (2015)
T_{day} [K]	829	829^{+1}_{-2}	2860 ± 30	Esteves et al. (2015)

Table 4.10: HAT-P-7 b: ReThElDo Model $\chi^2 = 27.32$. 20 walkers 2000 steps

Parameter	Best Fit	Median	Accepted Value	Reference
e	0.003	$0.0039^{+0.0002}_{-0.0012}$	0^a	Esteves et al. (2015)
i [deg]	83.07	$83.105^{+0.005}_{-0.041}$	$83.143^{+0.023}_{-0.020}$	Esteves et al. (2015)
ω [rad]	1.69	$1.6905^{+0.0032}_{-0.0003}$	...	Esteves et al. (2015)
M_p [M_J]	1.57	$1.577^{+0.006}_{-0.002}$	1.63 ± 0.13	Esteves et al. (2015)
R_p [R_J]	1.483	$1.4831^{+0.0003}_{-0.0003}$	$1.419^{+0.178}_{-0.085}$	Esteves et al. (2015)
A_g	0.11	$0.113^{+0.003}_{-0.002}$	$0.2044^{+0.0058}_{-0.0067}$	Esteves et al. (2015)
T_{day} [K]	2561	2557^{+5}_{-7}	2860 ± 30	Esteves et al. (2015)

in the model with more steps, as is expected during a fitting process. However, the non-Gaussian, multimodal triangle plots do not indicate that the fitting procedure robustly explored the entire parameter space. Usually, the MCMC's walkers will collect around the best fit values in some Gaussian distribution. Here, however,

the walkers do not seem to have settled at a steady value for certain parameters. This is likely indicative of an error that is insurmountable for the fitting process, such as the secondary eclipse model not fitting the secondary eclipse ingress and egress points properly.

Our best fit parameters for the 300 step run, shown in Table 4.9, are distinct from parameters from the other three targets when compared to the literature (Esteves et al. 2013; Esteves et al. 2015; Placek et al. 2014), in that the albedo is in agreement while the radius is not. We use a larger stellar radius than do these three works, therefore it makes sense that our calculated radius is larger. However, our R_p/R_* value, which does not depend on knowledge of the stellar radius, is also different than literature values (Morris et al. 2013; Esteves et al. 2013; Esteves et al. 2015; Placek et al. 2014). Our inclination is in agreement with literature values, which is interesting, as we would expect it to change in order to account for the different planetary radius. The calculated albedo is in agreement with Esteves et al. (2015), but our dayside temperature is still much too cool. The dayside temperature from the 2000 walker run is in closer agreement with literature values than that of the other planets. The thermal and reflective phase effects are certainly higher for this target than for the others, as revealed by the deeper secondary eclipse and more pronounced phase effects, which is likely why the program has an easier time finding reasonable values for their influential parameters. However, this deeper secondary eclipse depth also worsens the error caused by the secondary eclipse modeling issue, which prevents the walkers from settling to the true best fit. Instead, they contort the transit in attempt to fit the secondary eclipse ingress and egress data points.

When viewing the triangle plots in Figures 4.12 and 4.13 from the two different HAT-P-7 b runs of different lengths, it is clear that multimodality propagates itself

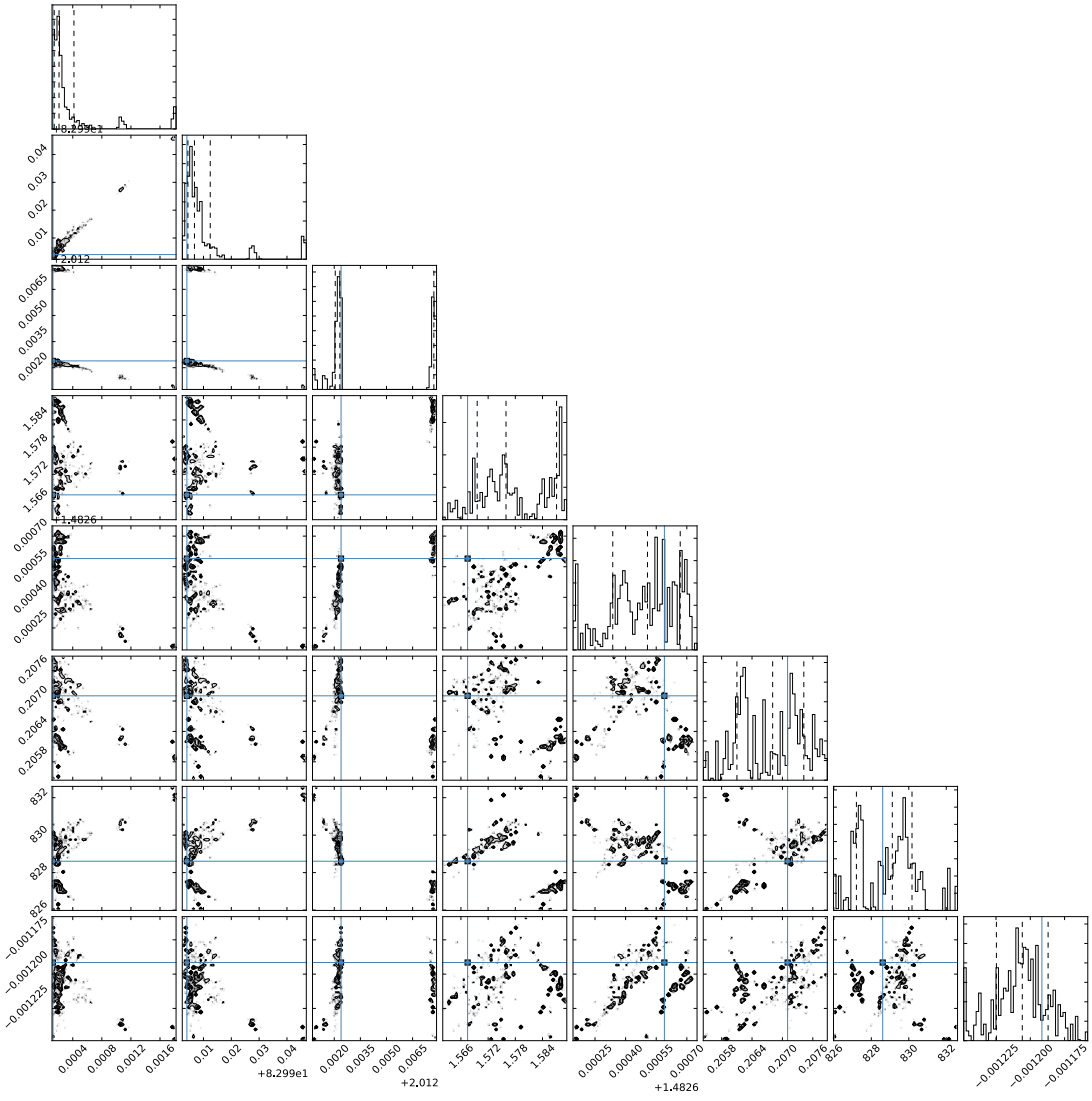

Figure 4.12: This triangle plot shows the movement of the walkers through parameter space during the course of the 300 step fitting procedure for the ReThElDo model applied to HAT-P-7 b. More walkers settle at parameter extremes during the run compared to the ReThElDo run shown in Figure 4.2. The parameters displayed here are, from top to bottom, (1) e, (2) i, (3) ω, (4) M_p, (5) R_p, (6) A_g, (7) T_{day}, (8) Flux offset.

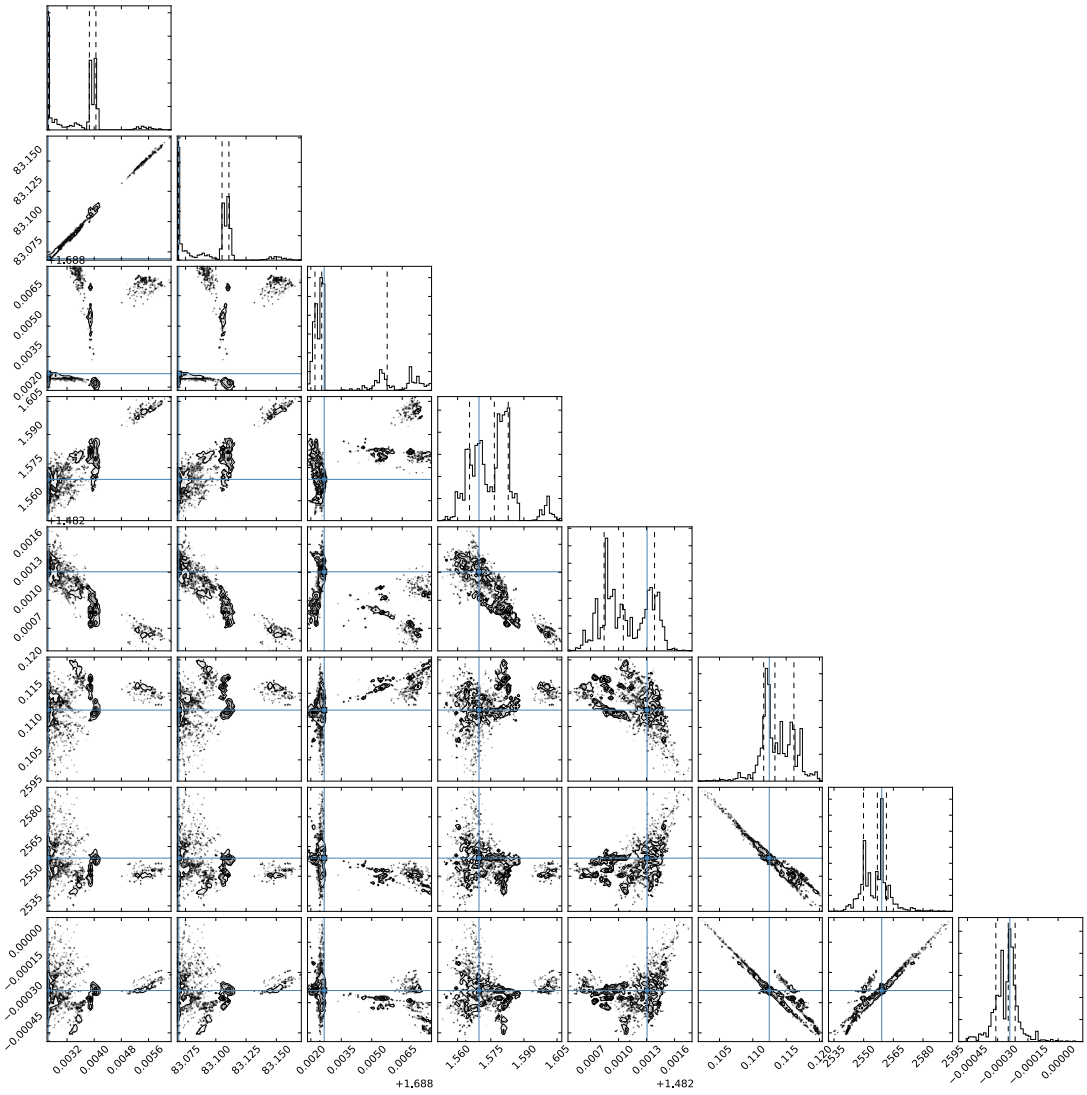

Figure 4.13: This triangle plot shows the movement of the walkers through parameter space during the course of the 2000 step fitting procedure for the ReThElDo model applied to HAT-P-7 b. More walkers settle at parameter extremes during the run compared to the ReThElDo run shown in Figure 4.2. The parameters displayed here are, from top to bottom, (1) e, (2) i, (3) ω, (4) M_p, (5) R_p, (6) A_g, (7) T_{day}, (8) Flux offset.

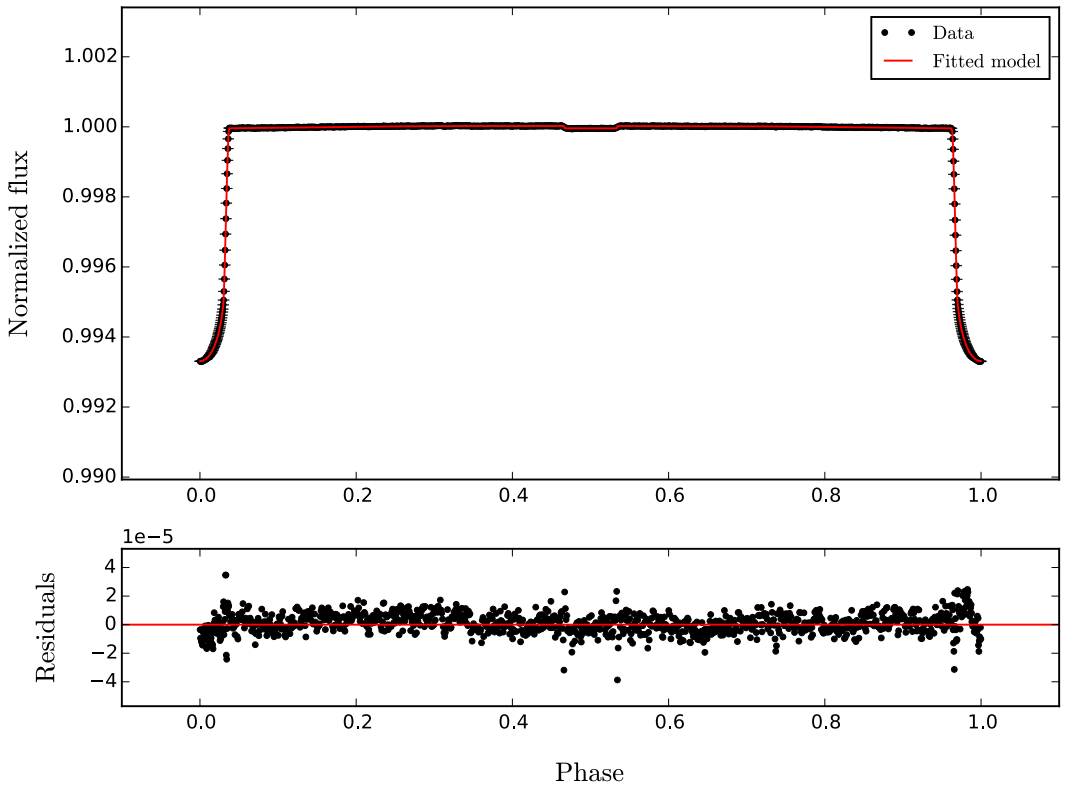

Figure 4.14: From the 300 step fitting run on the HAT-P-7 b model. (top) Illustrates the full phase for HAT-P-7 b. (bottom) Shows the residuals after subtracting the best fit model from the data. In this instance, the worst part of the fit in terms of contribution to overall χ^2 value are the six data points before and after $\phi = 0.5$, which are the ingress and egress of the secondary eclipse. Because HAT-P-7 b has the most prominent secondary eclipse, the secondary eclipse modeling issue has a greater magnitude of negative effect on our fitting procedure.

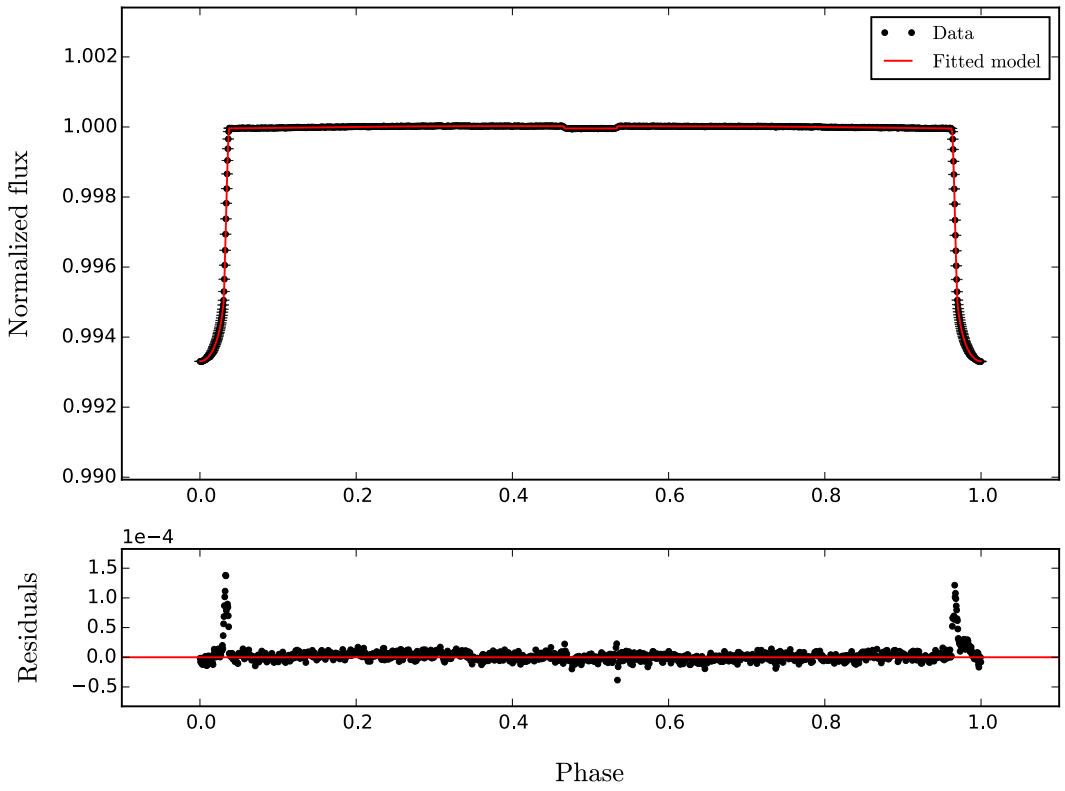

Figure 4.15: From the 2000 step fitting run on the HAT-P-7 b model. (top) Illustrates the full phase for HAT-P-7 b. (bottom) Shows the residuals after subtracting the best fit model from the data. For this longer run, the fitting formalism attempts to reduce the residuals shown before and after $\phi = 0.5$ in Figure 4.14, which in turn skews the transit, as is shown here in the residuals duing ingress and egress.

continuously, causing walkers not to settle in Gaussian distributions around the correct parameter values. More importantly, in comparing the residuals in Figure 4.14 and 4.15, it is clear that the program first goes to a fit that agrees well with the transit, as the run with 300 steps has almost no residuals near the transit section of the phase. However, the data points of secondary eclipse ingress and egress are poorly fit. After 2000 steps, the walkers have attempted to settle the discrepancy of these data points, which have smaller errors and therefore contribute more to the over χ^2 value, by contorting the transit fit, as is shown in Figure 4.15. One possibility is that the secondary eclipse ingress and egress error is very important for HAT-P-7 b and less important for targets with weaker secondary eclipses. Alternatively, one of our calculations for the thermal and reflective phase curves, or the secondary eclipse depth, may be incorrect. The clear next step is to resolve the obvious and pressing secondary eclipse ingress and egress issue. After this, if the fitting process still does not work, we will need to explore these other possibilities.

4.1.6 Discussion

While many of our parameter values are in agreement with the literature, there still exists a significant flaw in our model that causes the temperature and albedo calculations to deviate significantly from those in other studies (Esteves et al. 2013; Esteves et al. 2015; Placek et al. 2014; Batygin & Stevenson 2010). The inability of our model to calculate flux values for secondary eclipse ingress and egress prevents our fitting algorithm from reaching an actual best fit value. To combat this, we will need to develop a new secondary eclipse model. Rather than simply modeling a constant flux, which constitutes the bottom of the secondary

eclipse, for a duration equal to that of the transit and offset by $\phi = 0.5$ and adjusting the eclipse center slightly for eccentricity, we will need to use equations that describe the geometry of the planet moving behind the star.

The easiest solution is to calculate the duration of ingress and egress, remove those times from the current secondary eclipse duration, then fit a line between the out-of-eclipse flux and the bottom of the secondary eclipse. While fitting a line in this matter would be absolutely horrendous for transit modeling, it is completely acceptable for secondary eclipse modeling, as limb darkening has no effect on the slop of depression in the light curve. After we have corrected this relatively minor error in the model, our fitting algorithm will not be forced to attempt to compensate for the faults of the model. This will hopefully allow us to calculate parameters in agreement with those of other phase curve models. Furthermore, our model may make improvements to the fits in these works by allowing eccentricity to be a free parameter. As discussed previously, some of these systems already have predicted nonzero eccentricities, so this will potentially be a significant improvement to previous models.

Chapter 5

Conclusion

Kepler has irreversibly changed our perspective regarding the prevalence of planets in our galaxy. Not only has it found thousands of confirmed planets and even more unconfirmed candidates, it also contains data of sufficient quality to measure signals from two very subtle flux effects in transiting systems: secondary eclipses and phase curves. We have generated a data reduction program that reduces both transit, secondary eclipse, and phase curve data. It preserves these weakest of signals and produces very clean transits. Furthermore, we have developed a model that describes these three types of flux variation. The primary shortcoming of this model is likely in modeling the ingress and egress of secondary eclipse, which our program appears incapable of doing. This in turn confuses our parallel tempered affine invariant MCMC fitting routine, which then skews other portions of the model in order to achieve a better fit at secondary eclipse ingress and egress.

We have demonstrated the successes and shortcomings of our program through analysis of Kepler-5 b, Kepler-6 b, Kepler-7 b, and HAT-P-7 b. The residuals and triangle plots from these runs, especially those from HAT-P-7 b, provide some evidence that the underlying error is in this secondary eclipse ingress and egress modeling. Upon resolution of this minor error, we will hopefully 'constrain the dayside temperature and geometric albedo, which are currently the most prob-

lematic of the output parameters. Most of our other parameters, especially those correlated primarily with the transit, and even those that relate primarily to the gravitational phase effects, agree with literature values. This is a heartening sign that the final remaining issue is in the secondary eclipse ingress and egress, as the terms responsible for defining the magnitude of secondary eclipse are dayside temperature and geometric albedo.

Upon resolution of this final issue, the model can be applied to characterize the orbits, radii, masses, and atmospheric characteristics of dozens of *Kepler* exoplanets. It may even successfully characterize some targets that eluded proper fitting in the past, as our model is able to fit eccentric orbits while most currently assume a circular orbit. In addition to this greater detail, our model has the capacity to be improved in order to even more deeply characterize these targets. This improvement will come in the form of offsetting the thermal and reflected phase curves from one another, which is physically equivalent from shifting the hottest area of the planet away from the area receiving the most direct stellar radiation. This may allow us to measure wind speeds on hot-Jupiters, which have fascinating implications for other exoplanet characteristics that are difficult to probe, such as magnetic field. The more detail our model encapsulates, the smaller a physical effect we will be able to measure. This holds true in the addition of the secondary eclipse to transit models, followed by the addition of phase effects to these models. Offsetting these phase effects to probe even more subtle flux variations will allow us to take the next major step in improving the detailed nature of models to *Kepler* lightcurves.

5.1 Future Work

Exoplanetary Winds Close orbiting hot-Jupiters become tidally locked to their host stars on a relatively short time scale, which creates extreme temperature differences between their day and night sides. This temperature gradient drives planetary winds that redistribute dayside heat to the nightside, which in turn decreases the temperature contrast between the two sides. In close orbiting, tidally locked, non-eccentric systems, there is a significant degeneracy between thermal and reflective flux contributions to the combined phase curve flux. However, these dayside to nightside winds, which can travel at supersonic velocities, may induce a phase lag between the thermal and reflected flux contributions, as they will shift the hottest region of the planet to a different area than that of maximum reflection. This effect may provide a mechanism for breaking this parameter degeneracy while simultaneously providing a means of measuring wind velocities on hot-Jupiters as a function of planetary radius. We will add this effect to a preexisting phase curve model to test for improvement of fits to *Kepler* data.

K2 The second phase of the *Kepler* mission, *K2*, utilizes pressure from solar radiation to stabilize the space telescope though only two of its four reaction wheels remain functional. Because the telescope is in an Earth trailing orbit, it must change its field of view every 83 days, 75 of which are dedicated to science. Though data quality is inferior to that of the original *Kepler* mission, both in terms of noise and duration of time spent on a given field of view, this clever extension of the mission provides an opportunity to discover and characterize exoplanets around thousands of other stars. According to the NASA Exoplanet Archive, there are currently 270 exoplanet candidates in K2 data, 21 of which have

been confirmed, 6 of which were false positives (Montet et al. 2015). Though none of the confirmed exoplanets are in systems likely to have high magnitude phase effects, WASP-47 b and WASP-28 b (K2-1) may produce phase curves noticeable in K2 data. We will look for signs of secondary eclipses and phase curves in the short-cadence data from Vanderburg & Johnson (2014) and assess the feasibility of this study once K2 hot-Jupiter exoplanet candidates are confirmed.

Nontransiting Exoplanets Phase effects are present even in non-transiting systems. *Spitzer* has measured phase curves from the HD 179949b (Cowan et al. 2007) and *CoRoT* has measured those from HD 46375b (Gaulme et al. 2010), both of which are nontransiting. Exoplanets detected by their phase effects would likely be followed up by coronagraph studies, which means there is interest in discovering objects with periods greater than 100 days. This requires long lightcurves, such as those from *Kepler*. However, the long-term stability and photometric precision required for making these measurements is thought to be beyond the scope of *Kepler* (Kane & Gelino 2011). A significantly clever splining process would need to be developed to detrend data while still preserving the phase effects signal. Without the periodicity of a transit, it is difficult to estimate the periodicity of the phase effects from a nontransiting system. This is vital information for a detrending process conducive to preservation of phase effect signal. If phase effects from nontransiting systems cannot be detected in *Kepler* data, our model can be applied to data from Spitzer for studies similar to those of (Cowan et al. 2007) and (Gaulme et al. 2010). We will discuss the feasibility of implementing all three of these aforementioned extensions to modern phase curve analysis.

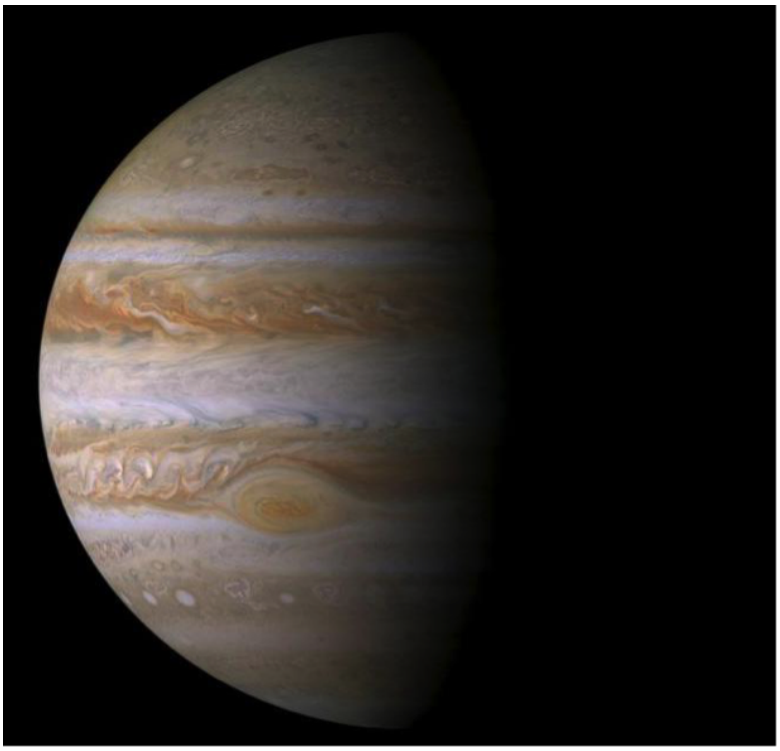

Figure 5.1: This true color image of Jupiter was taken by NASA's *Cassini* spacecraft on its journey to Saturn. Zonal recirculation is apparent in the distinct banding that has been seen by humans in Jupiter's atmosphere since the 17th century. These zonal flows are permeated by oval shaped vortices, which range from the Great Red Spot to smaller storms of various colors. The circulation of Jupiter's atmosphere operates under much cooler temperatures than those of its hot-Jupiter cousins. This means the wind speeds are generally slower in Jupiter than in hot-Jupiters, as the latter must redistribute vastly greater amounts of energy between their permanent day and night sides. From NASA/JPL/Space Science Institute.

5.1.1 Exoplanetary Winds

The necessity of dynamic winds in models of exoplanet atmospheres, especially those of gas giants, is conspicuous thanks to Jupiter, shown in remarkable *Cassini* image quality in Figure 5.1. Even small telescopes can observe its atmospheres zonal (east-west) bands, the Great Red Spot, and small active storms. There are two catagories of zonal bands –those that rotate in the same direction as the planet (belts) and those that rotate in the opposite direction (zones). Approximately 30

of these bands exist on Jupiters surface (Vasavada & Showman 2005). They are permeated by vortices of all sizes, rotational directions, ages, and colors that range from the long-lived and enormous Great Red Spot to comparatively small and short-lived spirals. There are also storms which mark sites of intensely localized convection (Vasavada & Showman 2005). For the purposes of exoplanetary winds, specifically those which can be measured with phase curves, we are primarily interested in large-scale zonal convective processes.

While the winds of Jupiter reach maximum speeds of about 150 ms^{-1}, winds of 2 kms^{-1} have been measured on HD209458 b with 95% statistical significance confidence level (Snellen et al. 2010). To do this, the authors measured a 2 kms^{-1} blueshift in carbon monoxide absorption features in the planets atmosphere. These tremendously fast winds shift the hot spot on the planets dayside eastward of the zone receiving the most direct solar radiation (substellar point) by $40.9° \pm 6.0°$ (Zellem et al. 2014). This group measured windspeed via phase curves from *Spitzer* at 4.5μm wavelengths. The phase curve maximum occurs 9.6 ± 1.4 hours before the secondary eclipse, which is indicative of equatorial superrotating winds induced by tidal-locking to HD209458. This agrees with circulation models of hot-Jupiters that are tidally locked to their host star, which have included superrotation since Showman & Guillot (2002) predicted it for 51-Pegasus b-like planets.

The original Showman & Guillot (2002) model uses angular momentum conservation requirements at different temperatures and pressures in different atmospheric layers to produce a numerical simulation of atmospheric circulation, which reaches a steady state after $\sim$400 Earth-days. Considering these simulations, the authors predict a cloud-free dayside, with clouds condensating on the night side of the planet due to material being exposed to equal pressures but lower temperatures. These clouds then sublimate when they hit the dayside. More recent

versions of this type of model, such as Rauscher & Menou (2013), include ohmic dissipation and the drag effect of exoplanets magnetic field. Ohmic dissipation, also known as Joule heating, describes the process of heat release through the passing of current through a conductor. In this case, the exoplanet is the conductor. It may be responsible for the inflated radii of hot-Jupiters (Batygin & Stevenson 2010), though this remains unresolved (Huang & Cumming 2012).

As shown in Figure 5.2, increasing the strength of the magnetic field in the Rauscher & Menou (2013) model significantly slows the wind speed. This in turn stops the warping of the hot zone by wind transportation, as shown in Figure 5.3. This warping shifts the center of the hot zone away from the substellar point. It is unlikely that the planetary hotspot would depart from the equator. For their HD209458 b model with no magnetic field, peak thermal emission was shifted from the substellar point by 12°, while magnetic field models have peak emission aligned with the substellar point to between zero and three degrees. For HD189733 b, the model gives the same effective longitude of peak thermal emission (17° offset from substellar point) for each magnetic field. In the future, wind speeds may be used to probe the magnetic fields of exoplanets, as hot-Jupiters without superrotating jets would likely have powerful magnetic fields. It is predicted that most will not, however, as tidal locking is thought to induce weak magnetic fields (Grießmeier et al. 2004). Studies of exoplanet winds can therefore contribute to research on exoplanetary magnetic fields and their evolution.

The flow fields of exoplanet atmospheres are not monodirectional by any means. They change drastically with depth, as illustrated in Figure 5.4. However, there is a dominant direction of overall wind magnitude, which is the direction of the equatorial superrotating jet.

Cowan & Agol (2011) model a close orbiting hot-Jupiters atmosphere and its

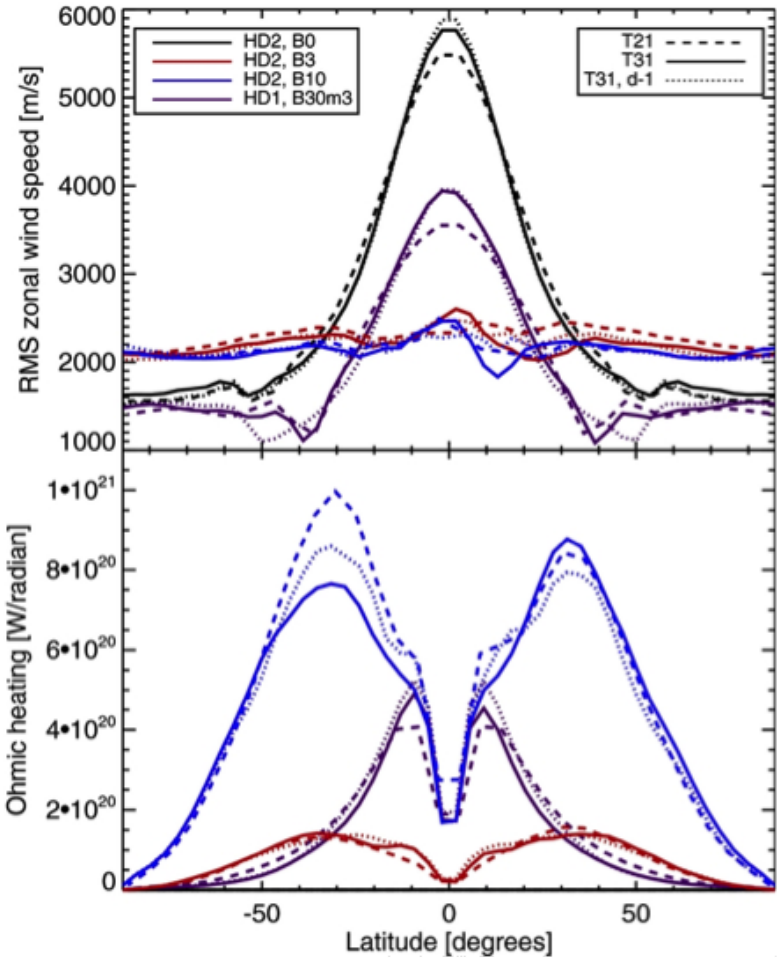

Figure 5.2: Illustrates the change in wind speed (top) and ohmic heating (bottom) with respect to magnetic field strength. The line colors are indicative of magnetic field strength. Black is the model for HD 209458 b with a magnetic field of strength $B = 0$, red is the model for HD 209458 b with strength $B = 3$, and blue is the model for HD 209458 b with $B = 10$. Purple corresponds to the model for HD 189733 b with magnetic field strength $B = 30$. Clearly an increased magnetic field serves to slow the wind on HD 209458 b, while the winds of HD 189733 b remain relatively strong. From Rauscher & Menou (2013).

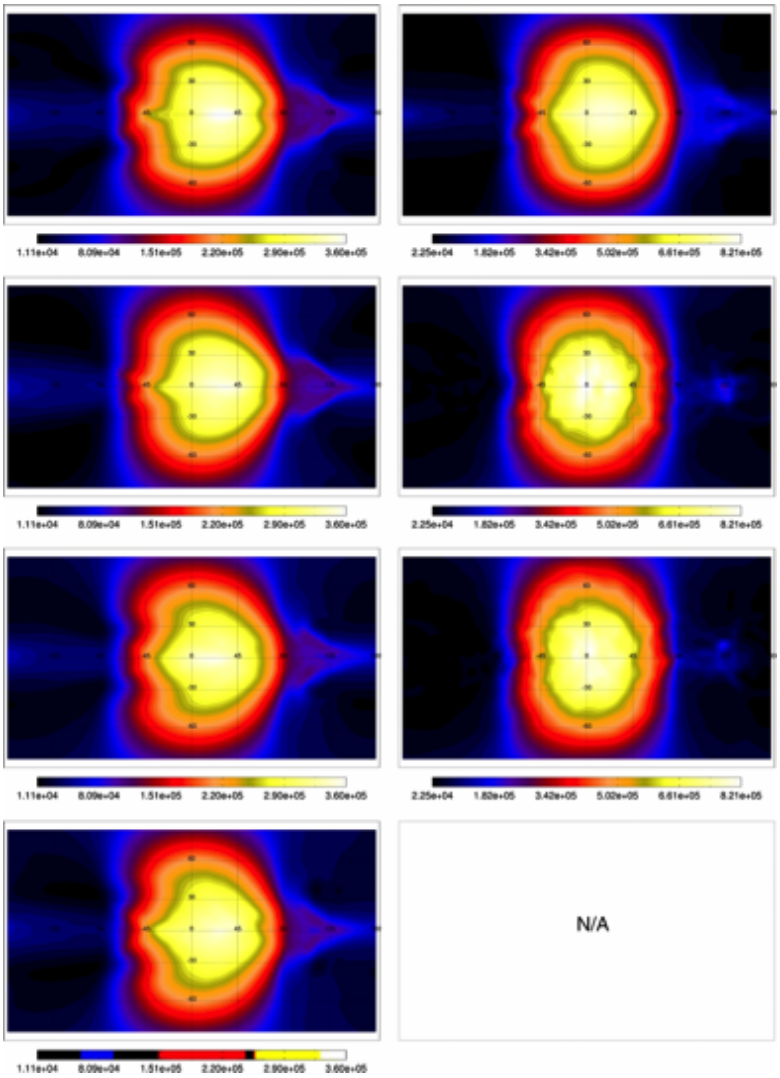

Figure 5.3: Shows the warping of the hot zone from the substellar point, which is at zero on these plots. The warping of the hot zones creates an offset between the substellar point and the zone of maximal thermal radiation, which may be detectable in phase effects if it is displaced far enough. The left column is the model for HD 187933 b and the right is HD 209458 b with rows corresponding to $B = 0$ G (top row), $B = 3$ G (second row), $B = 10$ G (third row), and $B = 30$ G (fourth row). Clearly increasing the strength of HD 209458 bs magnetic field significantly centers the hot zone on the substellar point, as it greatly drags circulating winds. On HD 189733 b, the offset persists in all modeled magnetic fields to a level detectable by phase curve analysis. From Rauscher & Menou (2013).

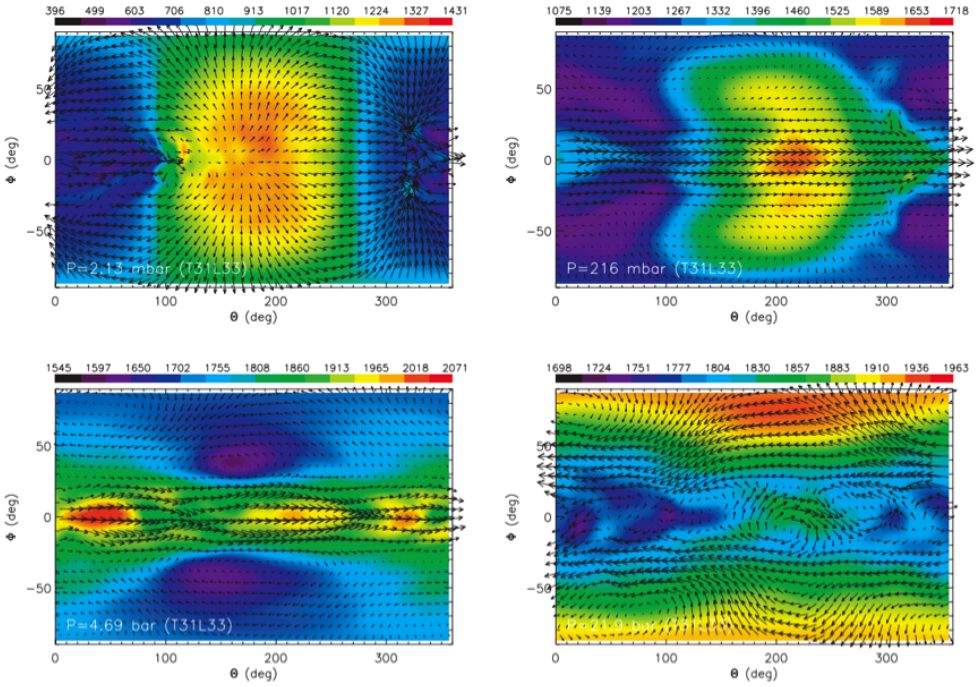

Figure 5.4: Recirculation flow maps at different layers of a model atmosphere of HD 209458 b. The P value corresponds to the pressure at that level of the atmosphere. $P = 2.13$ mbar (top left), $P = 216$ mbar (top right), $P = 4.69$ mbar (bottom left) and $P = 21.9$ mbar (bottom right). Clearly the upper-most layers of the atmosphere circulate more freely, radiating outwards from the hot zone. At deeper depths, such as 216 mbar, the equatorial superrotation can be seen, with lingering heat from the hot zone still readily apparent. At 4.69 bars, the superrotating jet is flowing at extremely fast speeds and carries a significant amount of heat with it. The higher latitude zones of the planet, especially those beneath the hotzone and above and below the jets, become distinctly colder than the rest of that atmospheric layer. In the deeper layers of the atmosphere, the dominant feature is a distinctly cold zone underneath the superrotating wind jet From Heng et al. (2011).

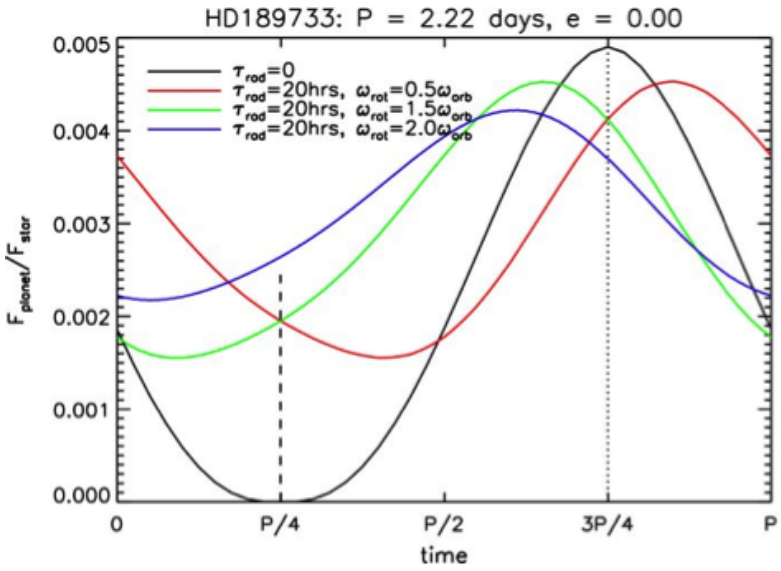

Figure 5.5: The dashed line marks the transit and the dotted line marks the secondary eclipse. Illustrates the modeled changing phase curve of HD 189733 b with respect to radiative timescale and wind speed, where the units of windspeed are the exoplanets rotational velocity. Clearly the fastest winds (blue) create the greatest spreading of thermal flux, which causes the drop in amplitude maximum, and the greatest offset in the hot zone from the substellar point. If the wind speed is less than that of the planets rotational velocity (red), the phase curve peak occurs after the secondary eclipse. From Cowan & Agol (2011).

resulting light curve. The offset of the phase effect maxima from the location of secondary eclipse is a function of the radiative timescale and the rotational velocity of the wind. These parameters are degenerate, which presents the greatest challenge for this type of study. Eccentricity and argument of periastron are other important parameters for characterizing the lightcurve, but these are nondegenerate. For eccentric orbits of sufficiently long period, such as those of HAT-P-2b, HD 17156b, and HD 80606b, a distinct ringing is produced in the lightcurve from the hotspot rotating in and out of view. The offset of thermal phase maxima, as well as the behavior induced by eccentric, long period orbits, is illustrated in Figure 5.5 and Figure 5.6 for the test cases for HD 189733 b and HAT-P-2 b.

This enhancement to the traditional phase curve model could have significant

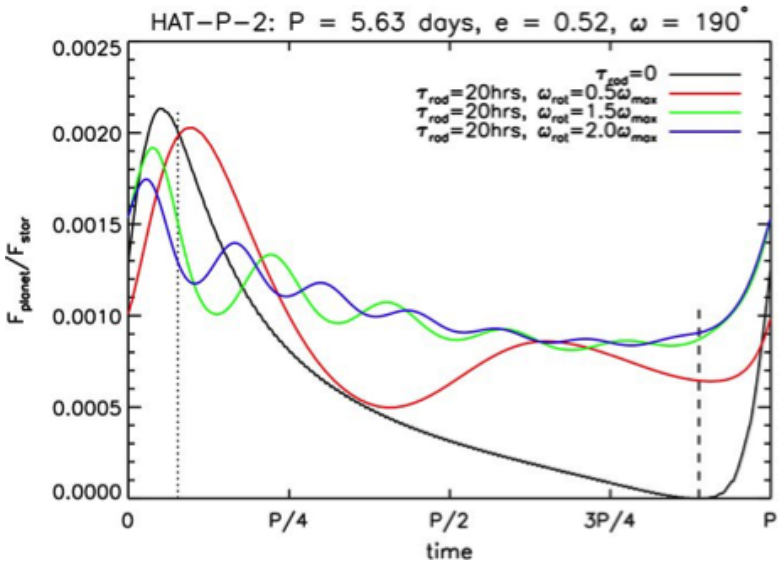

Figure 5.6: The dashed line marks the transit and the dotted line marks the secondary eclipse. Illustrates the change in modeled phase effects for HAT-P-2 b given different radiative timescales and wind speeds. The high eccentricity and relatively long period of this exoplanet can produce a ringing effect in the phase curve with the resonant wind velocity. The models with higher wind speeds clearly dissipate heat more efficiently, as they are of lower maximal amplitude, but do not drop in magnitude as quickly through the rest of the phase. From Cowan & Agol (2011).

use if applied to *Kepler* data. It would illuminate wind speeds for a plethora of hot-Jupiters, given an assumed radiative dissipation model. Furthermore, the prominent degeneracy between the thermal and reflective phase curves could be broken through addition of this offset, as the substellar zone will always be the area of maximal reflection, assuming the exoplanet has a uniform albedo. Not only are wind speeds critical for constraining models of exoplanet atmosphere dynamics, they also may provide a mechanism through which the strength of an exoplanet's magnetic field can be estimated. This would be a significant addition to exoplanet research, as methods for probing exoplanet interiors are relatively limited at present. The next step is to add the radiative timescale and rotational wind speed effects to a phase curve model that includes all four primary phase effects, such as the one presented in this thesis. Such a model could even further enrich the treasure of information regarding exoplanet characteristics found in *Kepler* lightcurves. Once a significant number of exoplanet wind speeds are measured, mechanisms underlying the magnitude and speed of recirculation can be understood and accessed, namely magnetic field strength. A modest sample of three exoplanet phase curves by Cowan et al. (2007) favors varying degrees of recirculation. The phase curve of ν Andromedae b (Harrington et al. 2006) is indicative of strong diurnal temperature variations, which is consistent with slower winds and a lesser degree of circulation. Determining the physical and evolutionary reasons behind these observations will grant astronomers deeper insight into the internal and external dynamics of hot-Jupiters.

5.1.2 K2

As of now, none of the confirmed candidates for *K2* exoplanets have shown signs of phase curves or occultations. Most are poor candidates for production of phase curves, as they are mostly sub-Jovian sized objects orbiting relatively small stars. However, in the future, *K2* will likely discover hot-Jupiters in its fields, which may show signs of occultations. Cold, large planets may still induce the gravitational phase effects in their host stars. Močnik et al. (2016) attempt to measure the secondary eclipse of WASP-157 b and find the signal is not strong enough to be picked up in *K2* data. Secondary occultation and phase curve analysis for *K2* targets will likely have to wait until more hot-Jupiter targets are discovered. After a few more campaigns, perhaps, our model can be applied to *K2* data.

5.1.3 Non-transiting Systems

Phase effects have been used to study nontransiting extrasolar planets such as υ Andromedae b (Harrington et al. 2006), HD 179949 b (Cowan et al. 2007), and HD 46375 b (Gaulme et al. 2010), the former two with *Spitzer* and the latter with *CoRoT*. The phase curve for υ Andromedae b is illustrated in Figure 5.7. They have not, however, been studied in *Kepler* data, as the long-term stability of the *Kepler* lightcurve requires a thorough detrending process that would likely rid the system of its nontransiting phase curves. Even without utilization of *Kepler* data for non-transiting system analysis, phase effects can still be used to successfully probe non-transiting planets observed with other space telescopes, as is proven by the aforementioned studies. Dedication of *Spitzer* time to observations of other tidally locked hot-Jupiter systems, both transiting and nontransiting, will give

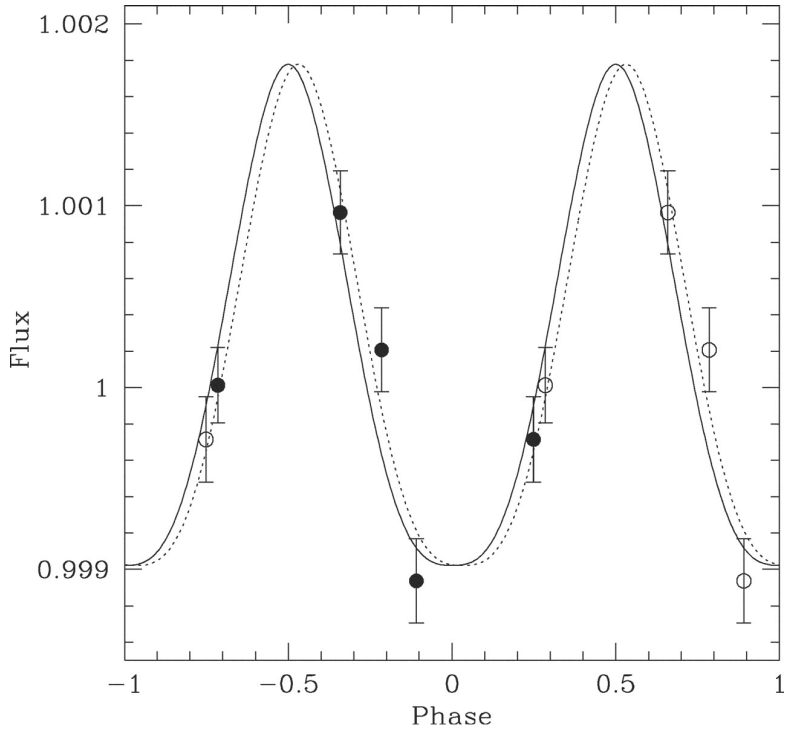

Figure 5.7: Phase curve for the nontransiting exoplanet υ Andromedae b measured using the 24μm channel of the Multiband Imaging Photometer for *Spitzer*. Thermal emission is thought to dominate the phase effects measureable from this 0.69 M_{Jup} minimum mass planet with an orbital period of 4.617 days (Harrington et al. 2006), as it is close enough to υ Andromedae to be extremely hot, but too small to induce gravitational phase effects on the F star. The filled points are the phase curve data after calibrations have been applied. The open points are the same data points shifted over by one phase. From Harrington et al. (2006).

more samples of exoplanet wind speeds. Eventually, this sample set will become robust enough to assess the physical and evolutionary mechanisms that produce the seemingly diverse recirculation rates of close orbiting exoplanets.

5.2 Summary and Final Acknowledgements

Exoplanet science has progressed significantly in the last two decades since the discovery of 51 Pegasi b by Mayor & Queloz (1995). We can now make assessments of exoplanet atmosphere characteristics through both single-band photometry and

spectroscopy. We have developed a transit, secondary eclipse, and phase curve model that fits to *Kepler* data. Its effectiveness in calculating many planetary parameters has been demonstrated on multiple *Kepler* exoplanets. Addition of more details to this model, specifically those related to exoplanetary wind measurement, would make it even more useful for characterizing exoplanets. It would provide a means to break the temperature and albedo parameter degeneracies by separating the thermal and reflective phase effects through the addition of wind. Phase curve models represent our most detailed understanding of lightcurve analysis, as they incorporate every possible contributing flux effect. This in turn makes them the most useful exoplanet models to be applied to single-band photometry. Our phase curve model will continue to be improved in order to further advance our knowledge of exoplanetary properties.

This research has made use of the NASA Exoplanet Archive, which is operated by the California Institute of Technology, under contract with the National Aeronautics and Space Administration under the Exoplanet Exploration Program. This paper includes data collected by the *Kepler* mission. Funding for the *Kepler* mission is provided by the NASA Science Mission directorate.

Bibliography

Akeson, R. L., et al. 2013, PASP, 125, 989

Batygin, K., & Stevenson, D. J. 2010, ApJ, 714, L238

Benneke, B., & Seager, S. 2012, ApJ, 753, 100

Biferno A., e. a. 2015, NASA's Eyes on Exoplanets, California Institute of Technology

Butler, R. P., et al. 2006, ApJ, 646, 505

Cowan, N. B., & Agol, E. 2011, ApJ, 726, 82

Cowan, N. B., Agol, E., & Charbonneau, D. 2007, MNRAS, 379, 641

Crossfield, I. 2012, Transit light curve routines, url-http://web.archive.org/web/20080207010024/http://www.808multimedia.com/winnt/kernel.htm accessed: 2015-10-03

Crossfield, I. J. M., et al. 2015, ApJ, 804, 10

Demory, B.-O., et al. 2011, ApJ Letters, 735, L12

Dieck, C. 2008, Master's thesis, Wesleyan University

Doppler, C. 1842, ber das farbige Licht der Doppelsterne und einiger anderer Gestirne des Himmels (Prag 1842 bei Borrosch und Andr)

Dunham, E. W., et al. 2010, ApJ Letters, 713, L136

Earl, D. J., & Deem, M. W. 2005, Physical Chemistry Chemical Physics (Incorporating Faraday Transactions), 7, 3910

Esteves, L. J., De Mooij, E. J. W., & Jayawardhana, R. 2015, ApJ, 804, 150

Esteves, L. J., Mooij, E. J. W. D., & Jayawardhana, R. 2013, ApJ, 772, 51

Flaherty, K. M., Hughes, A. M., Rosenfeld, K. A., Andrews, S. M., Chiang, E., Simon, J. B., Kerzner, S., & Wilner, D. J. 2015, ApJ, 813, 99

Foreman-Mackey, D., Hogg, D. W., Lang, D., & Goodman, J. 2013, PASP, 125, 306

Fressin, F., et al. 2013, ApJ, 766, 81

Galilei, G. 1610, Sidereus Nuncius (Unknown)

Gaulme, P., et al. 2010, AAP, 518, L153

Goodman, J., & Weare, J. 2010, Communications in applied mathematics and computational science, 5, 65

Gostev, N. Y. 2011, Astronomy Reports, 55, 649

Grießmeier, J.-M., et al. 2004, AAP, 425, 753

Haas, M. R., et al. 2010, ApJ Letters, 713, L115

Han, E., Wang, S. X., Wright, J. T., Feng, Y. K., Zhao, M., Fakhouri, O., Brown, J. I., & Hancock, C. 2014, PASP, 126, 827

Harrington, J., Hansen, B. M., Luszcz, S. H., Seager, S., Deming, D., Menou, K., Cho, J. Y.-K., & Richardson, L. J. 2006, Science, 314, 623

Hauschildt, P. H., Allard, F., & Baron, E. 1999, ApJ, 512, 377

Hellman, C. D. 1965, Science, 150, 1279

Heng, K., Menou, K., & Phillipps, P. J. 2011, MNRAS, 413, 2380

Hou, F., Goodman, J., Hogg, D. W., Weare, J., & Schwab, C. 2012, ApJ, 745, 198

Howell, S. B., et al. 2014, PASP, 126, 398

Huang, X., & Cumming, A. 2012, ApJ, 757, 47

Ivezić, Ž., Connolly, A., Vanderplas, J., & Gray, A. 2014, Statistics, Data Mining and Machine Learning in Astronomy (Princeton University Press)

Kane, S. R., & Gelino, D. M. 2011, ApJ, 729, 74

Kepler, J. 1609, Astronomia Nova (Unknown)

Kipping, D., & Bakos, G. 2011, ApJ, 730, 50

Knutson, H. A., Charbonneau, D., Noyes, R. W., Brown, T. M., & Gilliland, R. L. 2007, ApJ, 655, 564

Koch, D. G., et al. 2010, ApJ Letters, 713, L131

Lasunncty. 2007, Orbit1, Wikimedia Commons url-https://commons.wikimedia.org/wiki/File:Orbit1.svg

Latham, D. W., et al. 2010, ApJ Letters, 713, L140

Lecavelier Des Etangs, A., Pont, F., Vidal-Madjar, A., & Sing, D. 2008, AAP, 481, L83

Loeb, A., & Gaudi, B. S. 2003, ApJ Letters, 588, L117

López-Morales, M., & Seager, S. 2007, ApJ Letters, 667, L191

Lovis, C., & Fischer, D. 2010, Exoplanets, ed. S. Seager (University of Arizona Press)

Lund, M. N., et al. 2014, AAP, 570, A54

Mandel, K., & Agol, E. 2002, ApJ Letters, 580, L171

Mayor, M., & Queloz, D. 1995, Nature, 378, 355

Mislis, D., Heller, R., Schmitt, J. H. M. M., & Hodgkin, S. 2012, AAP, 538, A4

Montet, B. T., et al. 2015, ApJ, 809, 25

Morris, B. M., Mandell, A. M., & Deming, D. 2013, ApJ Letters, 764, L22

Močnik, T., et al. 2016, ArXiv e-prints

Müller, H. M., Huber, K. F., Czesla, S., Wolter, U., & Schmitt, J. H. M. M. 2013, AAP, 560, A112

Murray, C., & Correia, A. 2010, Exoplanets, ed. S. Seager (University of Arizona Press)

Murray, C. D., & Dermott, S. F. 1999, Solar system dynamics (Cambridge University Press)

Newton, I. 1687, Philosophiae naturalis principia mathematica (Londini : Jussu Societatis Regiae ac typis Iosephi Streater : Prostat apud plures bibliopolas)

Pál, A., et al. 2008, ApJ, 680, 1450

Parviainen, H. 2015, MNRAS, 450, 3233

Placek, B., & Knuth, K. H. 2015, in American Institute of Physics Conference Series, Vol. 1641, American Institute of Physics Conference Series, 447–455

Placek, B., Knuth, K. H., & Angerhausen, D. 2014, ApJ, 795, 112

Planck Collaboration et al. 2014, AAP, 571, A1

Rauscher, E., & Menou, K. 2013, ApJ, 764, 103

Schneider, J., Dedieu, C., Le Sidaner, P., Savalle, R., & Zolotukhin, I. 2011, AAP, 532, A79

Seager, S. 2010, Exoplanets (University of Arizona Press)

Seager, S., & Mallén-Ornelas, G. 2003, ApJ, 585, 1038

Serindag, D. 2015, Analyzing Kepler Exoplanets from their Optical Phase Curves

Serindag, D., & Redfield, S. 2015, in American Astronomical Society Meeting Abstracts, Vol. 225, American Astronomical Society Meeting Abstracts, 257.37

Showman, A. P., & Guillot, T. 2002, AAP, 385, 166

Shporer, A., & Hu, R. 2015, AJ, 150, 112

Snellen, I. A. G., de Kok, R. J., de Mooij, E. J. W., & Albrecht, S. 2010, Nature, 465, 1049

Szab, G. M., et al. 2011, ApJ Letters, 736, L4

Tully, R. B., Courtois, H., Hoffman, Y., & Pomarède, D. 2014, Nature, 513, 71

Van Cleve, D. A. C. . J. E. 2009, Kepler Instrument Handbook (KSCI-19033), NASA

Van Cleve, J., Caldwell, D., et al. 2009, KSCI-19033

Vanderburg, A., & Johnson, J. A. 2014, PASP, 126, 948

Vanderburg, A., et al. 2016, ApJ, 222, 14

Vasavada, A. R., & Showman, A. P. 2005, Reports on Progress in Physics, 68, 1935

Winn, J. 2010, Exoplanets, ed. S. Seager (University of Arizona Press)

Woolfson, M. 2000, Astronomy and Geophysics, 41, 1.12

Zellem, R. T., et al. 2014, ApJ, 790, 53